A STUDY ON DISPERSION IMPROVEMENT OF ACTIVE SITES ON SUPPORTED METAL CATALYSTS

by

Enes Emre Taş

B.S., Chemical Engineering, Boğaziçi University, 2019

B.S., Chemistry, Boğaziçi University, 2019

Submitted to the Institute for Graduate Studies in
Science and Engineering in partial fulfillment of
the requirements for the degree of
Master of Science

Graduate Program in Chemical Engineering

Boğaziçi University

2023

to my family

ACKNOWLEDGEMENTS

I am thankful to all of those who provided help and support throughout my research. I owe a special debt of gratitude to my thesis supervisor, Prof. Ahmet Erhan Aksoylu, who not only imparted crucial academic skills and perspectives but also offered his continuous encouragement and faith in my capabilities.

I would also like to express my thanks to Dr. Burcu Selen Çağlayan for her guidance and support throughout my studies.

I wish to express my profound gratitude to Prof. Ramazan Yıldırım, and Prof. Ayşe Nilgün Akın for graciously accepting the invitation to serve as esteemed members of my thesis committee. I am deeply indebted to them for sparing their valuable time to review and for providing invaluable feedback on my thesis.

I also wish to express my gratitude to Dr. Belkız Merve Eropak, Cihat Öztepe, and Ali Uzun for their guidance and invaluable assistance whenever needed.

I would like to extend my heartfelt appreciation to Burcu Acar, Necdet Semih Altınsoy, Gülten Çelebi, Barış Demirci, Serhat Erşahin, Ceren Hatipoğlu, Burcu Oral, Onur Ordulu, Hasret Nur Özata, Pınar Özdemir, Mert Özden, Dalga Merve Özkan, Özge Selçuk, Göksu Şengün, and Beyza Yılmaz for their continuous encouragement, friendship, and support throughout the ups and downs of my academic journey. I would also like to thank my former classmate, groupmate, and lab partner, as well as fellow teaching assistant, Hayrettin Hasan Köybaşı, for his longstanding support and friendship during my undergraduate and graduate studies.

Finally, I would like to acknowledge my deepest gratitude to my lovely family for their moral support, patience, and encouragement. Their endless love and trust have always kept me motivated. Their love, understanding, and belief in my abilities have been the driving force behind my accomplishments.

I would also like to acknowledge the financial support provided by the Presidency of the Republic of Turkey, Department of Strategy and Budget (Ministry of Development), through project 2016K12-2838.

ABSTRACT

A STUDY ON DISPERSION IMPROVEMENT OF ACTIVE SITES ON SUPPORTED METAL CATALYSTS

The current work aims to enhance metal dispersion on supported metal catalysts synthesized via dry impregnation (DI) method by focusing on 10 wt.% Ni/γ-Al_2O_3 catalysts as a specific example. Impregnated samples underwent calcination at varying temperatures (500°C, 700°C, and 900°C) and subsequent reduction at 800°C for 1 h under pure H_2 flow. Dispersion levels were determined by using the static H_2 chemisorption method. Additionally, N_2 physisorption, Raman, XRD and XPS analyses were performed on selected samples. The study includes the use of γ-Al_2O_3, precalcined Al_2O_3 at 920°C, and 1 wt.% La-doped Al_2O_3 as support materials, for which the PZC values were measured as 8.49, 8.42, and 7.82, respectively, using the salt addition method. pH shift models were utilized to determine the final pH values of impregnated slurry and to adjust the pH of the precursor solution. The behavior of nickel species in the impregnating solutions was modeled based on the changing pH, employing stability constants of potential compounds. Suitable complexing agents were selected according to the support material's surface charge across the pH scale to obtain Ni complexes/chelates. UV-Visible Spectrophotometry was used for the analysis of solutions. Results demonstrate that the surface distribution of metallic Ni is the primary factor determining dispersion levels at calcination temperature of 500°C. Conversely, at 700°C and 900°C, the formation of $NiAl_2O_4$ becomes the predominant factor, as confirmed by XPS and XRD analyses. NTA and CA complexes yield the highest dispersion results at lower calcination temperatures (500°C and 700°C), while the EDTA complex exhibits better results for sample calcined at 900°C. The highest dispersion level achieved using the Ni-CA complex for sample calcined at 500°C is 9.2624%, whereas the lowest dispersion is observed with the same support and solution when it is calcined at 900°C, with a dispersion of 2.5622%. These findings indicate that dispersion is influenced by a combination of different factors that should be evaluated holistically.

ÖZET

DESTEKLİ METAL KATALİZÖRLERDE AKTİF SİTELERİN DİSPERSİYONUNUN ARTIRILMASI ÜZERİNE BİR ÇALIŞMA

Mevcut çalışma, kütlece %10 Ni/γ-Al_2O_3 katalizörünü örnek olarak kullanarak, kuru emdirme (DI) yöntemi ile sentezlenen destekli metal katalizörlerde metal dispersiyonunu artırmayı amaçlamaktadır. Emprenye edilmiş örnekler, farklı sıcaklıklarda (500°C, 700°C ve 900°C) kalsinasyona tabi tutulmuş ve ardından 800°C'de saf H_2 akışı altında 1 saat boyunca indirgenmiştir. Dispersiyon seviyeleri, statik H_2 kemisorpsiyonu yöntemi kullanılarak belirlenmiştir. Ayrıca, seçilen örnekler üzerinde N_2 fizisorpsiyonu, Raman XRD ve XPS analizleri yapılmıştır. Çalışmada γ-Al_2O_3, 920°C'de kalsine edilmiş Al_2O_3 ve kütlece %1 La eklenmiş Al_2O_3'in destek malzemesi olarak kullanılmış ve destek malzemelerinin Sıfır Yük Noktaları (PZC) tuz ekme yöntemi kullanılarak sırasıyla 8.49, 8.42 ve 7.82 olarak ölçülmüştür. pH değişimine ait modeller, emprenye edilmiş destek-çözelti karışımında final pH değerlerini belirleyerek öncül çözeltinin pH değerini ayarlamak için kullanılmıştır. Emprenye çözeltisindeki nikel türlerinin davranışı, olası bileşiklerin kararlılık sabitlerini kullanarak değişen pH'ye bağlı olarak modellenmiştir. Destek malzemesinin pH ölçeği boyunca değişen yüzey yüküne bağlı olarak uygun kompleksleyici ajanlar seçilip Ni kompleksleri/şelatları elde edilmiştir. Çözelti analizi için UV-Vis spektrofotometrisi kullanılmıştır. Sonuçlar, 500°C kalsinasyon sıcaklığında metalik Ni yüzey dağılımının dispersiyon seviyelerini belirleyen temel faktör olduğunu göstermektedir. Bununla birlikte, XPS ve XRD analizlerine göre 700°C ve 900°C'de $NiAl_2O_4$ oluşumunun baskın faktör olduğu görülmüştür. NTA ve CA kompleksleri, daha düşük kalsinasyon sıcaklıklarında (500°C ve 700°C) en yüksek dispersiyon sonuçlarını verirken, EDTA kompleksi 900°C kalsinasyonda daha iyi sonuçlar göstermektedir. 500°C' kalsinasyonla elde edilen en yüksek dispersiyon seviyesi, Ni-CA kompleksi kullanıldığında % 9.2624 iken, aynı destek ve çözeltinin 900°C'de kalsinasyonuyla en düşük dispersiyon % 2.5622 olarak gözlemlenmiştir. Bu bulgular, dispersiyonun farklı faktörlerin kombinasyonu tarafından etkilendiğini ve bu faktörlerin bütünsel olarak değerlendirilmesi gerektiğini göstermektedir.

TABLE OF CONTENTS

LIST OF FIGURES

LIST OF TABLES

LIST OF SYMBOLS

A	Surface area
A_m	Cross-sectional area of one molecule
C	Concentration
c	BET constant
D	Dispersion
E_1	Heat of adsorption of N_2 in the formation of monolayer
E_L	Heat of liquefaction of N_2
e	Elementary charge
F	Faradaic constant
I	Ionic strength
K	Equilibrium constant
k	Boltzmann constant
L	Metal particle size
N_0	Avogadro number
N_s	Surface site hydroxyl density
P	Equilibrium pressure of adsorbates
P_0	Saturation pressure of adsorbates
R	Universal gas constant
r	Radius
S_g	Total surface area per unit weight of catalyst
S_M	Metal surface area
T	Temperature
V	Volume
v	Adsorbed gas quantity
v_m	Monolayer adsorbed gas quantity
w_{cat}	Catalyst weight
wt	Weight
Z	Charge of adsorbed species

α	Alpha phase
β	Cumulative formation constant
γ	Gamma phase
Γ	Surface adsorption density
ΔG	Gibbs free energy
ΔH	Enthalpy of reaction
ΔV	Volume of liquid N_2 removed
δ	Delta phase
ε_0	Vacuum permittivity
θ	Theta phase
κ	Debye-Hückel reciprocal double layer length
σ	Surface charge distribution
ψ	Surface potential

LIST OF ACRONYMS/ABBREVIATIONS

ALD	Atomic Layer Deposition
acac	Acetylacetonate
BET	Brunauer – Emmett - Teller
BJH	Barrett – Joyner - Halenda
CA	Citric Acid
CEDI	Charge Enhanced Dry Impregnation
CZLP	Cerium – Zirconia – Lanthanum - Praseodymium
DI	Dry Impregnation
DRM	Dry Reforming of Methane
EDTA	Ethylenediaminetetraacetic acid
en	Ethylenediamine
FWHM	Full Width of Half Maximum
HRTEM	High-Resolution Transmission Electron Microscopy
IWI	Incipient to Wetness Impregnation
NTA	Nitrilotriacetic acid
PSD	Pore Size Distribution
PZC	Point of Zero Charge
RPA	Revised Physical Adsorption
SBA	Santa Barbara Amorphous
TOF	Turn Over Frequency
TSA	Total Surface Area
TPR	Temperature Programmed Reduction
TPV	Total Pore Volume
UV-Vis	Ultraviolet – Visible
XPS	X-ray Photoelectron Spectroscopy
XRD	X-Ray Diffraction

1. INTRODUCTION

Chemical reactions lie at the heart of countless events taking place throughout the universe, have been explored through numerous scientific researches, and these ongoing studies has allowed us to build an understanding of their nature over time. This knowledge has generated a broad range of chemical products that are vital for meeting the demands of ever-growing human population in modern society. Controlling while speeding up such chemical reactions is expedient and needed for economically efficient production of chemicals as well as fuel and energy, thus necessitating the management of energy flow as well as product generation (including side and by-products). Catalysts are pivotal in many chemical reactions due to aforementioned reasons; it is vital to attain mechanistic of such reactions over them and how those reactions be regulated via modifying the design of the catalysts, which needs combined use of theoretical chemistry, inorganic chemistry, experimental design and establishment of structure-activity relation through exploiting all in a combined fashion.

Catalysts are substances used to decrease the activation energy by changing the mechanism of a reaction and thereby increasing the reaction rate while keeping themselves essentially unchanged. Catalytic systems can be classified as homogeneous and heterogeneous according to the phases present in the reaction medium. In homogeneous catalysis, the phases of the catalyst and reactants are the same, unlike heterogeneous systems. Moreover, in heterogeneous systems, the reactants are mostly in liquid or gaseous phase, while the catalyst is in the solid phase. (Fogler, 2016).

In heterogeneous catalysis, reaction takes place at the solid (catalyst) and fluid (gas or liquid reactants) interface, therefore, large surface area is required for effective catalysis. However, reaction only takes places on surface atoms or cluster(s) of atoms, called active sites, as the active part of the catalysts and are, almost all the time, metals and they have close packed structures. Active sites are dispersed over a solid with high surface area, mostly metal oxides or carbon, called as support, to increase the exposed surface area of the active sites to reactants. Various methods, such as impregnation and deposition precipitation, can be employed to disperse metal particles on support materials. Metal oxides such as Titania

(TiO_2), alumina (Al_2O_3) and zirconia (ZrO_2) are the most common examples of support materials (Ma and Zaera, 2006).

Supported metal catalyst design is a complex process that requires well-defined methodologies, well-understood properties and controlled preparation steps, all of which need to have expertise on different scientific research areas, like inorganic chemistry, thermodynamics, fluid dynamics/microfluidics, surface chemistry and cluster chemistry. Typically, the preparation of an industrial catalyst involves several stages. In general, at first, a support having suitable characteristics is prepared. Then, the metal precursor is distributed onto the support's surface. Subsequently, the catalyst undergoes drying and calcination to remove any moisture and facilitate the desired chemical changes. Finally, the precursor is transformed into the active and stable metallic phase through a reduction process (Foger, 1984).

Dispersion level of active sites on catalysts affects both their activity and durability. In processes that require high temperatures, catalysts may experience rapid activity loss due to various deactivation mechanisms such as coke formation, poisoning, sintering of active metal, or encapsulation of active metal particles. For instance, coke formation highly depends on the dispersion level and crystal size of metal in Ni-based DRM catalysts. Higher nickel dispersion, which corresponds to smaller Ni crystallites, reduces the rate of coke formation and increases the durability of the catalyst (Han et al., 2014).

In order to optimize catalyst efficiency, it is necessary to control parameters like metal loading, metal dispersion level and location of the metal clusters formed during the catalyst synthesis (Ortega-Domínguez et al., 2017). In various industrial applications, preparation of well dispersed metal catalysts is essential, particularly when the reaction and feasibility concerns impose of the use of high loading, to attain optimal catalytic activity. Impregnation and ion exchange methods are the most common methods for the preparation of catalysts. In impregnation method, high metal loading can be achieved but with limited metal dispersion levels (Nares et al., 2002). The main cause of low dispersion level can be the weak interactions of metal precursor with support established in impregnation step or redistribution of the active metal on support during the drying process, which heavily depends on the interaction between precursor and support surface (Foger, 1984). Interactions

between the support surface and the metal precursor can be controlled through understanding and regulating the properties of support (e.g., type / distribution of functional groups, acidity of surface etc.) and impregnation solution (e.g. factors such as the pH of the mixture, the type and concentration of the precursor compound, and the presence of competing ions can influence the process) (Brunelle, 1978).

During catalyst preparation, surface oxygen functional groups present on inorganic oxide supports serve as binding sites for metal precursor compounds, achieved through the displacement of ligands between functional groups and the metal precursor. The impregnation solution can exhibit a surface polarization effect, leading to a net electrical surface charge on suspended oxide particles, which is influenced by the dissociation of hydroxyl groups and reabsorption of hydroxo complexes in solution (Parks and DeBruyn, 1962). The charge on the support surface varies with the pH of the impregnation solution, where low pH values result in a positive charge and high pH values lead to a negative charge. Hence, the pH of the impregnation solution plays a crucial role in determining the interaction between the support and the added precursor compound. At an intermediate pH, the surface reaches a point where the net ion charge is zero, referred to as the point of zero charge (PZC) (Park and Regalbuto, 1995). PZC of a support can be used as a reference to choose the appropriate metal precursor for impregnation and deposition procedures (Eskandari et al., 2019).

In impregnation method, solubility of metal salt can cause a limitation for high loading and dispersion on support material. To increase loading, solubility of metal precursor must be high enough. Additionally, it is important to prevent formation of isolated metal ions and aggregation of metal clusters especially during impregnation and drying parts. In drying part, low viscosity of the impregnation solution can also cause a loss of active sites because of the redistribution of precursor molecules. Therefore, selected precursor solution must have sufficiently high viscosity to prevent low dispersion of active metal sites (Jos van Dillen et al., 2003).

Owing to its advantages such as technical simplicity, low cost and reproducible metal loadings, incipient wetness (i.e., dry) impregnation (IWI/DI) has an important place in traditional preparation methods of industrial heterogeneous catalysts (Foger, 1984). It is

therefore essential to improve this method to overcome low dispersion of active sites and thereby increase the activity and stability of catalyst in order to meet the necessary criteria for use in industrial applications (Foger, 1984).

In the current work, 10 wt.% Ni impregnated on γ-Al_2O_3 catalyst system was taken as a reference catalyst, and analyzed to optimize the catalyst preparation methodology through modification of experimental parameters in a combined fashion for the enhancement of metal dispersion. Main preparation parameters were composition of precursor solution, pH of precursor solution, support type (pre-treatments) and calcination temperature. Dry impregnation (DI) method was constantly used as preparation method for all samples. Support material was chosen as commercial γ-Al_2O_3, pre-doped Al_2O_3 calcined at 920°C, and La-doped (1 wt.%) Al_2O_3. Characterization of support surface by using N_2 physisorption and PZC measurement via salt addition method was conducted. pH shifts in precursor solutions after impregnation and physical adsorption of Ni on support surface models were obtained by using the results of support characterization. According to obtained model, most suitable Ni complex compounds were selected by considering their charge and support surface charge. Solutions of Ni complexes were modeled according to pH to select the most appropriate solution pH. To investigate the effect of calcination temperature, impregnated samples were calcined at different calcination temperatures as 500°C, 700°C and 900°C. Dispersion level of samples were measured by using static H_2 chemisorption method. According to dispersion results, selected samples were analyzed further by using N_2 physisorption, XRD, Raman Spectroscopy and XPS.

In this thesis, Chapter 2 consists of an extensive literature survey that covers the theoretical background and provides information about catalyst preparation methods and modifications aimed for enhancing metal-support interactions, including pH adjustments, additive utilization, and thermal treatments. Chapter 3 presents the experimental systems and procedures employed for catalyst preparation, as well as the characterization methods used in the current study. Chapter 4 encompasses the results obtained from experiments and their corresponding discussions, including discussions related to relevant models. Conclusions drawn from this research and recommendations for future studies are summarized in Chapter 5. Additionally, Appendix includes calculations, computer codes, and deconvolution results of X-Ray diffraction (XRD) and XPS peaks.

2. LITERATURE SURVEY

Transition metals play a crucial role as catalysts in various industrial chemical processes, including petroleum refining and alternative fuel production. However, the use of bulk metals as catalysts is often inefficient due to their high cost and limitations in thermal stability, which can lead to surface area losses caused by sintering. To overcome these challenges, transition metals are commonly dispersed on support materials with high surface areas, such as inorganic oxides or activated carbon, providing enhanced catalytic performance (Liu and Corma, 2018).

An effective catalyst requires well-designed and optimized active sites that are tailored for the specific reaction of interest. The catalytic activity and selectivity of a catalyst are primarily influenced by the interaction among the reactants, active sites, and support materials. In structure-insensitive reactions, the catalytic activity is directly related to the number of exposed active metal atoms, referred to as metal dispersion or metal surface area. However, in structure-sensitive reactions, the relationship between activity and metal dispersion can be more intricate, as the activity may also depend on the active site-support periphery and the properties of the support material itself. For both structure-sensitive and insensitive reactions, the long-term stability of a catalyst is closely linked to the type and dispersion of the active sites formed, as well as the extent of their exposure to the reactants during the reaction. Therefore, establishing a strong and stable active site-support interaction capable of withstanding the reactive environment is essential for achieving durable catalyst dispersion and maintaining efficient catalytic performance (Foger, 1984).

Catalytic activity is a crucial factor in chemical reactions, and the dispersion and arrangement of catalytically active components have a notable impact on determining the overall activity. Haneda et al. conducted a study that primarily focused on preparing Pt/Al_2O_3 catalysts with varying levels of Pt dispersion to investigate the performance of these catalysts in oxidation reactions of CO and C_3H_6. Results showed that increasing Pt dispersion led to higher CO conversion to CO_2, indicating a structure-insensitive reaction. The surface electronic state of Pt particles remained consistent regardless of Pt dispersion. However, in the case of C_3H_6 oxidation, the turnover frequency (TOF) was strongly influenced by Pt

dispersion. Initially, the TOF increased as Pt dispersion increased up to 0.20 and then plateaued, suggesting a structure-sensitive reaction. During the C_3H_6 oxidation, the formation of acrylate derivatives was observed, and its rate increased with reaction temperature. The researchers proposed that the formation of acrylate derivatives acted as the slow step in reactions with higher Pt dispersion, while the reaction of acrylate derivatives was the slow step in reactions with lower Pt dispersion. The lower TOF values observed on Pt/Al_2O_3 catalysts with lower Pt dispersion were attributed to the inhibition of catalytically active sites caused by the accumulation of acrylates. (Haneda et al., 2013)

2.1. Effect of Catalyst Preparation Method on Dispersion

Dispersed metal catalysts, where metal species are finely dispersed on a support material, have garnered significant attention due to their enhanced catalytic performance and improved stability compared to bulk metal catalysts. Various preparation methods have been developed to achieve efficient metal dispersion and control the properties of active sites (Foger, 1984).

The selection of an appropriate distribution method plays a critical role in controlling the metal loading and dispersion level in catalyst preparation. A wide range of distribution methods have been reported in the literature, including impregnation (wet/ dry, soaking etc.), ion exchange, deposition-precipitation, coprecipitation, reaction of organometallic clusters with functional groups on the support surface, and deposition of precursor compounds through vapor phase (Liu and Corma, 2018).

Impregnation is a widely used technique for catalyst preparation. It involves the wetting of a support material with a metal precursor solution, followed by drying and calcination to obtain the final catalyst sample. Dry impregnation (DI), also known as incipient wetness impregnation (IWI), is a commonly used method for catalyst preparation. In this method, a solid support material is mixed with a concentrated solution or vapor of the desired metal precursor. The support material absorbs the precursor solution or vapor until it reaches its maximum capacity, known as the incipient wetness point. The impregnated support is then dried to remove the solvent, leaving behind the deposited metal precursor. Subsequent calcination and reduction steps are often performed to convert the precursor into

the desired active metal form (Munnik et al., 2015). DI method allows precise control over metal loading, as the amount of precursor solution or vapor can be adjusted to match the support's pore volume. It is a straightforward and cost-effective method, particularly suitable for high metal loadings. It allows high metal loading on the support, but achieving uniform dispersion can be challenging. Factors such as metal precursor properties, impregnation solution pH, and support surface characteristics influence the metal dispersion during impregnation (Mehrabadi et al., 2017).

Wet impregnation is another widely used method for catalyst preparation. In this method, the support material is immersed or soaked in a solution containing the desired metal precursor. The support absorbs the precursor solution, impregnating the metal precursor into its pores. Excess solution is typically removed by filtration or centrifugation, and the impregnated support is then dried to eliminate the solvent. Calcination and reduction steps may follow to transform the precursor into the active metal form. Wet impregnation allows for efficient metal dispersion and is often employed for catalysts requiring low to moderate metal loadings. However, achieving uniform metal dispersion can be challenging, as the metal distribution can be influenced by factors such as the support material's surface properties, the metal precursor's affinity for the support, and the drying process (Huang and Schwarz, 1987).

The soaking method involves immersing the support material in a solution containing the metal precursor for an extended period. Unlike wet impregnation, where excess solution is removed, in the soaking method, the support remains in contact with the solution for a longer duration, allowing for deeper impregnation. This method enables enhanced metal uptake and better penetration into the support's pore structure, promoting improved metal dispersion. After soaking, the support is typically dried, followed by calcination and reduction steps to activate the catalyst. The soaking method is particularly useful for achieving higher metal loadings and uniform metal distribution. However, the extended soaking time required may result in longer preparation times compared to other impregnation methods (Choi and Suh, 2007).

Another approach involves the reaction of organometallic clusters with functional groups present on the support surface. This method allows the attachment of metal clusters

onto the support, promoting controlled metal dispersion. Additionally, vapor phase deposition methods have gained attention for their ability to achieve precise control over metal loading and dispersion. These methods involve the thermal decomposition of metal precursor vapors onto the support, resulting in the formation of highly dispersed metal species (Foger, 1984).

Deposition-precipitation is another commonly employed method for dispersed metal catalyst preparation. It involves the deposition of metal precursors onto a support surface, followed by precipitation and subsequent reduction to form metal nanoparticles. This method offers better control over metal dispersion and allows the preparation of highly active catalysts. The choice of deposition-precipitation conditions, such as the pH of the solution and the nature of the precipitating agent, plays a crucial role in achieving uniform metal dispersion (Foger, 1984).

Incorporation methods, such as ion exchange and solid-state intercalation, have also been used for dispersed metal catalyst preparation. These methods involve the exchange of metal ions or the intercalation of metal species into the support structure, leading to controlled metal dispersion. Ion exchange allows precise control over metal loading and dispersion by manipulating the ion exchange conditions, while solid-state intercalation enables the insertion of metal species into the interlayer spaces of layered support materials (Foger, 1984).

Other advanced techniques, such as sol-gel synthesis and atomic layer deposition (ALD), have gained prominence for dispersed metal catalyst preparation. Sol-gel synthesis involves the hydrolysis and condensation of metal alkoxides to form metal oxide nanoparticles that are then supported on the desired substrate. ALD, on the other hand, enables precise control over metal deposition by sequentially exposing the support material to metal precursors and reactants. These techniques offer excellent control over metal dispersion and provide opportunities for tailoring the catalyst structure at the atomic level (Lu et al., 2013).

Numerous studies have demonstrated that the preparation techniques employed for supported metal catalysts significantly affect the dispersion of active metal sites on the

support material. When selecting a preparation method, it is important to consider the desired catalyst properties and the specific catalytic reaction of interest. Morales (Morales, 2017) conducted research investigating the impact of different preparation methods on the catalytic activity of Ni/γ-Al_2O_3 catalysts using glycerol conversion as a probe reaction. Two methods, incipient wetness impregnation and wet impregnation, were employed to study their effects on the catalysts' structure and performance. The results showed that the choice of preparation method influenced both the selectivity and activity of the catalysts. Catalysts prepared through incipient wetness impregnation exhibited hydrogenolysis and dehydration routes, yielding diverse products. In contrast, catalysts prepared via wet impregnation method exhibited almost exclusive methane selectivity. The samples also displayed variations in particle size, dispersion, and carbon deposition. The author concluded that the choice of preparation method had a significant impact on the performance and properties of the catalysts.

2.2. Modifications on Preparation Methodology

2.2.1. Precursor Solution

Selection of an appropriate distribution method and precursor compound, such as a metal salt or a cluster compound, plays a crucial role in controlling the metal loading and dispersion level in catalyst preparation. Dry impregnation is a widely preferred method in many studies due to its simplicity, cost-effectiveness, and versatility. In this method, the support material is saturated with a solution volume equal to the total pore volume and then left to dry. However, to achieve a catalyst with a high level of dispersion in a controlled manner, it is essential to enhance the metal-support interaction to prevent agglomeration of residual metals during the drying process. Charge-enhanced dry impregnation (CEDI) is a modified version of the DI method that increases electrostatic metal-support interactions. This technique controls the surface charge of the support material by adjusting the solution pH, thereby enabling enhanced interactions between the metal precursor and the support at an optimal pH, effectively preventing metal agglomeration (Eskandari et al., 2019).

Eskandari et al. (Eskandari et al., 2019) conducted a study to investigate the impact of the charge-enhanced dry impregnation (CEDI) method on the particle size of monometallic

and bimetallic catalysts supported on one-dimensional SBA-15. Different metal precursors, including Pt, Pd, Co, Ni, and Cu, were used to disperse metals on SBA-15 at various loadings ranging from 1 to 20 wt.%. CEDI method was employed to prepare nanocrystalline catalysts, utilizing metal ammine complexes as precursors. It was observed that when using metal ammine chloride salt precursors, an additional washing step to remove chloride ions was not recommended to maintain high dispersion levels. The pH value at the point of zero charge (PZC) for SBA-15 was determined to be 2.7. Experimental results revealed that increasing the pH allowed for the deprotonation of OH groups on the support surface, facilitating the adsorption of cationic Pt/Pd ammine complexes. The final pH was adjusted to approximately 11. A comparison between charge-enhanced dry impregnation and dry impregnation (DI) without pH adjustment showed that the CEDI method resulted in smaller metal particle sizes. For a Pt loading of 8-9 wt.%, the particle size ranged from 8 nm to 11 nm with the DI method, while the CEDI method yielded a range of 5.7 nm to 8.3 nm. Similar results were observed for other metals and bimetallic catalysts, indicating that the CEDI method achieved better dispersion on SBA-15.

During the preparation of a catalyst using CEDI method, it is crucial to consider all possible complex formations in the solution. Cheng et al. conducted a study to investigate the benefits of pH adjustment during impregnation part for preparing a Pt catalyst supported on a ceria-based CZLP (Ce-Zr-La-Pr) support. PZC value for the CZLP support was determined to be approximately 6.5 using the salt addition method (Park and Regalbuto, 1995). By comparing the metal particle sizes of the catalysts prepared at different pH values to the pH value at PZC, the optimum pH value for precursor adsorption was found to be 3. Although repulsion was expected due to the positively charged Pt complexes in the $Pt(NO_3)_2$ precursor solution at pH values below PZC, the presence of labile terminal ligands in the Pt complex allowed for ligand exchange with surface hydroxyl groups. This led to a strong interaction between the precursor and the support surface at pH values below PZC (Dou et al., 2001). Based on the obtained characterization results, pH adjustment during the preparation process resulted in excellent thermostability and smaller Pt nanoparticle size in the catalyst (Cheng et al., 2018).

Kim et al. (Kim et al., 2009) investigated the impact of pH adjustment in the impregnating solution on dispersion improvement. Pt metal was impregnated onto silica,

silica-alumina, and alumina supports using various cationic ($[Pt(NH_3)_4]Cl_2$, $[Pt(NH_3)_4](NO_3)_2$) and anionic (H_2PtCl_6, $H_2Pt(OH)_6$) precursors. Suspension of support and precursor was adjusted to pH 1.5 or 10.5 to obtain positive or negative surface charges, respectively. Reported results demonstrated that pH adjustment enhanced the dispersion of Pt on all three support types, with particle sizes ranging from 4 to 15 nm. The effect of pH adjustment was particularly pronounced on the silica support. To further enhance Pt dispersion, titania was incorporated into all support types, resulting in new particle sizes between 1 and 2 nm. It was concluded that the pH adjustment improves interaction between support and Pt precursor and leads to high dispersion of Pt particles, but additional treatments such as titania incorporation to the support may be required to reach sufficiently small particle size for high catalytic activity.

Zhu et al. (Zhu et al., 2013) have developed a model known as the Revised Physical Adsorption (RPA) Model to elucidate the electrostatic interactions on the support surface using the concept of PZC. This model offers a versatile framework applicable to diverse metal-support systems. The core of the model lies in the protonation-deprotonation equilibrium of hydroxyl groups on the support surface, enabling the determination of the surface potential at varying pH levels as shown in Figure 2.1. Subsequently, by integrating this surface potential with the Langmuir adsorption model, the relative metal adsorption can be computed across different pH conditions. Notably, the model confines its considerations to the electrostatic forces exclusively between the surface and the adsorbing particles, and it embraces a simplified depiction achieved through the utilization of the Gouy-Chapman electrical double layer theory which has been widely employed in various research areas. It has been utilized to establish relationships between surface charge densities and surface potentials, estimate the thickness of the double layer, and investigate the influence of the double layer on electron-transfer kinetics.

Ewbank et al. (Ewbank et al., 2015) conducted a study to investigate the impact of different catalyst preparation methods on the composition of nickel species in alumina-supported nickel (Ni/Al_2O_3) catalysts. Two distinct catalyst preparation methods were employed in the study. The controlled adsorption method involved the preparation of 2 wt. % Ni/Al_2O_3 catalyst samples using strong electrostatic adsorption (SEA) method in conjunction with RPA calculations to determine the optimum pH value for maximum Ni

adsorption, which was found to be 9.5. The pH of the solution was maintained at 9.5 through regular hourly checks and readjustments using NH_4OH solution. The other method used was the dry impregnation method, without any pH adjustment. Different calcination and reduction temperatures were examined to investigate the behavior of Ni species on the support surface. Catalyst samples synthesized using controlled adsorption (2NiCA) exhibited lower formation of $NiAl_2O_4$ spinel but showed higher dispersion at various calcination temperatures due to strong interactions between the metal and support. On the other hand, the dry impregnation method (2NiDI) resulted in lower dispersion, with surface $NiAl_2O_4$ identified as the primary nickel species based on various characterization techniques, including H2 chemisorption, TPR, and TEM. The research concluded that the specific types of active sites present in the catalysts had a significant impact on their selectivity, activity, as well as the quantity and nature of carbonaceous deposits. These findings highlight the importance of tailored catalyst preparation and characterization for controlling catalytic performance. This research holds broader implications as it offers valuable insights into tailoring active nickel sites on γ-Al_2O_3 surfaces through systematic catalyst preparation and characterization. These findings enable the application of such catalysts in a wide range of reactions.

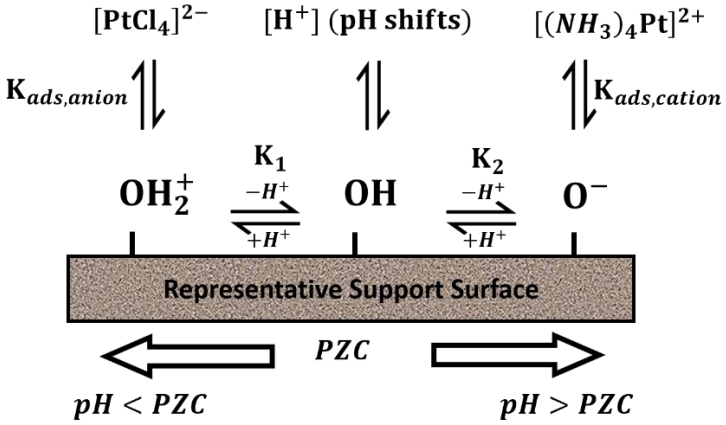

Figure 2.1. Schematic representation of electrostatic adsorption mechanism.

Choice of metal precursor is a crucial factor affecting the dispersion level. Utilizing stable metal complexes as precursor compounds, which in turn promote stronger metal-support surface interactions, can significantly enhance the distribution of active sites. Chelates have been widely employed as precursor compounds in the synthesis of supported metal catalysts, demonstrating promising properties in terms of both activity and stability.

Chelating agents, acting as electron donor ligands with two or more electron pairs, facilitate the attachment of metal ions. The formation of a metal chelate complex involves a Lewis acid-base reaction. Due to the exothermic nature of the reaction and the increased entropy resulting from the replacement of numerous solvent molecules with a single chelating ligand molecule, most chelates exhibit relatively high stability (Jos van Dillen et al., 2003). Chelate molecules possess a five- or six-membered cyclic molecular structure, which induces a steric hindrance effect, causing the separation of metal atoms from one another (Zhang et al., 2017). Furthermore, the gradual removal of water from chelate solutions leads to an increase in solution viscosity due to gelation. This phenomenon prevents the crystallization of the metal precursor and inhibits the agglomeration of metal particles (Jos van Dillen et al., 2003).

Most commonly used chelating agents for preparation of metal precursors include nitrilotriacetic acid (NTA) (Medici and Prins, 1996), citric acid (CA) (van de Loosdrecht et al., 1997), ethylenediamine (en) (Zhang et al., 2017), ethylenediaminetetraacetic acid (EDTA) (Ortega-Domínguez et al., 2012), oxalic acid (Wang et al., 2017) and acetic acid (AC) (Zhang et al., 2017). Complexation reactions are dependent on pH of the reaction mixture and hence, pH is closely related to the chelating ability of chelating agents which are stable over a wide range of pH. Application of metal chelated precursors onto various supports such as silica (SiO_2), alumina (Al_2O_3), zirconia (ZrO_2) and extended to mesoporous materials such as SBA-15 depend on the stability of complexes.

Stability of metal complexes follows Irving - Williams series where generally the stability increases as the size of the metal cation decreases exemplified in Figure 2.2. General trend in stability constants for the complexes of some M^{2+} type metal cations can be summarized as follows: $Ba^{2+} < Sr^{2+} < Ca^{2+} < Mg^{2+} < Mn^{2+} < Fe^{2+} < Co^{2+} < Ni^{2+} < Cu^{2+} > Zn^{2+}$.

Influence of metal-chelate precursors on dispersion of Ni on SBA-15 support was studied by Ortega-Domínguez et al. (Ortega-Domínguez et al., 2012). EDTA and citric acid (CA) were used as chelating agents. To investigate the effect of chelating agents, catalysts were synthesized both with and without the use of these agents. Catalysts were prepared using the conventional impregnation method, followed by drying (100°C, 12 h), calcination in air (500°C, 4 h), and reduction in a tubular quartz reactor (400°C, 4 h) with a stream of

H_2/Ar (20% H_2). In first catalyst series, EDTA and CA were selected as chelating agents. Ni(II) – EDTA complex was formed at a pH of approximately 9. As a comparison, $Ni(NO_3)_2$ was used as the precursor for the second type of catalyst without chelating agents. Catalysts with nominal Ni loadings of 5, 10, and 20 wt.% were prepared. The results showed that at 20 wt.% Ni loading, the particle size was 6 nm for the catalyst prepared with Ni(II)-EDTA complex, while it was measured as 18 nm for the $Ni(NO_3)_2$ precursor. This indicates a better dispersion for the Ni(II)-EDTA chelate precursor. However, the catalysts prepared using Ni(II)-CA chelate resulted in larger particle sizes, around 48 nm, indicating even lower dispersion compared to the catalysts synthesized without a chelating agent. In a subsequent study by Ortega-Domínguez et al., the effect of EDTA was investigated in more detail. Ni loading of the catalysts ranged from 1 to 20 wt.%. Catalytic activity and selectivity tests were conducted for the hydrogenation of naphthalene as a model reaction. The results showed that the naphthalene conversion (at 30 min reaction time) for catalysts prepared with the EDTA complex at 20 wt.% was 96.3%, whereas it was 42.0% without the EDTA complex. Results suggest that incorporating EDTA into the impregnation solution during the preparation of Ni/SBA-15 catalysts had a notable positive impact on the dispersion of Ni metal. This enhancement in dispersion ultimately led to an improvement in the activity of the catalyst. (Ortega-Domínguez et al., 2017).

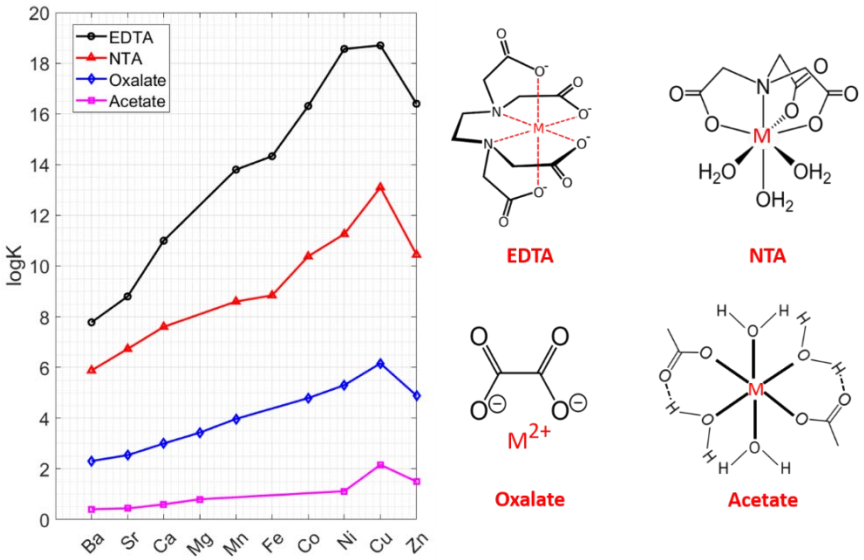

Figure 2.2. Illustration of Irving – Williams effect for selected complexing agents (EDTA, NTA, oxalate and acetate).

In a study conducted by Zhang et al. (Zhang et al., 2017), the researchers investigated the impact of different chelating agents on the dispersion and catalytic activity of the Ni/SBA-15 catalyst in the dry reforming of methane reaction. The study focused on the physicochemical properties of the metallic phase and the support. Catalysts were prepared using a modified version of the dry impregnation method, with a 7.5 wt. % metal loading. Chelating agents such as ethylenediamine (en), citric acid (CA), and acetic acid (AC) were employed and added to a $Ni(NO_3)_2.6H_2O$ solution to obtain a Ni(II)-chelate complexes. SBA-15 was then added to the precursor solution, followed by ultrasonic treatment at 30°C for 2 hours. Catalyst powders were calcined at 500°C in air for 4 hours, with a heating rate of 1°C/min. TEM analysis of the fresh catalysts revealed a uniform distribution of Ni particles with a particle size of less than 6 nm. Due to the high viscosity of the impregnation solution, the particle size remained relatively stable even after the calcination and reduction steps. The Ni(II)-(en) precursor showed the best results, as it could form two five-membered chelate rings with Ni metal. The catalytic performance of the prepared samples was evaluated for the CO_2 reforming of methane reaction within a temperature range of 600°C to 800°C. Long-term catalytic stability experiments were conducted at 700°C for 50 hours. In the case of traditional Ni(II)-nitrate impregnation, there was a significant decrease in CH_4 and CO_2 conversions. The initial CH_4 conversion decreased from 73.3% to 30.9%, while the initial CO_2 conversion decreased from 84.2% to 51.3%. However, the chelated precursors exhibited stable conversions, with CO_2 and CH_4 reaching approximately 85% and 80% conversion, respectively. Furthermore, the modified catalysts demonstrated excellent resistance to coke formation.

In another study on SBA-15 supported NiMo hydrotreating catalyst conducted by Badoga et al. (Badoga et al., 2012) , effect of EDTA as a chelating agent is investigated for different EDTA/Ni molar ratio. Catalyst preparation was done by using sequential dry impregnation mehod. 12.5 wt. % Mo loaded to support with dry impregnation method. Sample was dried (100 ºC, 6 h) and calcined (550 ºC, 5 h). Obtained Mo/SBA-15 catalyst was used to prepare NiMo/SBA-15. 2.5 wt. % of Ni was impregnated by using Ni (II)-EDTA chelate solution. EDTA/Ni molar ratio was adjusted between 0 and 2. Impregnation followed by drying (120ºC, 5 h) and calcination (550 ºC, 6 h). Dispersion of active sites analyzed by using HRTEM. Without EDTA, metal dispersion was found as 8.5% and crystallite size was

14.5 nm while EDTA/Ni ratio was 2, dispersion increase to 18.7 % and crystallite size was 6.5 nm.

Effect of chelating agents on dispersion of Cr/ γ-Al_2O_3 catalysts investigated by Wang et al. (Wang et al., 2017). Chromia/alumina (Cr_2O_3/γ-Al_2O_3) catalysts were prepared by using traditional impregnation technique with addition of citric acid and oxalic acid as chelating agents. During preparation of catalysts, precalcined support at 500ºC were impregnated with Cr(III)-nitrate solutions which contain citric acid or oxalic acid at different weight percents (0, 15, 25, 35 wt.%) for 24 h at 25 ºC. Chromium loading was adjusted to 20 wt. % for each sample. After impregnation part, drying (120ºC, 12 h) and calcination (550ºC, 4h) was followed. Catalyst samples with different contents of citric acid and oxalic acid was tested for activity and selectivity by using the dehydrogenation reaction of isobutane to isobutene at 560ºC and atmospheric pressure. According to SEM results, addition of 25 wt. % of citric acid and oxalic acid resulted in better dispersion. Higher or lower mass fractions resulted with larger particle size and lower dispersion. According to activity test results, addition of chelating agent plays a role in better catalytic performance and stability at 25 wt.% citric acid or oxalic acid addition. Also, by decreasing the acid sites in the catalyst, improves anti-coking ability and inhibits coke formation which was a major cause of catalyst deactivation.

In the study of van de Loosdrecht et al. (van de Loosdrecht et al., 1997), effect of EDTA and citric acid to dispersion on alumina supported cobalt catalysts was investigated. During preparation of catalysts, incipient wetness method was used with three different cobalt precursor solutions ($Co(NO_3)_2.6H_2O$, Co(II)-EDTA and ammonium cobalt citrate). Low loaded (2.5 wt.%) high loaded (5 wt.%) cobalt catalysts were prepared. Co (II)-EDTA complex was formed in ammonia solution (pH at 9). After impregnation samples were dried firstly at room temperature and under air flow, subsequently at 393 K for 2h and finally 393 K for 2 h. TEM images were used to investigating the dispersion of active metal sites. By the use of chelating agents (EDTA and citric acid) relatively small cobalt oxide particles on alumina support were detected.

2.2.2. Thermal Treatment

In order to enhance metal dispersion and ensure catalyst stability, it is essential to carry out controlled drying and calcination steps. The calcination process, particularly after introducing the precursor metal compound, plays a significant role in the formation of robust metal-support interactions. Zhou et al. (Zhou et al., 2015) conducted a study that examined the influence of calcination temperature on metal-support interactions, as well as the catalyst's resistance to sintering and coking. The findings indicated that higher calcination temperatures contribute to the production of more stable catalysts, thereby enhancing their performance during long-term dry reforming of methane (DRM) reaction given below.

$$CH_4 + CO_2 \rightleftharpoons 2CO + 2H_2 \qquad \Delta H_{298\,K} = +247\ kJ\ mol^{-1} \qquad (2.1)$$

In their research, Zhou et al. (Zhou et al., 2015) utilized a Ni/Al_2O_3 catalyst, known for its pronounced propensity for coke formation during the dry reforming of methane (DRM) reaction. This elevated tendency for coke formation arises primarily from the occurrence of methane cracking and the Boudouard reactions, given below:

$$CH_4 \rightleftharpoons C + 2H_2 \qquad \Delta H_{298\,K} = +74.9\ kJ\ mol^{-1} \qquad (2.2)$$

$$2CO \rightleftharpoons CO_2 + C \qquad \Delta H_{298\,K} = -172.5\ kJ\ mol^{-1} \qquad (2.3)$$

Nickel loading of 16 wt. % was achieved through the dry impregnation of $Ni(NO_3)_2.6H_2O$ solution onto Al_2O_3 support with a BET surface area of 130 m^2g^{-1}. Catalyst preparation process involved overnight drying at 110°C, followed by a five-hour calcination step in an air atmosphere. The calcination temperatures utilized were 350°C, 700°C, and 900°C, as reported in the study. The prereduction temperature was determined through H_2 - temperature programmed reduction (H_2-TPR) analysis, performed under a pure H_2 atmosphere at a temperature of 800°C for a duration of 1 hour (Zhou et al., 2015).

According to the XRD analysis, increasing the calcination temperature led to stronger metal-support interactions and the formation of the $NiAl_2O_4$ spinel structure. This structural transformation occurred by overcoming the surface barrier of alumina and integrating the spinel structure into the alumina lattice. To assess catalyst activity in the dry reforming of methane (DRM) reaction, activity tests were conducted using a 20 mg catalyst under a total

flow rate of 160 mL.min^{-1} at a temperature of 700°C. Feed composition consisted of $N_2/CH_4/CO_2$ in a ratio of 2:1:1. Activity was evaluated based on the turn over frequencies (TOF) of both CH_4 and CO_2. Results revealed that the catalyst samples calcined at 350°C and 700°C initially displayed higher activity. However, these samples experienced significant activity loss during the early stages of the reaction. In contrast, the sample calcined at 900°C exhibited the highest stability and demonstrated the lowest deposition of coke, indicating superior performance and resistance to deactivation. (Zhou et al., 2015).

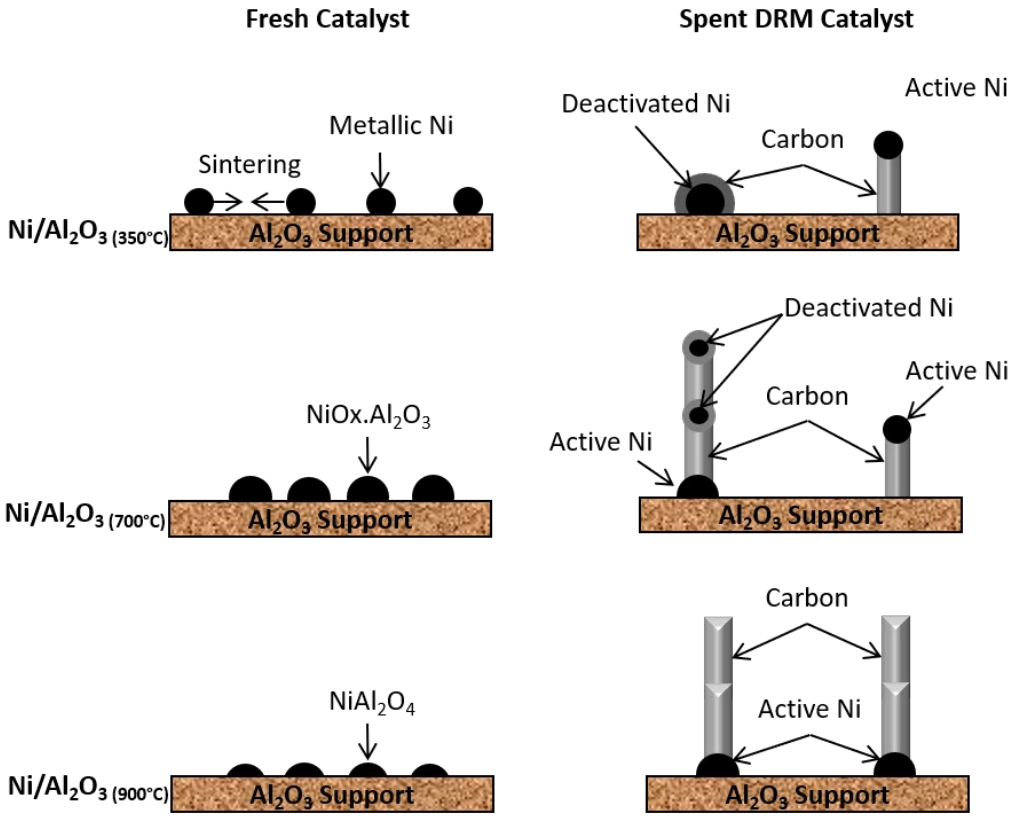

Figure 2.3. Schematic representation of the effect of calcination temperature on carbon deposition mechanism during DRM reaction over Ni/Al_2O_3 catalysts.

Das et al. (Das et al., 2019) conducted a study on the impact of inert thermal annealing on Ni/SiO_2 catalysts, primarily focusing on mitigating Ostwald ripening and minimizing sintering. catalysts were synthesized using the impregnation method, with a nominal Ni loading of 10 wt. %. Nickel (II) acetylacetonate (acac) served as the metal precursor, with acetylacetonate acting as the chelating agent. In the thermal annealing process, the impregnated catalyst was initially dried overnight at 100°C. Subsequently, it was subjected

to heating at 450°C for 30 minutes under an inert atmosphere. The purpose of this step was to thermally decompose the acetylacetonate, transforming it into a carbonaceous deposit that acts as a protective layer on the metal particles, rather than completely eliminating the organic content of the precursor, as typically done through calcination. The resulting carbon layer served to reduce metal sintering and enhance metal dispersion by limiting metal mobility during high-temperature reduction. For comparison, calcined catalyst samples were also prepared by subjecting them to calcination at 600°C for 2 hours. These calcined samples were then reduced under a flow of H_2 gas (20 ml/min) at 600°C for 1 hour. The nickel dispersion on the pyrolyzed Ni/SiO_2 catalyst after reduction was measured to be 10.4 wt.%, while the dispersion of the calcined sample was found to be 3.6 wt.%. The estimated particle size, determined through H_2 chemisorption, was reported as 26.8 nm for the calcined Ni/SiO_2 catalyst and 9.3 nm for the pyrolyzed Ni/SiO_2 catalyst after reduction.

3. EXPERIMENTAL WORK

3.1. Materials

3.1.1. Chemicals

The list of solid and liquid chemicals used for the dispersion improvement experiments in this research is given in the Table 3.1 along with their specifications and application areas.

Table 3.1. Properties and application areas of solid and liquid chemicals used.

Chemical	Formula	Specification	Source	Application
Aluminum oxide	γ-Al_2O_3	High surface area, 1/8″ pellets	Alfa Aesar	Catalyst support, PZC measurements
Ammonium hydroxide	NH_4OH	25% aq. solution for analysis	Merck	Precursor solution preparation
Citric Acid	$C_6H_8O_7$	Anhydrous for synthesis	Merck	Precursor solution preparation
EDTA (Ethylenediamine tetraacetic acid)	$C_{10}H_{16}N_2O_8$	99.4 - 100.6 %	VWR Chemicals BDH	Precursor solution preparation
Lanthanum (III) nitrate hexahydrate	$La(NO_3)_3.6H_2O$	99.9 %	Alfa-Aesar	Support preparation
Liquid Nitrogen	N_2	Liquid	-	BET analysis
Nickel (II) nitrate hexahydrate	$Ni(NO_3)_2.6H_2O$	99.0 - 102.0 %	VWR Chemicals BDH	Catalyst preparation

Table 3.1. Properties and applications of solid and liquid chemicals used. (cont.)

Chemical	Formula	Specification	Source	Application
Nitric Acid	HNO_3	65% aq. solution	Merck	PZC measurement, Precursor solution preparation
NTA (Nitrilotriacetic acid)	$N(CH_2CO_2H)_3$	99 %	Alfa-Aesar	Precursor solution preparation
Sodium hydroxide	NaOH	≥ 99 %	Merck	PZC measurement
Sodium nitrate	$NaNO_3$	≥ 99 %	Carlo Erba Reagents	PZC measurement
Technical buffer pH 4.01	-	±0.02 pH	Mettler Toledo	Calibration of pH meter
Technical buffer pH 7.00	-	±0.02 pH	Mettler Toledo	Calibration of pH meter
Technical buffer pH 9.21	-	±0.02 pH	Mettler Toledo	Calibration of pH meter
Water	H_2O	Ultrapure	-	Precursor solution preparation, PZC measurement

3.1.2. Gases

All the gases used in experiments and listed in Table 3.2 are supplied by the Linde Group, Gebze, Turkey.

Table 3.2. Properties and applications of the gases used.

Gas	Formula	Specification	Application
Argon	Ar	99.995%	Inert
Dry air	-	99.998%	BET degas unit Pneumatic valves
Helium	He	99.999%	Inert
Hydrogen	H_2	99.998%	Reducing agent/Chemisorption analysis
Nitrogen	N_2	99.999%	BET Analysis, To fill manifold and sample tube

3.2. Experimental Systems

This research utilized a comprehensive set of experimental systems, which can be broadly classified into four main categories: support preparation, support characterization, catalyst preparation, and catalyst characterization. Within the catalyst preparation stage, particular attention was given to the preparation and analysis of precursor solutions, which were treated as a subheading under the catalyst preparation systems.

The incipient-to-wetness impregnation (dry impregnation) method was employed for the doping of Lanthanum onto the support for modification and for the loading of nickel during the catalyst preparation stages.

3.2.1. Support Preparation

In this study, the size range of the support material used was determined to be 45-60 mesh size (0.250 - 0.354 mm). γ-alumina pellets with a size of 1/8" were crushed with a

mortar and pestle, then sifted through 45 and 60 mesh sieves with the aid of a vibratory sieve shaker. A schematic of the equipment used for adjusting the support size is shown in Figure 3.1.

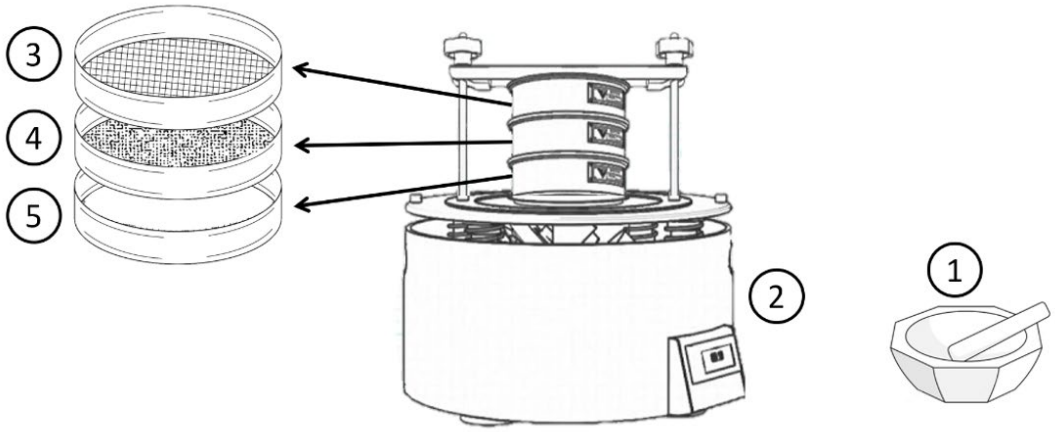

Figure 3.1. Schematic representation of equipment used for support sieving (1. Mortar and pestle, 2. Vibratory Sieve Shaker, 3. Sieve – 45 mesh (354 microns), 4. Sieve – 60 mesh (250 microns), 5. Pan).

A subset of the γ-alumina samples was chosen for modification based on the results of thermal stability studies. The γ-alumina was subjected to a dehumidification treatment at 150°C for 2 hours prior to modification. This treatment aimed to remove any residual moisture from the γ-alumina before further processing. Subsequently, the dehumidified samples underwent calcination in a muffle furnace at 920°C for 4 hours. The purpose of this thermal treatment was to enhance the structural stability of the γ-alumina support by eliminating any remaining volatile components and inducing a high-temperature solid-state transformation. The resulting calcined alumina samples were then used as support materials for subsequent modification experiments.

As an additional modification for the support material, a doping process was performed to introduce 1% Lanthanum. Lanthanum doping onto the support material was achieved using the incipient wetness impregnation method. Figure 3.2 provides an illustration of this impregnation process.

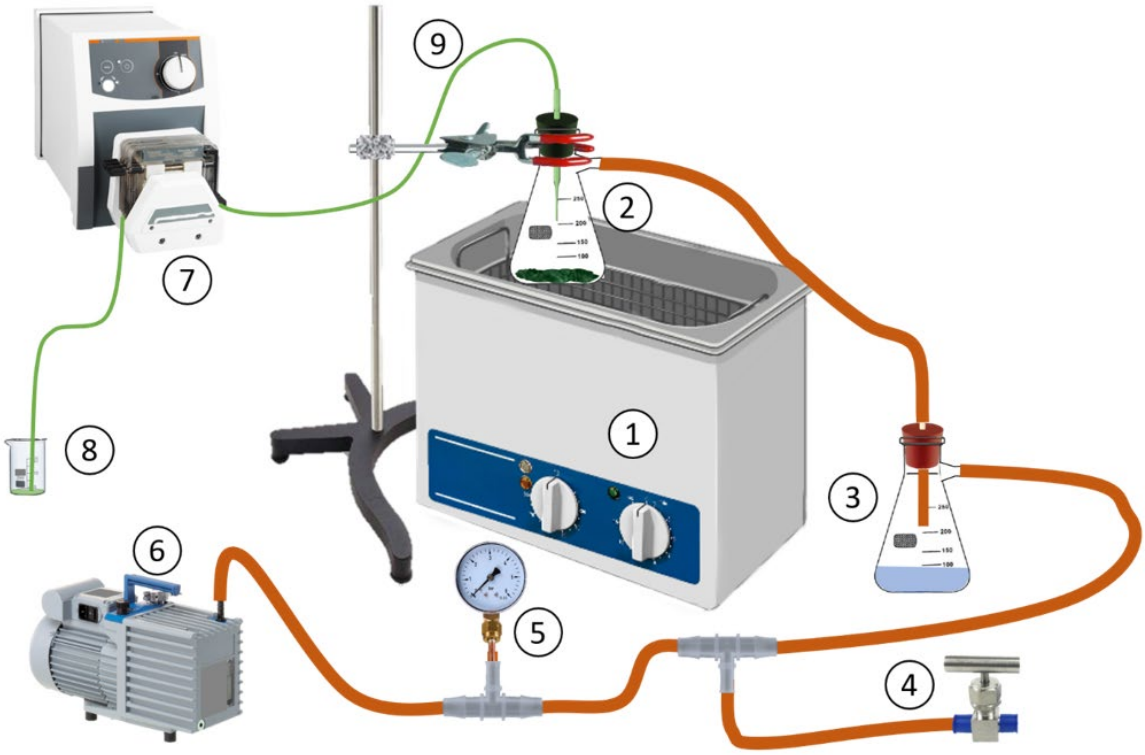

Figure 3.2. Schematic representation of dry impregnation system (1.Ultrasonic bath, 2. Vacuum filtering flask, 3. Vacuum trap, 4. Needle valve, 5. Pressure gauge, 6. Vacuum pump, 7. Peristaltic pump, 8. Beaker, 9. Silicone tubing).

The process began by transferring the precalcined support sample into a vacuum filtering flask, ensuring that it covered the bottom of the flask with a single layer. The vacuum level inside the flask was carefully monitored using a pressure gauge integrated into the system. To adjust the vacuum level, a vacuum pump and a needle valve were employed, allowing precise control of the pressure within the flask. To protect the vacuum pump from potential damage, a vacuum trap was created using another vacuum filtering flask. This trap acted as a safeguard by capturing any liquid or volatile components that could potentially enter the vacuum pump, preventing damage to the pump.

Subsequently, the precursor solution was impregnated onto the support using a peristaltic pump. To enhance the penetration of the solution into the pores of the support, an ultrasonic bath was utilized. This ultrasonic treatment facilitated the entry of the solution into the support material, ensuring a more uniform distribution. The same process was

repeated when impregnating nickel onto the support, following the impregnation steps using the peristaltic pump and the assistance of the ultrasonic bath.

3.2.2. Support Characterization

In this study, the characterization of the support materials was divided into two categories: physical characterization and chemical characterization. These characterization methods were employed to gain insights into the properties and behavior of the support material, which are vital for the successful preparation of a high-quality catalyst.

Physical characterization involves the analysis of various surface properties of the support material. This includes determining the total surface area, pore size distribution, and pore volume distribution. The total surface area measurement provides information on the available surface area for catalytic reactions. The pore size distribution analysis helps understand the distribution of pore sizes within the support material, which can influence factors such as diffusivity and accessibility of reactants and products. The pore volume distribution measurement provides insights into the volume of the pores within the support material.

Chemical characterization primarily involves the determination of the point of zero charge (PZC) of the support material. The PZC represents the pH value at which the surface charge of the material becomes neutral. This characterization parameter provides insights into the surface charge properties of the support material and can have implications for various surface reactions, such as adsorption and ion exchange processes.

3.2.2.1. Physical Characterization of Support Materials. In this study, the specific surface area of the catalyst supports is determined using Brunauer-Emmett-Teller (BET) Surface Area Analysis. This measurement is conducted through the physisorption of nitrogen (N_2) using the Micromeritics 3Flex Surface Characterization Analyzer.

To perform BET analysis, the solid material was exposed to N_2 gas at low temperatures, and the amount of gas adsorbed was measured at different pressures. The data obtained from the measurement was then analyzed using the BET equation given in Equation

3.1, which relates the amount of gas adsorbed to the relative pressure of the gas to calculate the specific surface area of the solid material (Thommes et al., 2015).

$$\frac{z}{(1-z)v} = \frac{(c-1)z}{v_m c} + \frac{1}{v_m c} \qquad where\ z = \frac{P}{P_0} \tag{3.1}$$

The variables in the BET equation include z, which represents the ratio of the equilibrium pressure of N_2 (P) to the saturation pressure of the N_2 (P_0) at the temperature of analysis condition. The BET constant c is related to the heat of adsorption of N_2 in the formation of monolayer (E_1) and, heat of liquefaction of N_2 (E_L) which is given as

$$\mathrm{c} = \exp\left(\frac{E_1 - E_L}{RT}\right). \tag{3.2}$$

Finally, v is the adsorbed gas volume and v_m represents the volume of gas adsorbed onto surface as monolayer. These variables are used to calculate the BET surface area of the material, which is an important parameter for understanding the material's properties. Constants (i.e. c and v_m) is calculated from the $z/(1-z)v$ vs. z graph. In this linear relation, $(c-1)/v_m c$ is the slope and $1/v_m c$ is the intercept. By using volume corresponding to monolayer coverage, v_m, total surface area S_g (m^2/g_{cat}) is calculated by using Equation 3.3. A_m represents the area of one N_2 molecule and w_{sample} is the mass of sample.

$$S_g\left(\frac{m^2}{g}\right) = \frac{\left(\frac{v_m(m^3)}{0.0224\left(\frac{m^3}{mol}\right)} \times 6.02 \times 10^{23}\ (mol^{-1})\right) \times \left(A_m\ (\text{Å}^2) \times \left(\frac{1\ m^2}{10^{20}\ \text{Å}^2}\right)\right)}{w_{sample}(g)} \tag{3.3}$$

The pore geometry of the support material was also evaluated using N_2 physisorption data. The shapes of the hysteresis loops observed in the adsorption-desorption isotherms were analyzed to understand the pore geometry. Additionally, the Barrett-Joyner-Halenda (BJH) pore size distribution method was used to examine the pore size distribution of the support material. The BJH method employs relative pressure to calculate the volume of gas released, which is subsequently used to determine the pore size distribution of the material. The results of these analyses provide a comprehensive understanding of the pore structure and properties of the support material, which are crucial for designing high-quality catalysts and for predicting the catalyst's behavior in various applications.

3.2.2.2. Chemical Characterization of Support Materials. In order to characterize the chemical properties of the support materials, the point of zero charge (PZC) of the support surface was analyzed using the salt addition method. To obtain the PZC, solutions of different pH values were prepared with a total volume of 25 mL and a surface loading of 1000 m^2/L for all support materials. Total surface area values obtained from BET analysis were used to ensure the same surface loading for all support materials. To maintain a constant ionic strength, 20 mL of a 0.1 M $NaNO_3$ solution was added to each solution, and the desired pH value was achieved by adding 5 mL of either HNO_3 or NaOH solution to the mixture.

During the PZC measurement, the prepared solutions were placed in a beaker covered with a watch glass and stirred for 24 hours at a constant temperature using a magnetic stirrer, as shown in Figure 3.3. The initial and final pH values were measured using a spear-shaped pH electrode. pH values were continuously measured by adjusting the initial pH until the point of zero charge was reached.

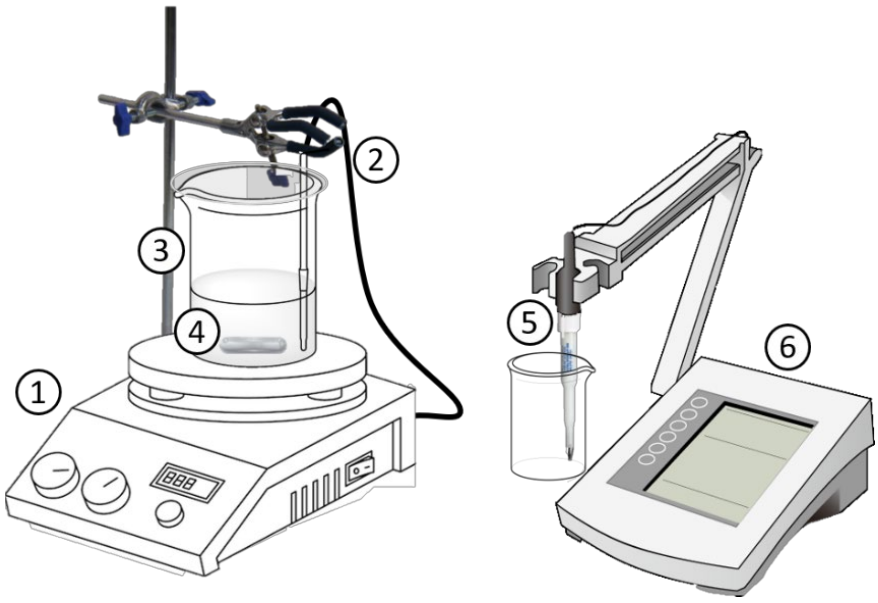

Figure 3.3. Schematic representation of point of zero charge (PZC) measurement system (1.Hot plate magnetic stirrer, 2. Temperature probe, 3. Covered beaker, 4. Magnetic stirring bar, 5. Spear shape tipped ATC Probe with ISM pH electrode, 6. Benchtop pH meter monitor).

Table 3.3. Support materials used for PZC measurements.

Support Type	γ-Al_2O_3	La-doped	δ-Al_2O_3
Amount used (g)	0.1134	0.2174	0.1888

Table 3.4. Initial pH values for PZC measurements.

Number of Trial	**γ-Al_2O_3**	**La-doped**	**δ-Al_2O_3**
	Initial pH of Solution	**Initial pH of Solution**	**Initial pH of Solution**
1	1.86	1.9	1.9
2	11.17	11.17	12.14
3	6.29	6.29	7.05
4	8.62	8.47	9.98
5	7.49	7.31	8.58
6	8.11	7.73	7.57
7	8.31	2.55	3.25
8	2.55	3.22	4.73
9	3.22	4.78	6.25
10	4.78	7.21	9.3
11	5.36	7.49	10.56
12	7.59	7.55	11.17
13	7.87	7.59	
14	9.86	7.64	
15	10.14	9.53	
16	10.29	9.95	

3.2.3. Catalyst Preparation

In the process of catalyst preparation, the widely used conventional incipient to wetness method was employed. The influence of chemical modifications made to the impregnating solution on the dispersion level of the catalyst was investigated.

3.2.3.1. Impregnating Solution Preparation. Impregnating solutions used for catalyst preparation were modified by adjusting their pH values by using NH_3 and HNO_3 based on the data obtained from experiments conducted to determine the point of zero charge (PZC) of the support. To investigate the effect of different complexing agents on nickel dispersion, impregnation was carried out using solutions containing complexes prepared at a 1:1 molar ratio of $Ni(NO_3)_2$ with EDTA, NTA, and Citric Acid.

Formation of complexes was modeled using stability constants, and appropriate pH values of solutions were determined based on the PZC value of the support and the charges of the complexes expected to form according to the model. The presence of targeted complexes in the prepared solutions was confirmed by UV-Vis spectrophotometry. Experimental parameters for the prepared solutions are provided in Table 3.5.

To prepare solutions containing nickel complexes of EDTA and NTA, $Ni(NO_3)_2$ and EDTA or NTA were mixed in a 1:1 molar ratio in solid form. Next, a 25% aqueous NH_3 solution was slowly added to the mixture while continuously monitoring the pH with a pH meter until the appropriate pH was reached to ensure the formation of the desired nickel complexes. Temperature of the solution was maintained at 25°C during the reaction. Mixture was then subjected to ultrasonic mixing in an ultrasonic bath at 35 kHz and 25°C until a clear suspension was obtained.

During the synthesis of the citric acid-nickel complexes with 1:1 molar ratio, firstly, $Ni(NO_3)_2$ and citric acid were dissolved separately in beakers. A 25% aqueous NH_3 solution was added dropwise to the citric acid in an ultrasonic bath until fully dissolved. $Ni(NO_3)_2$ was dissolved in ultrapure water slightly above its solubility limit (1 mL water for 1.7812 g $Ni(NO_3)_2$), and the ammonia-citric acid solution was added dropwise to prevent the formation of $Ni(OH)_2$, while the process was carried out in the ultrasonic bath. Finally, the pH of the resulting clear solution was adjusted to the target value using a 25% aqueous NH_3 solution and ultrapure water.

Table 3.5. Experimental parameters impregnating solution preparation.

Solution	**Nickel precursor compound / Complexing Agent**	**Acid / Base Used for pH Regulation**	**pH Range**	**Predominant Complex in solution**
$Ni(NO_3)_2$ Solution	$Ni(NO_3)_2$ / H_2O	-	≈ 3.5	$[Ni(H_2O)_6]^{2+}$
$Ni(NO_3)_2$ Solution with pH regulation (Below PZC)	$Ni(NO_3)_2$ / H_2O	HNO_3	$0.8 - 0.9$	$[Ni(H_2O)_6]^{2+}$
$Ni(NO_3)_2$ Solution with pH regulation (Above PZC)	$Ni(NO_3)_2$ / NH_3	NH_3	$9.5 - 10$	$[Ni(NH_3)_n(H_2O)_{6-n}]^{2+}$
$Ni(NO_3)_2$ + EDTA (1:1 mol) Solution	$Ni(NO_3)_2$ / EDTA	NH_3	$8.0 - 8.5$	$[NiEDTA(NH_3)]^{2-}$
$Ni(NO_3)_2$ + NTA (1:1 mol) Solution	$Ni(NO_3)_2$ / NTA	NH_3	$6.0 - 6.5$	$[NiNTA(H_2O)_2]^{-}$
$Ni(NO_3)_2$ + Citric Acid (1:1 mol) Solution	$Ni(NO_3)_2$ / Citric Acid	NH_3	$6.0 - 7.0$	$[NiCit]^{-}$

3.2.3.2. Impregnation of Precursor Solution. Support materials were impregnated with solutions prepared based on the specified values in Table 3.5, employing the incipient wetness impregnation method through the system shown in Figure 3.2. Support material was placed into the vacuum filtering flask and kept under vacuum in the ultrasonic bath for 25 minutes. Subsequently, the impregnation solution was gradually applied onto the support material at a controlled rate of 0.4 ml/min, by using a peristaltic pump.

A vacuum pump and a needle valve were employed to maintain a vacuum level of approximately 810 mbar. To ensure consistent ultrasonic bath temperature, the synthesis of

all samples was initiated at 25°C, and the temperature of the bath was monitored and recorded at 25-second intervals using a DS18B20 Digital Thermometer. Following the impregnation process, the samples were subsequently subjected to overnight drying in an oven set at a temperature of 110°C.

3.2.3.3. Calcination of Impregnated Samples. Samples, which had been impregnated with the precursor solution, underwent calcination in an air atmosphere using a muffle furnace. This calcination process was carried out at three distinct temperatures: 500°C, 700°C, and 900°C. Calcination step lasted for a duration of 4 hours.

3.2.3.4. Reduction Procedure of Calcined Samples. Prior to measuring the dispersion levels, the catalyst samples underwent in situ reduction in the U-shaped quartz fixed-bed reactor of the Micromeritics 3Flex Adsorption Analyzer. The samples were heated at a rate of 12°C per minute and reached a temperature of 800°C in approximately one hour. Following this, the samples were subjected to in situ reduction for an hour under a continuous flow of pure H_2 at a flow rate of 50 mL/min.

Table 3.6. Parameters belong to prepared catalyst samples.

Impregnating Solution	**Calc. Temp (°C)**	**Gamma Alumina (γ-Al_2O_3)**	**920°C Precalcined Support (δ-Al_2O_3)**	**920°C Precalc. + 1% La Doped (calc.at 1000°C)**
$Ni(NO_3)_2$ Solution	**500**	Sample 1	Sample 4	Sample 7
	700	Sample 2	Sample 5	Sample 8
	900	Sample 3	Sample 6	Sample 9
$Ni(NO_3)_2$ Solution with pH regulation (Below PZC)	**500**	Sample 10	Sample 13	Sample 16
	700	Sample 11	Sample 14	Sample 17
	900	Sample 12	Sample 15	Sample 18

Table 3.6. Parameters belong to prepared catalyst samples. (cont.)

Impregnating Solution	**Calc. Temp (°C)**	**Gamma Alumina (γ-Al_2O_3)**	**920°C Precalcined Support (δ-Al_2O_3)**	**920°C Precalc. + 1% La Doped (calc.at 1000°C)**
$Ni(NO_3)_2$ Solution with pH regulation (Above PZC)	**500**	Sample 19	Sample 22	Sample 25
	700	Sample 20	Sample 23	Sample 26
	900	Sample 21	Sample 24	Sample 27
$Ni(NO_3)_2$ + EDTA (1:1 mol) Solution	**500**	Sample 28	Sample 31	Sample 34
	700	Sample 29	Sample 32	Sample 35
	900	Sample 30	Sample 33	Sample 36
$Ni(NO_3)_2$ + NTA (1:1 mol) Solution	**500**	Sample 37	Sample 40	Sample 43
	700	Sample 38	Sample 41	Sample 44
	900	Sample 39	Sample 42	Sample 45
$Ni(NO_3)_2$ + Citric Acid (1:1 mol) Solution	**500**	Sample 46	Sample 49	Sample 52
	700	Sample 47	Sample 50	Sample 53
	900	Sample 48	Sample 51	Sample 54

3.2.4. Catalyst Characterization

The objective of this study was to measure the impact of changes in the impregnating solution, different support materials, and various calcination temperatures on the dispersion level of nickel. In order to understand the underlying reasons for changes in dispersion level, surface properties were also analyzed such as the interactions between nickel and support material, pore structure, and phase transitions of the support.

To investigate the interactions that occurred on the surface of support materials during the impregnation stage with $Ni(NO_3)_2$ solution, Raman spectroscopy was employed. After

impregnation with the $Ni(NO_3)_2$ solution, the support materials were dried overnight at 110°C and subjected to analysis Raman spectroscopy.

The samples were analyzed using a Renishaw inVia Raman microscope, which utilized a 514 nm Ar+ laser which has an intensity of approximately 2mW, and each spectrum was acquired with a 10-second acquisition time. To improve the signal-to-noise ratio, each spectrum was accumulated 20 times. Analyses were conducted at the Advanced Technologies Research and Development Center located in Boğaziçi University.

Dispersion analysis of nickel metal on alumina support surface was done by using static H_2 chemisorption measurements performed with Micromeritics 3Flex Surface and Catalyst Characterization Analyzer. Figure 3.4 provides a visual representation of the system.

Calcined catalyst samples were prepared for analysis by degassing under vacuum and at 110 °C for 30 min. Subsequently, the catalyst samples were subjected to reduction in a hydrogen flow at 800°C for 1 hour, with a heating ramp of 12°C per minute. This was followed by an evacuation process at 800°C for 30 minutes. Temperature of the system was allowed to decrease to 35°C in order to obtain H_2 adsorption isotherms at this specific temperature. During the measurements, precise amounts of H_2 gas ranging from 2 mmHg to 450 mmHg were incrementally introduced. Each dose was allowed to equilibrate for a duration of 20 seconds before data collection, ensuring the acquisition of a high-resolution adsorption isotherm. Measurements were repeated to estimate the amount of physically adsorbed hydrogen after the evacuation of sample for 1 hour to remove weakly adsorbed H_2 from catalyst surface.

Difference between the total adsorbed hydrogen quantities (mmol/g) of first and repeated analysis was used to calculate dispersion level of nickel on alumina support by using given equality in Equation 3.4. Adsorption stoichiometry of H_2 on nickel was assumed as one hydrogen atom per nickel atom on support surface.

$$\%\, D = 100 \times \frac{\left[\left(H_{2(First)}\right) - \left(H_{2(Repeated)}\right)\frac{mmol}{gcat}\right] \times 2}{\frac{\left(0.1\ \frac{g\ Ni}{gcat}\right)}{\left(58.71\ \frac{g\ Ni}{mol}\right)} \times \frac{1000\ mmol}{1\ mol}} \tag{3.4}$$

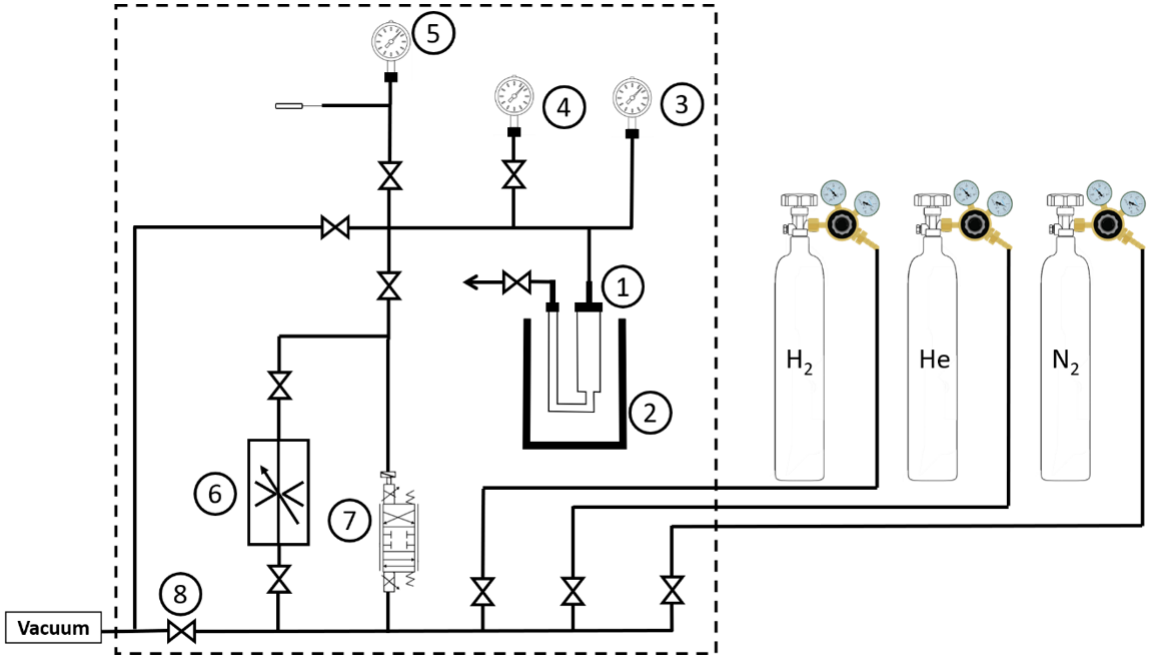

Figure 3.4. Schematic representation of static hydrogen chemisorption system (1. Quartz reactor, 2. Furnace, 3. Manifold pressure gauge, 4. Vacuum gauge, 5. Atmospheric pressure gauge, 6. Mass flow controller, 7. Servo valve, 8. Pneumatic valve).

The pore structure and BET surface area of the selected catalyst samples were analyzed using the N_2 physisorption method, following the examination of obtained dispersion levels. Crystalline structure of selected catalyst samples after reduction was analyzed with Bruker D8 Discover X-ray diffraction system with a copper (Cu) target X-ray generator and a scan speed of 2°/min. Types and amounts of surface Ni-species were analyzed with X-ray photoelectron spectrometer (XPS) by using PHI 5000 VersaProbe III Photoelectron Spectrometer. Analyses were carried out at the SNG&HydTec laboratory located in Boğaziçi University.

4. RESULTS AND DISCUSSION

The catalytic performance of supported metal catalysts is predominantly determined by the level of control over metal-support and metal-metal interactions during manufacturing, which is essential to obtain reproducible products with desirable features such as high activity and selectivity, long-term stability, and low cost. Catalyst deactivation is a persistent problem in industrial processes, particularly in high-temperature reactions, and can occur via sintering, coke formation, and poisoning. For example, nickel-based catalysts used in dry reforming of methane (DRM) are highly prone to deactivation. The importance of mitigating climate change by utilizing greenhouse gases emphasizes the need to improve the activity and thermal stability of nickel catalysts, which are highly catalytically active and cost-effective especially in converting captured carbon to valuable chemicals. Furthermore, the excellent stability of Ni^{2+} cation complexes, which are positioned favorably in the Irving-Williams series, simplifies the formation of transition metal complexes in precursor solutions.

The main objective of this study is to enhance the nickel dispersion level on commercial and modified granular γ- Al_2O_3 supports through the use of a Dry Impregnation (DI) method in which optimized preparation parameters are employed. The present investigation is focused on analyzing the support and precursor solution, as well as the various steps involved in the DI method. This is the initial stage of the work that aims to identify key factors that impact the efficiency of the impregnation process and ultimately to improve the catalyst performance. The findings of this study are expected to contribute to the development of effective catalyst preparation methods for various industrial applications.

4.1. Analysis of Support Properties

Ensuring the long-term stability and sustainability of dispersion levels achieved in manufactured catalysts is a critical concern, especially for reactions that involve high temperatures such as dry reforming of methane. In such cases, thermal stability becomes even more crucial. To analyze the thermal stability of alumina supports, we utilized data from thermal stability studies had been conducted on Al_2O_3 within our research group

(Çelebi, 2021). Granular γ- Al_2O_3 underwent precalcination at 920°C as a thermal treatment, prior to doping with an active metal salt, leading support's phase change from γ- Al_2O_3 to δ- Al_2O_3. Furthermore, 1% La doped onto precalcined Al_2O_3 at 920°C which then calcined at 1000°C was studied just to understand how additives as modifiers affect the support surface and active metal dispersion. Hence, three distinct support materials were employed in this research: commercial γ-Al_2O_3; precalcined Al_2O_3 at 920°C (δ- Al_2O_3); and 1 wt. % La-doped on precalcined Al_2O_3 at 920°C which furtherly calcined upon impregnation at 1000°C. These changes on the support material not only impact its physical properties such as pore size distribution, total surface area, and pore volume, but also affect its chemical characteristics, including the presence and abundance of functional groups and their interactions with metallic species in the precursor solution, then the metal atoms/clusters, which have significant effects on active metal site dispersion.

4.1.1. Surface Physical Properties of Support Materials

In the course of Nitrogen (N_2) physisorption experiments, data were meticulously analyzed to discern the physical properties of the employed support materials. Key parameters, including BET surface area, pore volume, pore size distribution, and adsorption-desorption hysteresis loop characteristics, were specifically examined. These metrics furnished robust insights into the physical attributes of support materials, thereby facilitating a more nuanced understanding of their would-be function within the experimental framework.

As demonstrated by the adsorption-desorption isotherms in Figure 4.1, a divergence occurs between middle section of the desorption isotherm and the adsorption isotherm. This results in an adsorption hysteresis loop, consistent with a type IV(a) curve according to the IUPAC classification, indicative of presence of mesopores in the support samples and the occurrence of capillary condensation (Thommes et al., 2015).

Insight into the pore structure of the adsorbent is provided by the type of hysteresis loop. In low-temperature nitrogen adsorption experiments, the hysteresis loops of the support samples are identified as type H1, according to IUPAC classification. A type H1 hysteresis loop is typically displayed by materials in the absence of pore blocking or cavitation-induced

evaporation, and is characteristic for those with independent pores and organized three-dimensional pore networks (Thommes et al., 2015). Observation of similar hysteresis loop shapes provides evidence that there is no discernible alteration in the pore tortuosity of the support materials.

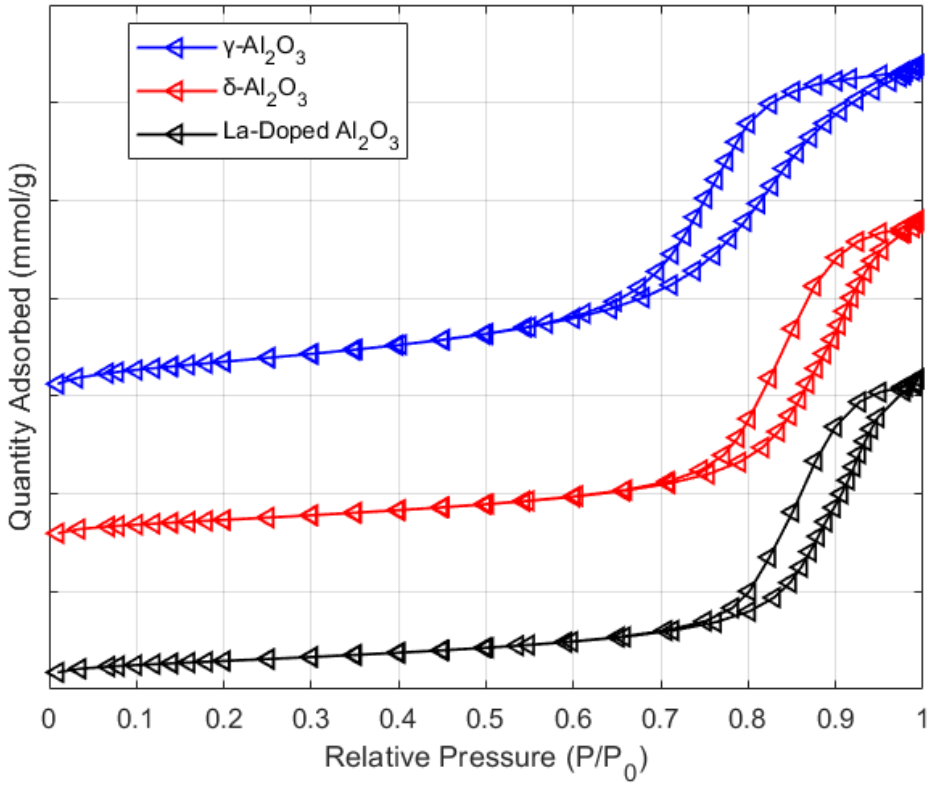

Figure 4.1. Low-temperature N_2 adsorption/desorption isotherms of support materials.

During preparation of the catalysts, support materials are impregnated with nickel compounds to disperse active material on the surface and on the inner pore walls. A primary factor affecting dispersion level is the pore size distribution (PSD); overly small pores can hinder effective penetration of the precursor solution while excessively large one's risk is uneven dispersion and easy agitation. PSD also plays an essential role in determining catalyst's stability; well-sized pores help secure a reaction by preventing leaching and/or sintering (aggregating) during the reaction. This is crucial for maintaining long-term catalytic activity.

In Figure 4.2, the distribution of pore sizes in the support materials is demonstrated. This is depicted as a graph where pore width (representing the size of the pores) is plotted

against differential pore volume (indicating the volume taken up by pores of a specific size). The dV/dw curves have been specifically chosen to emphasize the significance of smaller pore ranges in mesoporous pore systems of support materials (Liu and Ostadhassan, 2019).

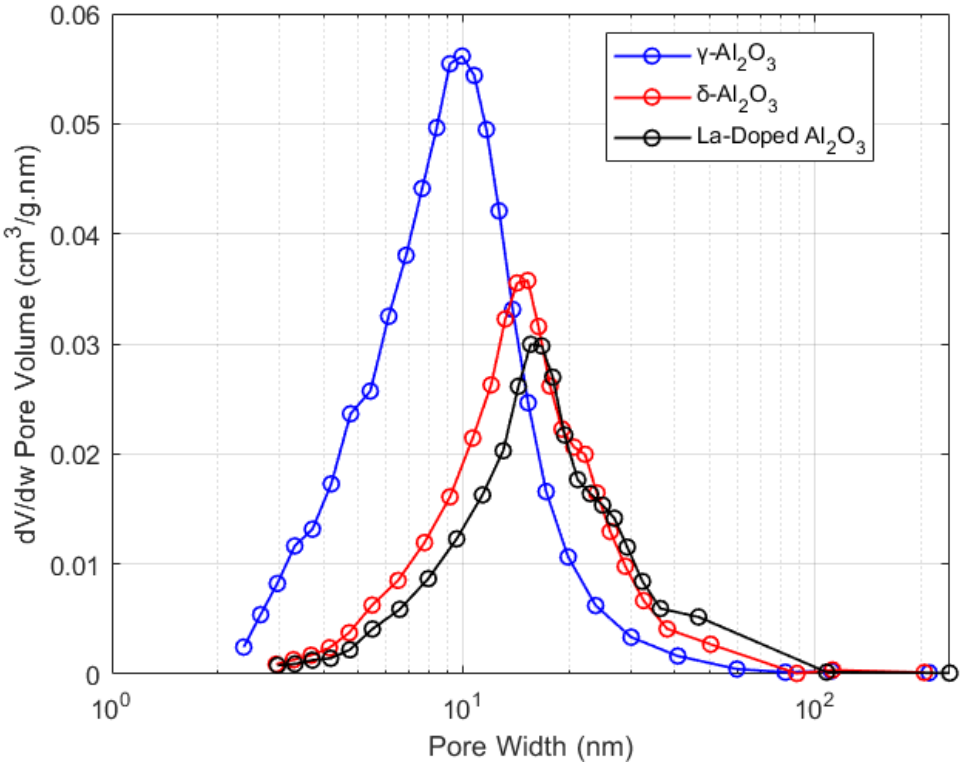

Figure 4.2. dV/dw Pore volume ($cm^3/g \cdot nm$) vs. pore width (nm) of support materials calculated by BJH model.

According to the results of average pore width measurements, it is evident that the thermal treatment has caused an enlargement or expansion of the pores of the support material. This expansion can be attributed to various factors, including the removal of adsorbed species, thermal decomposition or restructuring of the support material, or changes in the surface chemistry.

Additionally, the decrease in the dV/dw value indicates a reduced rate of change in pore volume with increasing pore width. This observation suggests that thermal treatment has selectively impacted the larger pores in the alumina support material. While the larger pores have experienced some expansion, this has been relatively less significant compared to the expansion observed in smaller pores.

4.1.2. Point of Zero Charge of Support Materials

Interactions between support surface groups and the metal precursor compound are of an electrostatic nature. Considering the characteristics of electrostatic forces, when support surface carries an opposite charge to that of the precursor metal compound, it enhances the interaction between the support and metal. As a result, this prevents the agglomeration of the precursor compound and promotes increased dispersion of the metal compound on the surface.

Surface charge of Al_2O_3 support can be adjusted by protonation / deprotonation of the terminal hydroxyl groups on the surface. Therefore, the pH of the precursor solution used during the adsorption process of the metal compound onto the support surface directly affects the surface charge and the formation of electrostatic interactions between the metal compound and the support. As depicted in Figure 4.3, when the pH is above the point of zero charge (PZC), for which the support surface is neutrally charged, the surface of the alumina support becomes negatively charged due to the deprotonation of hydroxyl groups. Conversely, when the pH is below the PZC, the surface becomes positively charged as a result of the protonation of hydroxyl groups (Zhu et al., 2013).

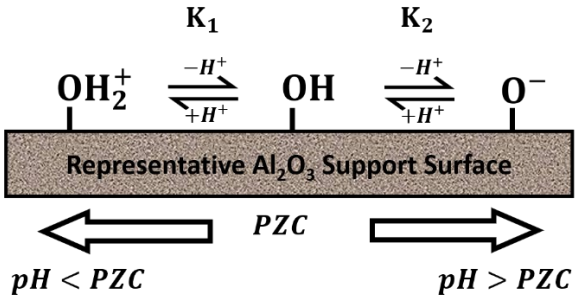

Figure 4.3. Schematic representation of protonation and deprotonation of surface hydroxyl groups according to the solution pH on Al_2O_3 support.

Determination of PZC for the selected alumina supports is done by using salt addition method (Mahmood et al., 2011). In this method, ionic strength of solution and surface loading are control parameters which have effect on surface charge of support material. Ionic strengths of all solutions were kept fixed at around 0.08 M by using 20 mL of 0.1 M $NaNO_3$

solution which suppress effect of other ions on ionic strength. Surface loading was selected as 1000 m^2/L for selected Al_2O_3 supports and its calculation is given as

$$\mathrm{SL} = \frac{m_{support} \times S_g}{V_{solution}}. \tag{4.1}$$

Volume of solution was chosen as 25 mL. Total surface areas (S_g) of Al_2O_3 support samples were determined by using BET analysis. BET surface area results and mass of support samples added in solutions are tabulated in Table 4.1.

Table 4.1. BET surface areas and sample amounts of selected supports in suspensions.

Support	**BET Surface Area (m^2/g)**	$m_{support}$ **(g)**
$\gamma - Al_2O_3$	220.51	0.1134
Precalcined Al_2O_3 (at 920°C)	132.39	0.1888
Precalcined and 1% La-doped Al_2O_3	114.98	0.2174

To ensure the attainment of equilibrium, all suspensions were vigorously stirred for a period of 24 hours prior to the final pH measurement. Initial and final pH values of the suspensions for the three selected supports are tabulated in Table 4.2. Analysis of the initial and final pH values was carried out to estimate PZC by using Figure 4.4, Figure 4.5 and Figure 4.6. ΔpH values represent the disparity between initial and final pH values.

Table 4.2. pH measurements of suspensions for PZC determination.

γ-Al_2O_3 Suspensions		**δ-Al_2O_3 Suspensions**		**1% La-doped Al_2O_3 Suspensions**	
Initial pH	**Final pH (After 24 h)**	**Initial pH**	**Final pH (After 24 h)**	**Initial pH**	**Final pH (After 24 h)**
1.86	3.26	1.9	4.01	1.9	3.94
2.55	5.41	3.25	6.95	2.55	4.96
3.22	6.79	4.73	8.33	3.22	6.88
4.78	8.37	6.25	8.41	4.78	7.76
5.36	8.44	7.05	8.41	6.29	7.80
6.29	8.46	7.57	8.41	7.21	7.80
7.49	8.47	8.58	8.42	7.31	7.80
7.59	8.47	9.3	8.46	7.49	7.80
7.87	8.47	9.98	8.62	7.55	7.80
8.11	8.47	10.56	9.06	7.59	7.81
8.31	8.48	11.17	10.05	7.64	7.81
8.62	8.49	12.14	11.01	7.73	7.81
9.86	8.85			8.47	7.88
10.14	9.05			9.53	8.12
10.29	9.11			9.95	8.36
11.17	10.12			11.17	10.30

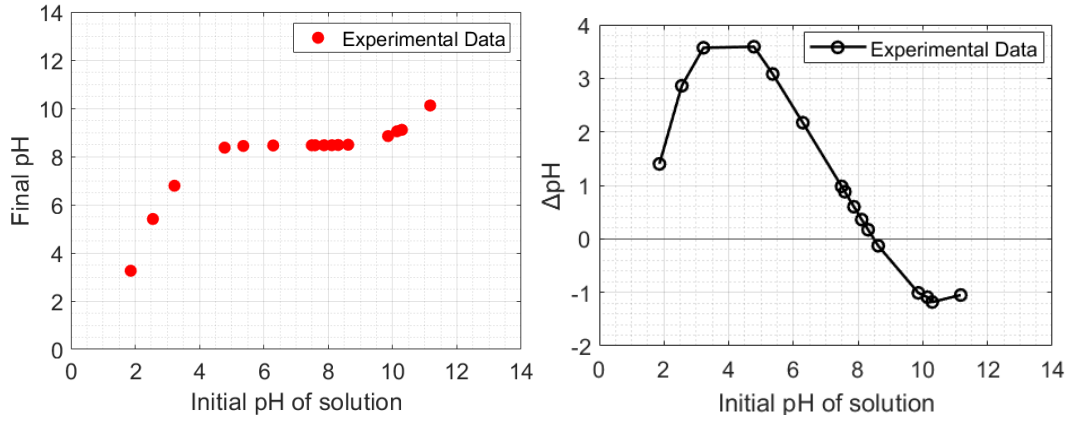

Figure 4.4. PZC measurement results of γ- Al_2O_3 suspensions.

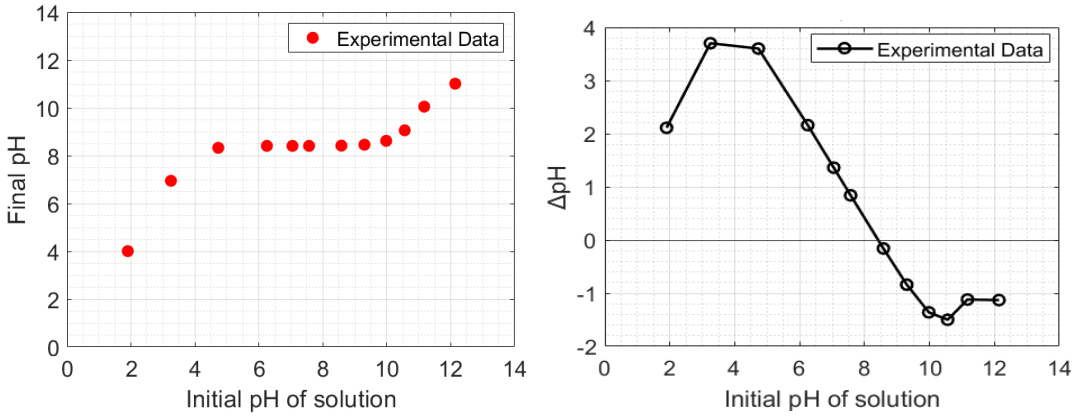

Figure 4.5. PZC measurement results of δ-Al_2O_3 suspensions.

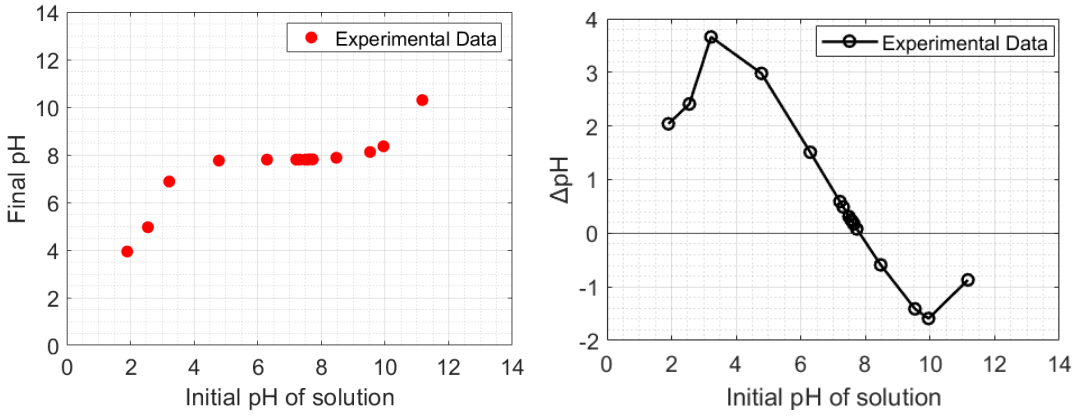

Figure 4.6. PZC measurement results of 1% La-doped Al_2O_3 suspensions.

In accordance with the 2-pK charging model approach, behavior of the Al_2O_3 surface can be likened to that of a diprotic acid. Surface acidity can be modelled by using protonation/deprotonation equilibriums, which can be written as

$$\mathrm{Al-OH_2^+} \rightleftharpoons \mathrm{Al-OH + H_s^+} \tag{4.2}$$

$$\mathrm{Al-OH} \rightleftharpoons \mathrm{Al-O^- + H_s^+}, \tag{4.3}$$

where H_s^+ denotes the protons near the support surface. Intrinsic acid dissociation constants for reactions given in Equation 4.2 and Equation 4.3 can be written as

$$K_1 = \frac{[Al-OH][H_s^+]}{[Al-OH_2^+]} \tag{4.4}$$

$$K_2 = \frac{[Al-O^-][H_s^+]}{[Al-OH]}. \tag{4.5}$$

It is perceptible that Al_2O_3 surface behaves as a pH buffer and pH of the solution is closely related to the surface charge. As the pH of the medium increases, the equilibrium of reactions described in in Equation 4.2 and Equation 4.3 shifts towards the right, leading to an increase in the negative charge on the support surface. Conversely, a decrease in pH results in the opposite effect. Consequently, around PZC, Al_2O_3 exhibit resistance to dramatic pH changes, which is reflected in the plateau observed around the pH of PZC, as depicted in Figure 4.4, Figure 4.5 and Figure 4.6. At the pH of PZC, the difference between the initial and final pH of the solution must be zero once equilibrium is attained. The initial pH value, where the change in solution pH is zero, was determined by interpolating the experimental data obtained and is tabulated in Table 4.3.

Table 4.3. Experimental PZC values of selected supports.

Support	**PZC**
$\gamma - Al_2O_3$	8.49
Precalcined Al_2O_3 (at 920℃)	8.42
Precalcined and 1% La-doped Al_2O_3	7.82

PZC values were used to develop a simple non-Nernstian model incorporating the Gouy-Chapman model of diffuse double layer to predict the pH shifts associated with the support properties with different impregnating solutions. Details of calculations can be found in Appendix B, while the MATLAB computer code used in the analysis is provided in Appendix C. The characterization of the support surface involved experimental determination of the PZC and total surface area, and literature values of ΔpK (Hao et al., 2003) and surface hydroxyl densities N_s (Kittaka, 1974) were also taken into account. To assess the adequacy of the obtained models in comparison with the experimental data, the results are presented in Figure 4.7, Figure 4.8 and Figure 4.9.

Deviations between the model and experimental data are attributed to several factors, including the sensitivity of the pH meter probe used, CO_2 absorption due to prolonged exposure to the atmosphere, and the high ionic strength of the solution. Additionally, certain assumptions made during the model development contribute to these discrepancies. Nevertheless, the deviations are relatively minor and do not significantly impact the validity of the model. Hence, it was employed as a reliable foundation for predicting changes in both the impregnation solution and the support surface.

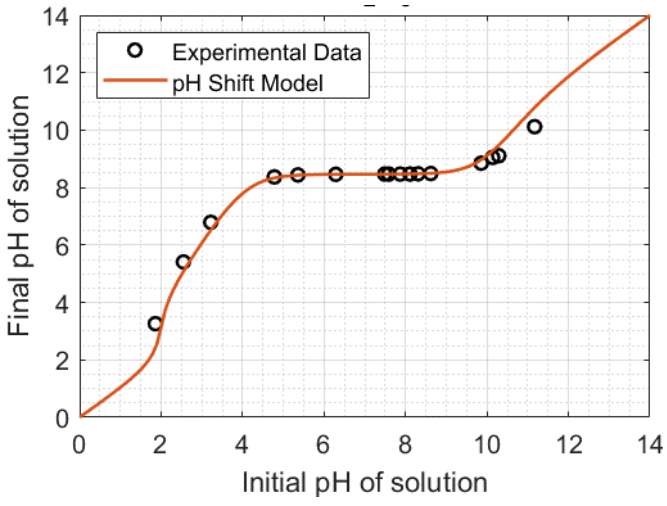

Figure 4.7. pH shifts for γ- Al_2O_3 suspensions (SL = 1000 m^2/L, ΔpK = 5.0, TSA = 220.51 m^2/g, N_s = 8 OH/nm^2).

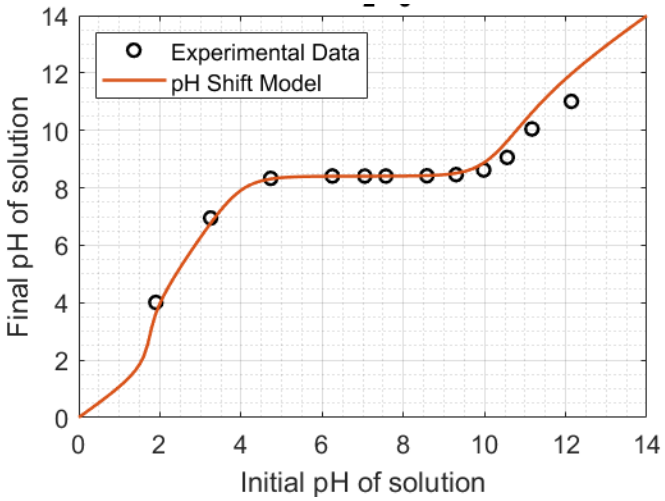

Figure 4.8. pH shifts for δ- Al_2O_3 suspensions (SL = 1000 m^2/L, ΔpK = 5.0, TSA = 132.39 m^2/g, N_s = 14.34 OH/nm^2).

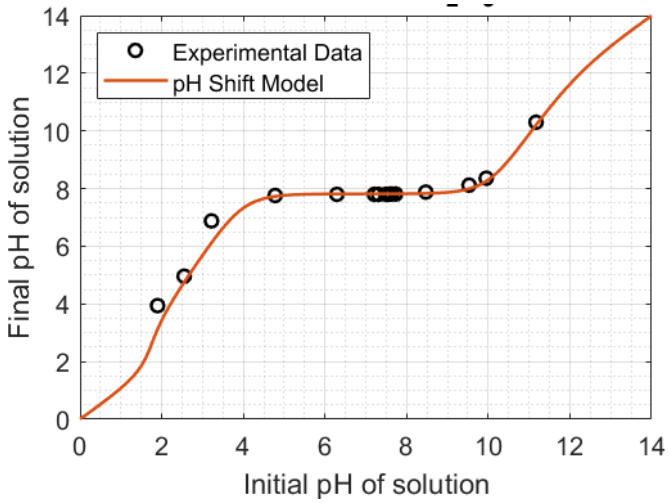

Figure 4.9. pH shifts for La-Doped Al_2O_3 suspensions (SL = 1000 m^2/L, ΔpK = 5.0, TSA = 114.98 m^2/g, N_s = 14.7 OH/nm^2).

System parameters were adjusted to simulate the adsorption of Ni^{2+} ions on each support type in an impregnating solution containing $Ni(NO_3)_2$ for specifically focusing on the pH dependency for a 10 wt.% Ni loading. The resulting pH changes in the impregnating solution, surface charge, and surface potentials were calculated. Cationic uptakes by RPA model, which is based on the Langmuir adsorption model, assuming a simple electric double layer where all species adsorb on a single plane. Further details of this revised physical adsorption model, along with the corresponding MATLAB codes, can be found in Appendix

B and Appendix C, respectively. The results of the simulations are presented in Figure 4.10, Figure 4.11 and Figure 4.12.

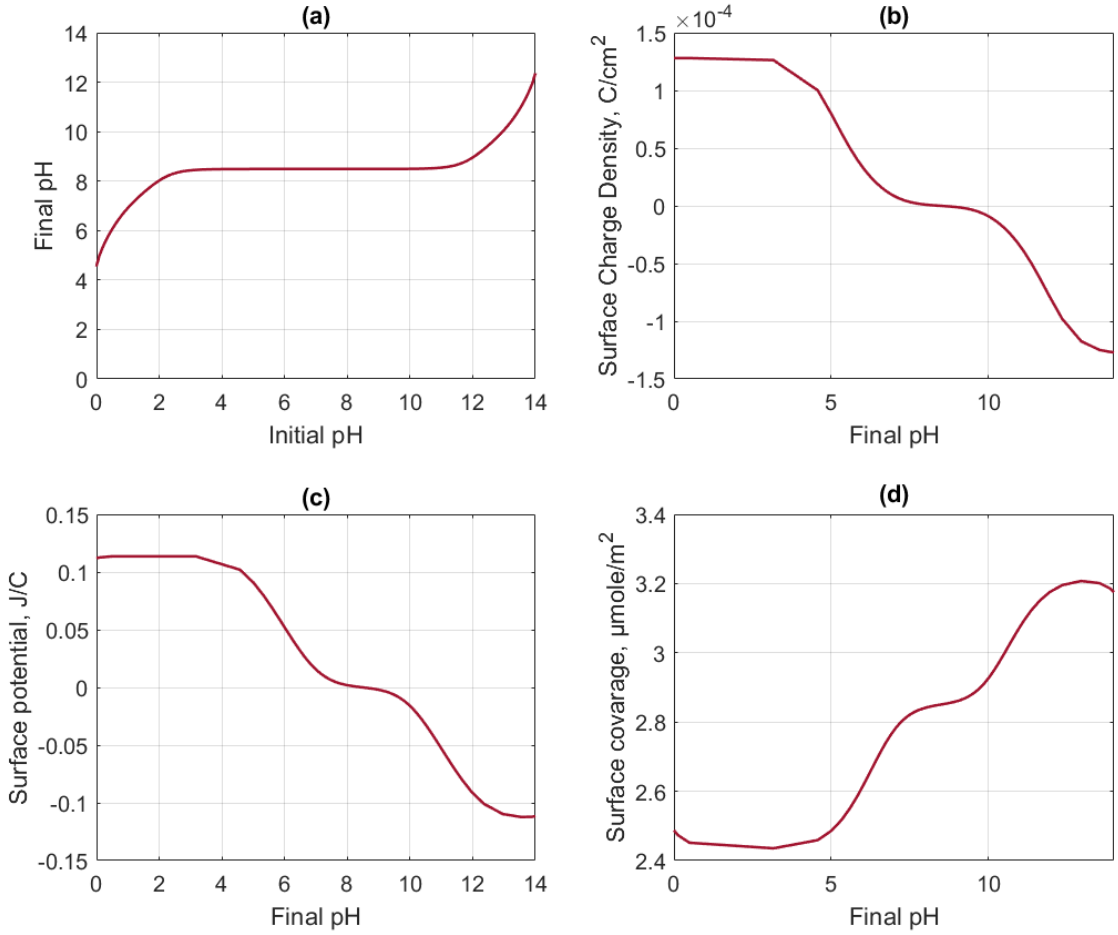

Figure 4.10. Results of simplified RPA model for cationic Ni ($[Ni(H_2O)_6]^{2+}$) uptake by γ-Al_2O_3 support (a) pH shift, (b) Surface charge changes with pH, (c) Surface potential changes with pH and (d) Surface coverage-pH calculations

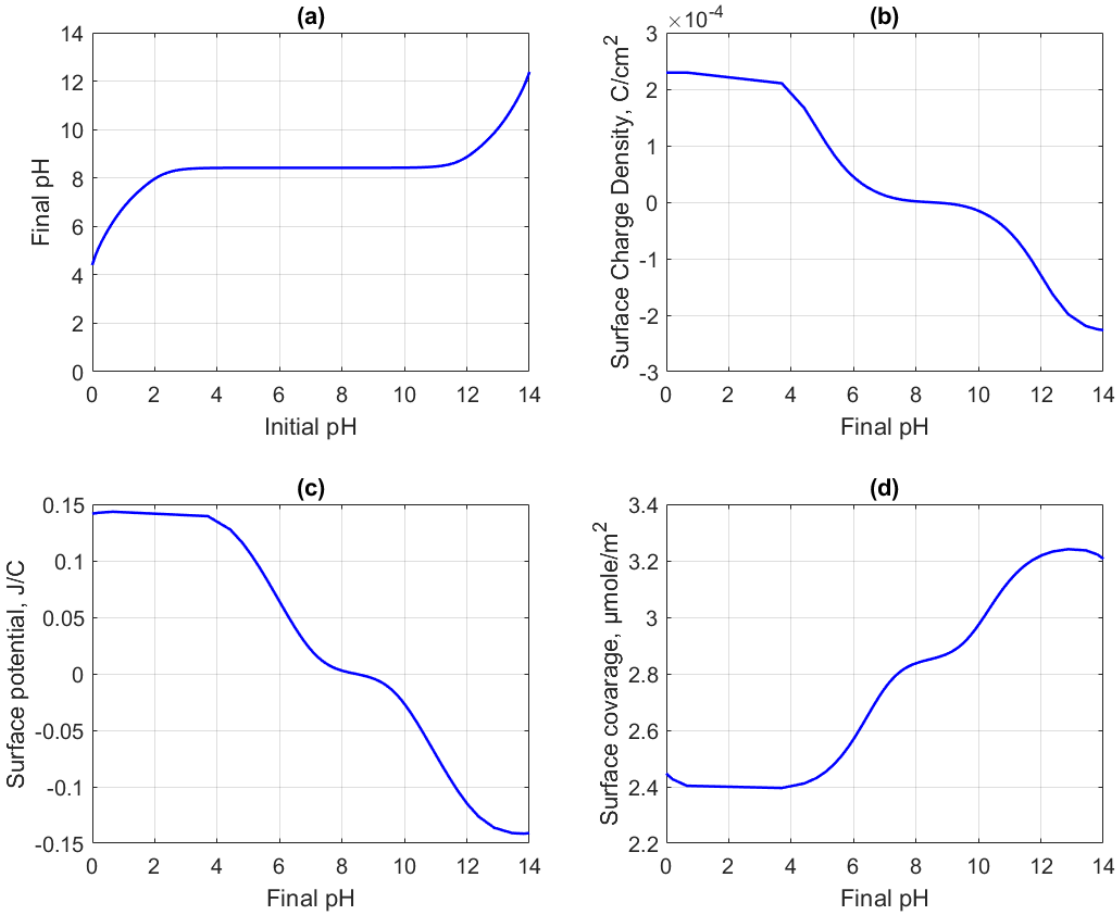

Figure 4.11. Results of simplified RPA model for cationic Ni ($[Ni(H_2O)_6]^{2+}$) uptake by δ-Al_2O_3 support (a) pH shift, (b) Surface charge changes with pH, (c) Surface potential changes with pH and (d) Surface coverage-pH calculations

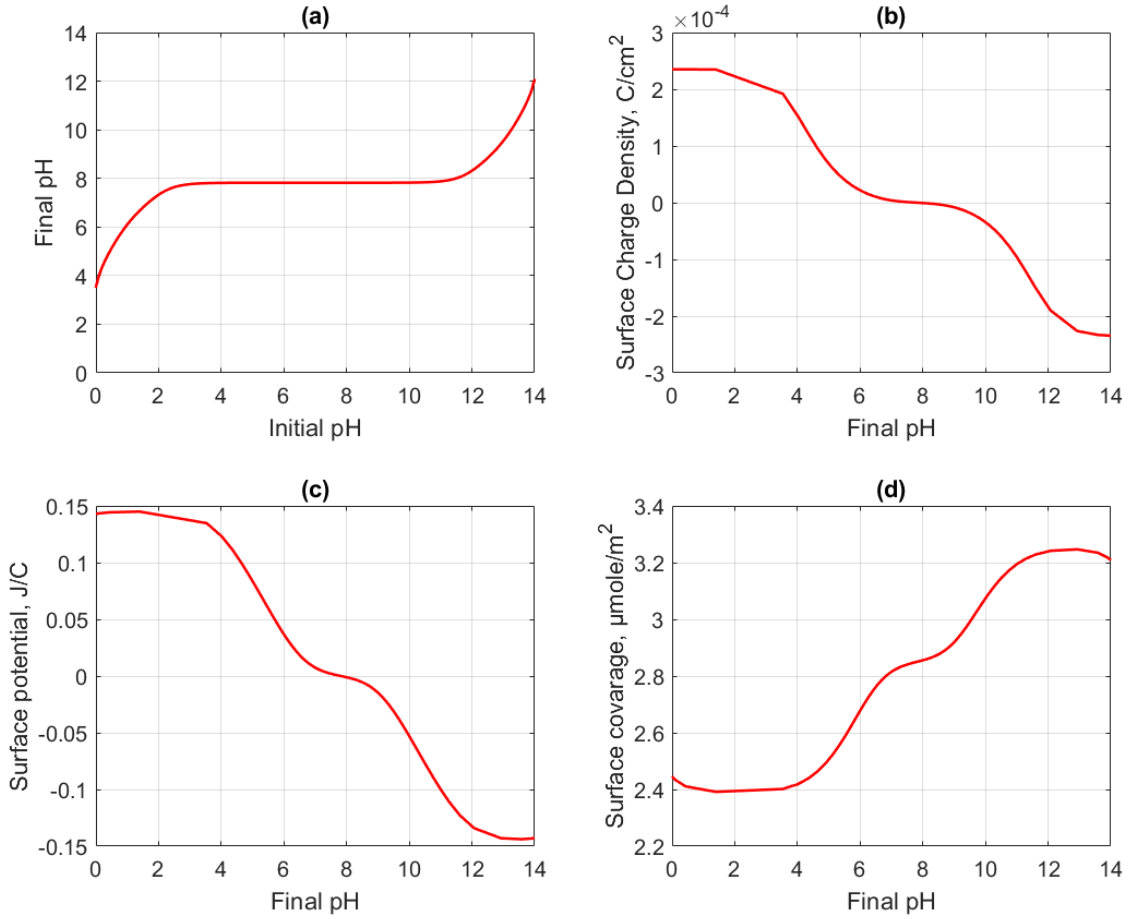

Figure 4.12. Results of simplified RPA model for cationic Ni ($[Ni(H_2O)_6]^{2+}$) uptake by La-Doped Al_2O_3 support (a) pH shift, (b) Surface charge changes with pH, (c) Surface potential changes with pH and (d) Surface coverage-pH calculations.

Due to the robust buffering capacity of the support surface, the equilibrium pH of the impregnating solution is typically maintained around the point of zero charge (PZC), except under extremely acidic or basic conditions. To achieve the maximum level of adsorption, the pH of the impregnating solution should be extremely basic, as indicated in Table 4.4. However, the simplified RPA model is unable to predict the changes in the Ni species within the impregnating solution with respect to pH variations. Therefore, a thermodynamic analysis of the impregnating solution was conducted, utilizing the equilibrium constants provided in Table A.1 and Table A.2.

Table 4.4. Equilibrium pH for maximum Ni^{2+} uptake according to simplified RPA model.

Support Type	**Surface Loading (m^2/L)**	**Final pH for Maximum Adsorption**
$\gamma - Al_2O_3$	222950	12.96
Precalcined Al_2O_3 (at 920°C)	133850	12.87
Precalcined and 1% La-doped Al_2O_3	116250	12.93

Results of complexation-precipitation equilibrium calculations given in Figure 4.13 shows that solid $Ni(OH)_2$ formation occurs at high pH levels. Even at low initial pH conditions, final pH of solution will be close to the PZC value and $Ni(OH)_2$ will be formed on support surface. The resulting $Ni(OH)_2$ has PZC at around 7.9 which is close to those of the support materials, thus adsorption of nickel species wouldn't be efficient. To avoid accumulation of $Ni(OH)_2$ particles on support surface which decreases the dispersion level of Ni metal, formation of Ni species in impregnating solution should be delicately controlled. Therefore, suitable complexing agents were used to increase solubility of Ni species at basic pH levels and for the adjustment of Ni species in impregnating solution.

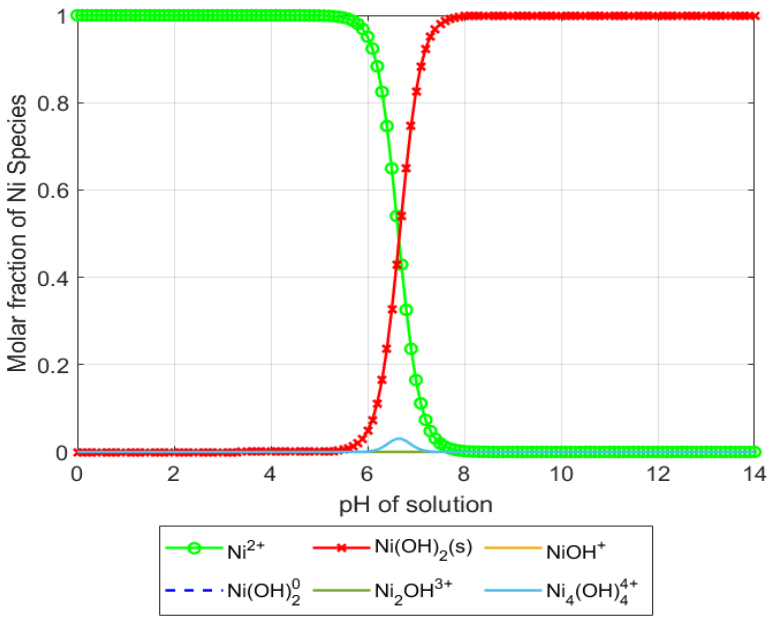

Figure 4.13. Thermodynamic predictions of the Ni species in impregnating solution of $Ni(NO_3)_2$ as a function of pH.

4.2. Analysis and Adjustment of Impregnating Solution

To achieve the desired pH values, HNO_3 was used for achieving acidic conditions, while NH_3 was employed for having basic conditions during pH adjustments. The advantage of using HNO_3 and NH_3 is that they can be easily removed from the catalyst surface during the calcination stage without requiring an additional procedural step. Furthermore, based on the Hofmeister anion series, NO_3^- ions generate a strong double layer on the surface of colloidal support particles, thereby improving dispersion through the salting-in effect. Consequently, the compound $Ni(NO_3)_2$ was chosen as the source of nickel metal for complexation and chelation reactions.

Catalyst samples prepared using the conventional incipient wetness method were treated with a simple nickel nitrate solution without pH adjustment (pH ≈ 3.5). Nickel speciation in the impregnating solutions was analyzed using an Ultraviolet-visible (UV-Vis) spectrophotometer within the wavelength range of 340 to 900 nm. The UV–vis spectra for the nickel nitrate solution exhibit peaks at 394 nm and a doublet at 656 nm - 718 nm, indicating the presence of the aqua complex of the Ni^{2+} cation, $[Ni(H_2O)_6]^{2+}$, as illustrated in Figure 4.14.

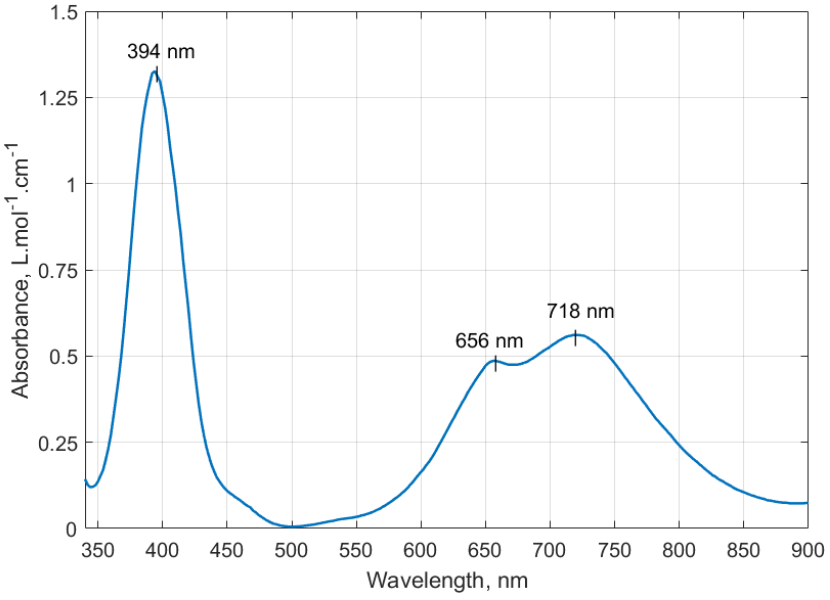

Figure 4.14. UV-Vis Spectrum for $Ni(NO_3)_2$ solution prepared at pH=3.5.

In accordance with the PZC calculations, impregnating solutions were prepared with initial pH values around 0.8 to prevent the formation of $Ni(OH)_2(s)$ during the impregnation step. It was observed that the nickel species in the impregnating solution remained unchanged compared to the nickel nitrate solution prepared at pH 3.5. This consistency was confirmed by analyzing the UV–vis spectra, as depicted in Figure 4.15.

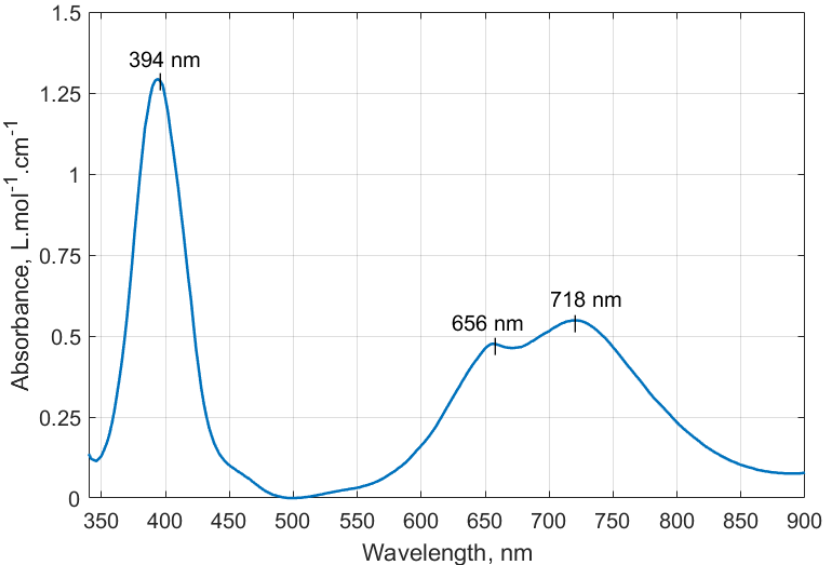

Figure 4.15. UV-Vis Spectrum for $Ni(NO_3)_2$ solution prepared at pH=0.8.

In order to enhance the crystal field stabilization of Ni^{2+} ion, complexing agents were utilized. Ligands containing nitrogen and carboxylate groups, which are positioned lower in the spectrochemical series compared to water, exhibit greater crystal field stabilization in their complexes than the aqua complex of Ni^{2+} (Martell and Hancock, 2013). As a result, water molecules in the aqua complex of nickel, $[Ni(H_2O)_6]^{2+}$, can be displaced by these ligands.

In order to achieve a higher level of dispersion, charges of nickel species formed in the presence of the selected ligands should be negative at pH values below PZC and positive above PZC. Complexing agents selected for this study are ammonia, Ethylenediaminetetraacetic acid (EDTA), Nitrilotriacetic acid (NTA), and citric acid (CA). These agents were selected based on their ability to form complexes with nickel and that they can provide desired charge characteristics for achieving optimal dispersion.

Distribution diagram illustrating all the species present in the solution upon adding 10.05 M NH_3 to 1.91405 M $Ni(NO_3)_2$ has been constructed in Figure 4.16.

The concentrations of each species in the solution were calculated by solving the system of simultaneous mass balance equations for $Ni(NO_3)_2$ and NH_3 written as

$$\begin{aligned} c_{Ni(NO_3)_2} &= [Ni^{2+}] + [\mathrm{Ni}(NH_3)^{2+}] + [\mathrm{Ni}(NH_3)_2^{2+}] + [\mathrm{Ni}(NH_3)_3^{2+}] \\ &\quad + [\mathrm{Ni}(NH_3)_4^{2+}] + [\mathrm{Ni}(NH_3)_5^{2+}] + [\mathrm{Ni}(NH_3)_6^{2+}] + \frac{n_{Ni(OH)_2(s)}}{V_{sol}} \end{aligned} \quad (4.6)$$

$$\begin{aligned} c_{NH_3} &= [NH_3] + [NH_4^+] + [\mathrm{Ni}(NH_3)^+] + 2[\mathrm{Ni}(NH_3)_2^{2+}] \\ &\quad + 3[\mathrm{Ni}(NH_3)_3^{2+}] + 4[\mathrm{Ni}(NH_3)_4^{2+}] + 5[\mathrm{Ni}(NH_3)_5^{2+}] \\ &\quad + 6[\mathrm{Ni}(NH_3)_6^{2+}] \end{aligned} \quad (4.7)$$

by taking into account the complex equilibrium, acid-base equilibrium, and precipitate equilibrium equations to determine the equilibrium concentrations using the equilibrium constants provided in Table A.1, Table A.2, Table A.3 and Table A.4.

For the aqueous NH_4OH, presence of multiple Ni species in the impregnating solution is expected. These complexes are predicted to carry positive charges in solution. To enhance the interactions between the Ni complexes and the support surface, it is important to ensure that the pH value of the impregnating solution is above the PZC of the support material. This will result in a negatively charged support surface, facilitating the interaction with the positively charged Ni complexes.

To prevent the precipitation of bulk $Ni(OH)_2(s)$, the impregnating solution was prepared with a pH value maintained at approximately 9.5. This pH value was chosen to ensure that the concentration of hydroxide ions is sufficient to prevent the precipitation of $Ni(OH)_2(s)$ while still maintaining the desired interactions between the Ni complexes and the support surface.

The UV-Visible spectrum of the impregnating solution at pH 9.5 is given in Figure 4.17. This spectrum provides information about the absorption of light by the species present

in the solution, allowing for the characterization and analysis of the Ni species in the impregnating solution at this particular pH value.

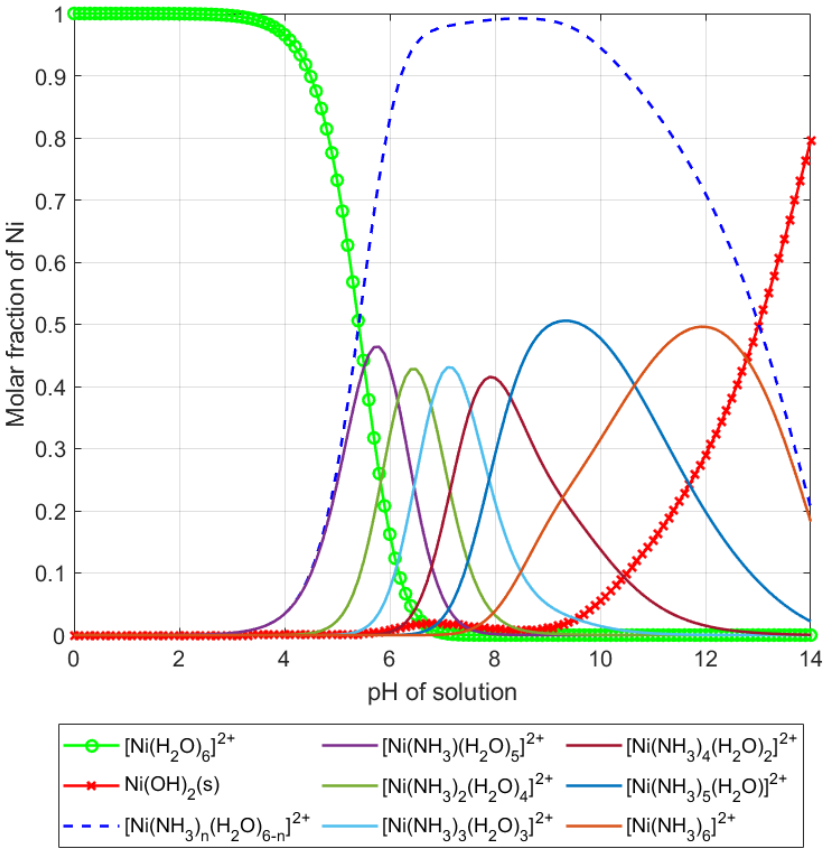

Figure 4.16. Thermodynamic predictions of Ni species in ammonia solution as a function of pH.

Presence of ammonia in the impregnating solution leads to a noticeable shift in the maximum wavelengths of the $[Ni(H_2O)_6]^{2+}$ complex , as observed in Figure 4.14 and Figure 4.15. Specifically, the maximum wavelengths shift towards smaller values, indicating the formation of new complexes and species within the solution. In addition, the presence of $Ni(OH)_2(s)$ particles formed in the impregnating solution contributes to the absorbance observed in the UV-Visible spectrum. It is important to note that the observed shifts in the maximum wavelengths and the contribution of $Ni(OH)_2(s)$ particles to the spectrum are indicative of the presence of different species and complexes in the solution (Shi et al., 2021). These changes provide valuable insights into the interactions and transformations occurring within the impregnating solution.

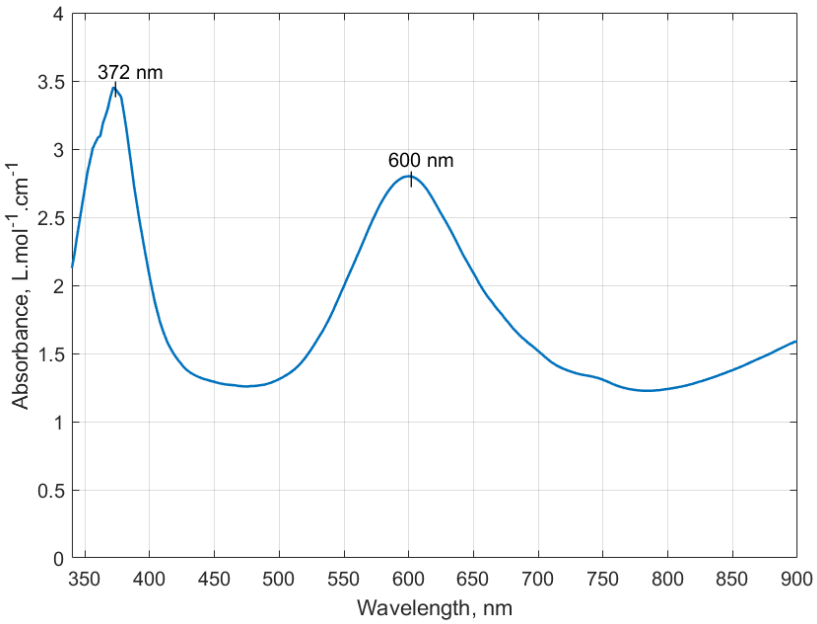

Figure 4.17. UV-Vis Spectrum for Ni-Ammonia solution prepared at pH=9.5.

4.2.1. Effect of Chelating Agents on Impregnating Solution

Chelation is a highly effective method for increasing the stability of metal cations in impregnating solutions. By adding chelating agents, the precipitation of metal ion hydroxides and hydrous oxides can be shifted to higher pH levels (Apak et al., 1999). This is crucial as it allows the metal precursor to remain in solution at a pH suitable for impregnation, ensuring its availability for the desired process.

One significant advantage of chelating agents is their ability to hinder the accumulation of metal ions during the impregnation step. This is due to the bulky structure of chelates, which prevents the metal ions from aggregating and promotes a higher level of dispersion. The use of chelating agents leads to a more uniform distribution of metal ions on the support surface.

An example of a common and well-known chelating agent is EDTA, which can form stable complexes with nickel in a 1:1 molar ratio. This means that each molecule of EDTA can bind to one nickel ion, forming a stable and well-controlled complex. This stability enhances the control and manipulation of nickel ions in impregnating solutions, thus improves the efficiency of the impregnation process further.

A mixture of 10.05 M NH_3 to 1.91405 M $Ni(NO_3)_2$ and 1.91405 M H_4EDTA was used to prepare Ni-EDTA (1:1 mole) impregnation solution. Mass balance equations for $Ni(NO_3)_2$, NH_3 and H_4EDTA in the impregnating solution are written as

$$\begin{aligned} c_{Ni(NO_3)_2} = {} & [Ni^{2+}] + [\mathrm{Ni}(EDTA)^{2-}] + [\mathrm{NiH}(EDTA)^{-}] + [\mathrm{NiH_2}(EDTA)] \\ & + [\mathrm{NiOH}(EDTA)^{3-}] + [\mathrm{Ni}(EDTA)(\mathrm{NH_3})^{2-}] + [\mathrm{Ni}(NH_3)^{2+}] \\ & + [\mathrm{Ni}(NH_3)_2^{2+}] + [\mathrm{Ni}(NH_3)_3^{2+}] + [\mathrm{Ni}(NH_3)_4^{2+}] \\ & + [\mathrm{Ni}(NH_3)_5^{2+}] + [\mathrm{Ni}(NH_3)_6^{2+}] + \frac{n_{Ni(OH)_2(s)}}{V_{sol}} \end{aligned} \quad (4.8)$$

$$\begin{aligned} c_{NH_3} = {} & [NH_3] + [NH_4^+] + [\mathrm{Ni}(NH_3)^+] + 2[\mathrm{Ni}(NH_3)_2^{2+}] \\ & + 3[\mathrm{Ni}(NH_3)_3^{2+}] + 4[\mathrm{Ni}(NH_3)_4^{2+}] + 5[\mathrm{Ni}(NH_3)_5^{2+}] \\ & + 6[\mathrm{Ni}(NH_3)_6^{2+}] + [\mathrm{Ni}(EDTA)(\mathrm{NH_3})^{2-}] \end{aligned} \quad (4.9)$$

$$\begin{aligned} c_{H_4EDTA} = {} & [EDTA^{4-}] + [\mathrm{H}EDTA^{3-}] + [\mathrm{H_2}EDTA^{2-}] + [\mathrm{H_3}EDTA^{-}] \\ & + [\mathrm{H_4}EDTA] + [\mathrm{Ni}(EDTA)^{2-}] + [\mathrm{NiH}(EDTA)^{-}] \\ & + [\mathrm{NiH_2}(EDTA)] + [\mathrm{NiOH}(EDTA)^{3-}] + [\mathrm{Ni}(EDTA)(\mathrm{NH_3})^{2-}] \end{aligned} \quad (4.10)$$

and solved for each species considering their equilibrium constants given in Table A.1, Table A.2, Table A.3, Table A.4, Table A.5 and Table A.6. The species and their corresponding concentrations, as predicted, are shown in Figure 4.18.

The expected complexes of Ni-EDTA remain negatively charged even under acidic conditions, which prevents the formation of $Ni(OH)_2$(s) formation, which is not predicted due to the high stability of Ni-EDTA complexes. However, since EDTA has limited solubility in water at low pH levels, the pH of the impregnating solution was adjusted to around 8 by using ammonia. At this pH, the predominant complex species is $[\mathrm{Ni(EDTA)(NH_3)}]^{2-}$. This adjustment ensures that the impregnating solution contains soluble Ni-EDTA complexes. The UV-Vis spectrum of $Ni(NO_3)_2$ showed a shift in the local maxima towards 584 nm, confirming the formation of Ni-EDTA complexes, as given in Figure 4.19. This shift provides experimental evidence for the presence of Ni-EDTA complexes in the impregnating solution (Laine and Matilainen, 2005).

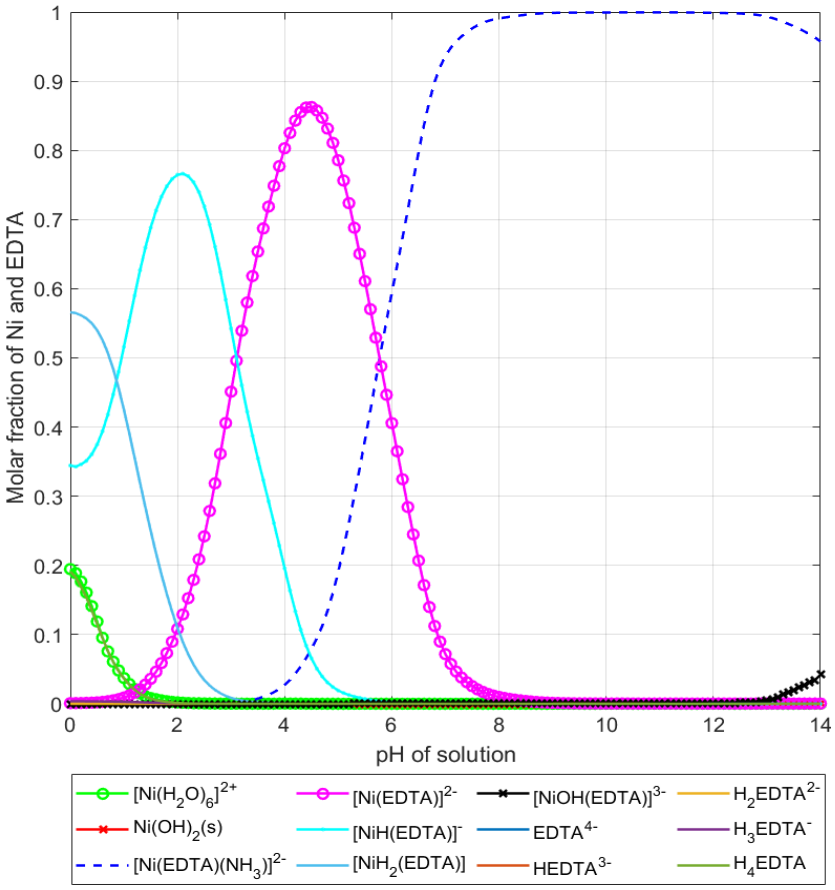

Figure 4.18. Thermodynamic predictions of Ni species in EDTA - Ammonia solution as a function of pH.

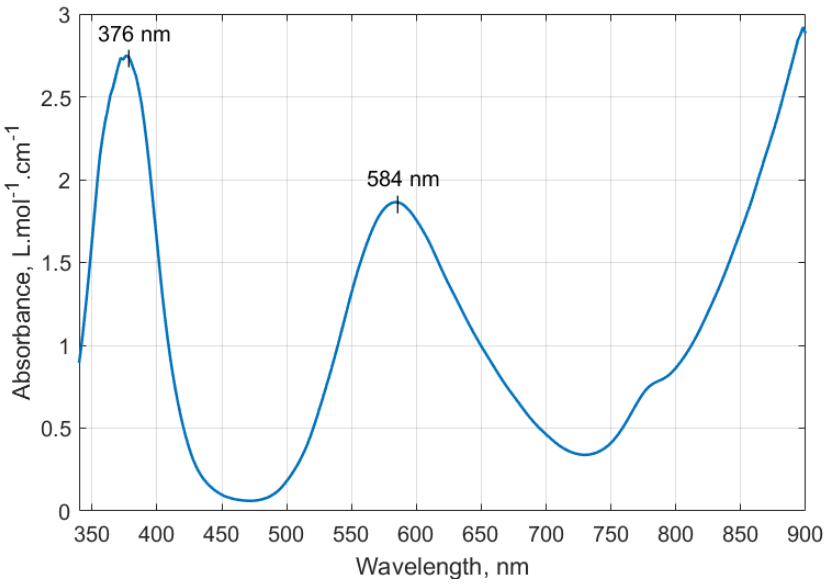

Figure 4.19. UV-Vis Spectra for Ni-EDTA solution prepared at pH=8.0.

Mass balance equations for Ni-NTA (1:1 mole) complexes in aqueous ammonia solution is written as

$$\begin{aligned} c_{Ni(NO_3)_2} &= [Ni^{2+}] + [\mathrm{Ni}(NTA)^-] + [\mathrm{Ni}(NTA)_2^{4-}] + [\mathrm{Ni}(NTA)(NH_3)^-] \\ &\quad + [\mathrm{Ni}(NTA)(NH_3)_2^-] + [\mathrm{Ni}(NH_3)^{2+}] + [\mathrm{Ni}(NH_3)_2^{2+}] \\ &\quad + [\mathrm{Ni}(NH_3)_3^{2+}] + [\mathrm{Ni}(NH_3)_4^{2+}] + [\mathrm{Ni}(NH_3)_5^{2+}] \\ &\quad + [\mathrm{Ni}(NH_3)_6^{2+}] + \frac{n_{Ni(OH)_2(s)}}{V_{sol}} \end{aligned} \quad (4.11)$$

$$\begin{aligned} c_{NH_3} &= [NH_3] + [NH_4^+] + [\mathrm{Ni}(NH_3)^+] + 2[\mathrm{Ni}(NH_3)_2^{2+}] \\ &\quad + 3[\mathrm{Ni}(NH_3)_3^{2+}] + 4[\mathrm{Ni}(NH_3)_4^{2+}] + 5[\mathrm{Ni}(NH_3)_5^{2+}] \\ &\quad + 6[\mathrm{Ni}(NH_3)_6^{2+}] + [\mathrm{Ni}(NTA)(NH_3)^-] + 2[\mathrm{Ni}(NTA)(NH_3)_2^-] \end{aligned} \quad (4.12)$$

$$\begin{aligned} c_{H_3NTA} &= [NTA^{3-}] + [HNTA^{2-}] + [H_2NTA^-] + [H_3NTA] \\ &\quad + [H_4NTA^+] + [\mathrm{Ni}(NTA)^-] + 2[\mathrm{Ni}(NTA)_2^{4-}] \\ &\quad + [\mathrm{Ni}(NTA)(NH_3)^-] + [\mathrm{Ni}(NTA)(NH_3)_2^-] \end{aligned} \quad (4.13)$$

for the solution containing 1.91405 M $Ni(NO_3)_2$ and 1.91405 M NTA (1:1 metal to chelate molar ratio) in 10.05 M NH_3 aqueous solution. Final concentrations were determined by performing equilibrium calculations utilizing the equilibrium constants provided in Table A.1, Table A.2, Table A.3, Table A.4, Table A.7 and Table A.8 and illustrated in Figure 4.20, considering varying solution pH.

The thermodynamic calculations reveal that the precipitation of $Ni(OH)_2(s)$ is hindered until pH values exceed 12, owing to the complexation of Ni with NTA. Additionally, the formation of negatively charged complexes occurs even under acidic conditions, where the support surface is positively charged, similar to the formation of Ni-EDTA complexes. These findings justify the selection of NTA as the complexing agent for the preparation of the impregnating solution.

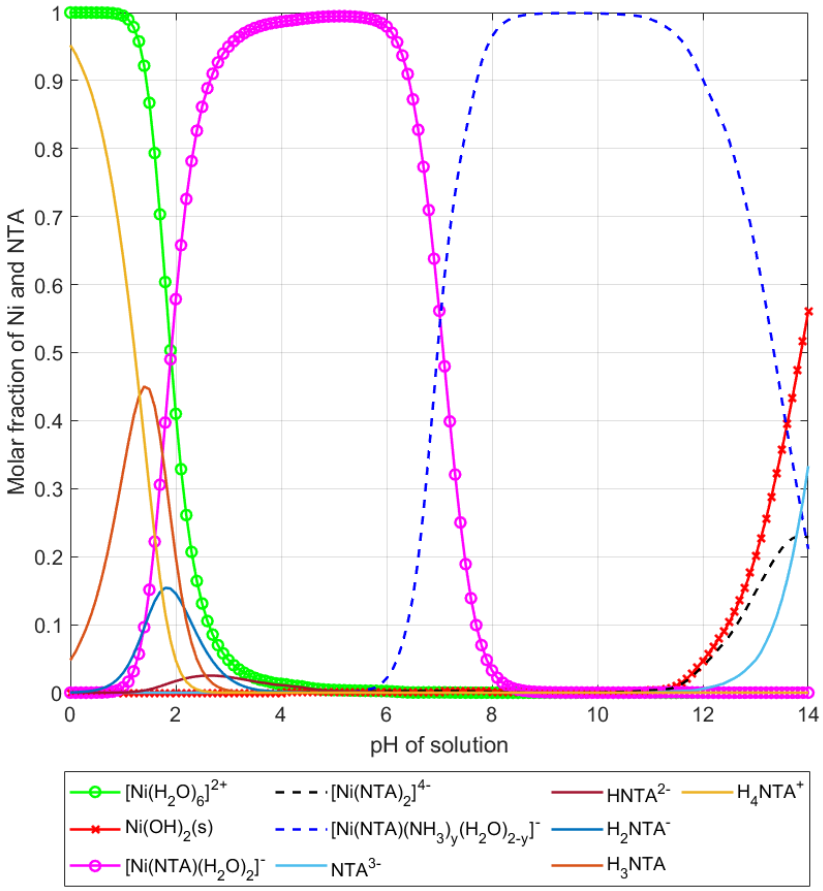

Figure 4.20. Thermodynamic predictions of Ni species in NTA - Ammonia solution as a function of pH.

The increase in solution pH facilitated the deprotonation of the carboxylic groups in NTA, resulting in generation of NTA ligands capable of interacting with nickel. In order to promote the formation of $[Ni(NTA)(H_2O)_2]^-$ complex, pH of the impregnating solution was adjusted to 6.0. This adjustment aimed to favor the predominant presence of the $[Ni(NTA)(H_2O)_2]^-$ species. Formation of new complexes involving NTA was confirmed through the UV-Vis spectrum provided in Figure 4.21 (Medici and Prins, 1996)

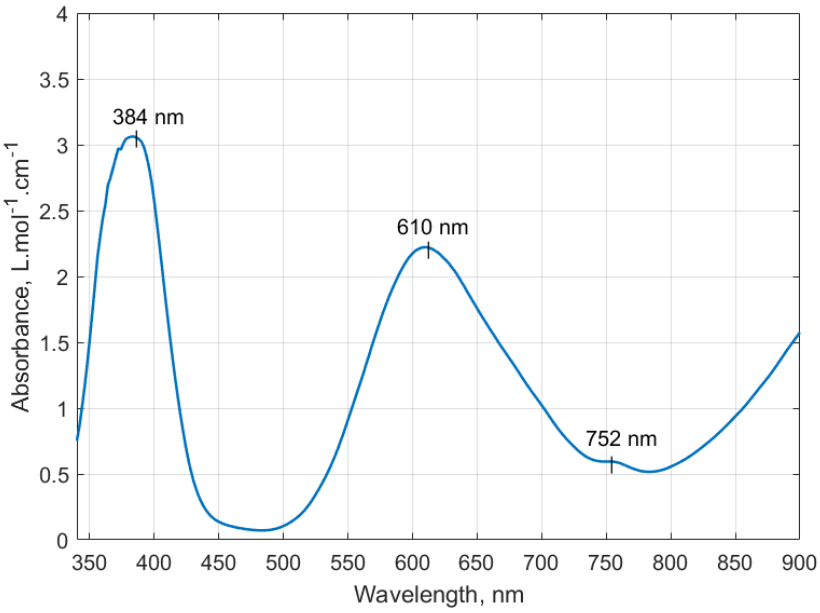

Figure 4.21. UV-Vis Spectra for Ni-NTA solution prepared at pH=6.0.

Mass balance equations around the impregnating solution of Ni-CA (1:1 mole) complexes in aqueous NH_3 solution can be written as

$$\begin{aligned} c_{Ni(NO_3)_2} = {} & [Ni^{2+}] + [\mathrm{Ni}(Cit)^{-}] + [\mathrm{Ni}(Cit)_2^{4-}] + [\mathrm{Ni}(HCit)] \\ & + [\mathrm{Ni}(H_2Cit)^{+}] + [\mathrm{Ni}(HCit)(Cit)^{3-}] + 2[\mathrm{Ni}_2(\mathrm{H}_{-1}\mathrm{Cit})_2^{4-}] \\ & + [\mathrm{Ni}(NH_3)^{2+}] + [\mathrm{Ni}(NH_3)_3^{2+}] + [\mathrm{Ni}(NH_3)_4^{2+}] \\ & + [\mathrm{Ni}(NH_3)_5^{2+}] + [\mathrm{Ni}(NH_3)_6^{2+}] + \frac{n_{Ni(OH)_2(s)}}{V_{sol}} \end{aligned} \quad (4.14)$$

$$\begin{aligned} c_{NH_3} = {} & [NH_3] + [NH_4^{+}] + [\mathrm{Ni}(NH_3)^{+}] + 2[\mathrm{Ni}(NH_3)_2^{2+}] \\ & + 3[\mathrm{Ni}(NH_3)_3^{2+}] + 4[\mathrm{Ni}(NH_3)_4^{2+}] + 5[\mathrm{Ni}(NH_3)_5^{2+}] \\ & + 6[\mathrm{Ni}(NH_3)_6^{2+}] \end{aligned} \quad (4.15)$$

$$\begin{aligned} c_{H_3Cit} = {} & [Cit^{3-}] + [\mathrm{H}_3Cit] + [\mathrm{H}_2Cit^{-}] + [\mathrm{HCit}^{2-}] + [\mathrm{H}_{-1}Cit^{4-}] \\ & + [\mathrm{Ni}(Cit)^{-}] + 2[\mathrm{Ni}(Cit)_2^{4-}] + [\mathrm{Ni}(HCit)] + [\mathrm{Ni}(H_2Cit)^{+}] \\ & + 2[\mathrm{Ni}(HCit)(Cit)^{3-}] + 2[\mathrm{Ni}_2(\mathrm{H}_{-1}\mathrm{Cit})_2^{4-}] \end{aligned} \quad (4.16)$$

where H_3Cit represents citric acid. Equilibrium calculations were performed utilizing the equilibrium constants provided in Table A.1, Table A.2, Table A.3, Table A.4, Table A.9 and Table A.10.

The incorporation of citric acid effectively prevented the formation of nickel hydroxide up to high pH levels (up to 10) in impregnating solutions containing 1.91405 M CA, 1.91405 M $Ni(NO_3)_2$, and 10.05 M NH_3, as demonstrated in Figure 4.22, which showcases the variation in species concentrations with changing solution pH. The persistence of $[Ni(H_2O)_6]^{2+}$ ions up to pH 6 indicates the thermodynamically unfavorable dissociation of citric acid. Consequently, the pH of the impregnation solution was adjusted to a range of 6.5 to 7 in order to facilitate the formation of negatively charged $[Ni(Cit)]^-$ and $[Ni(Cit)_2]^{4-}$ species.

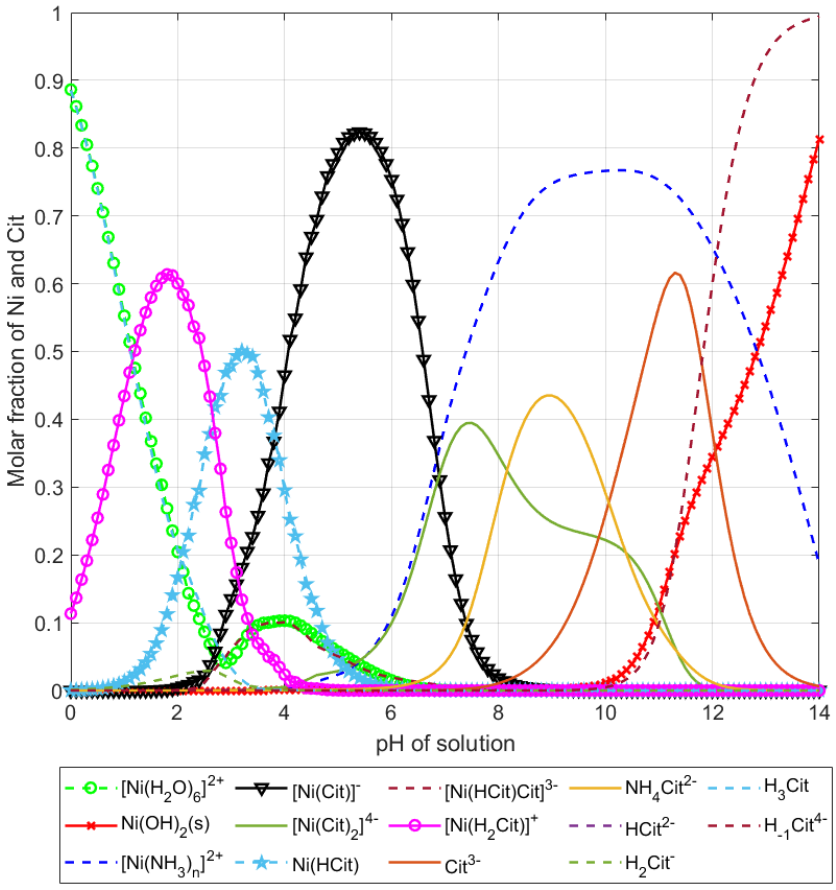

Figure 4.22. Thermodynamic predictions of Ni species in Citric Acid - Ammonia solution as a function of pH.

The formation of Ni-CA complexes was confirmed through the UV-Vis spectrum shown in Figure 4.23 (Suárez-Toriello et al., 2015). It is worth noting that due to the presence of excess ammonium ions in the solution, the formation of $[Ni(NH_3)_n(H_2O)_{6-n}]^{2+}$ complexes was also predicted within this pH range.

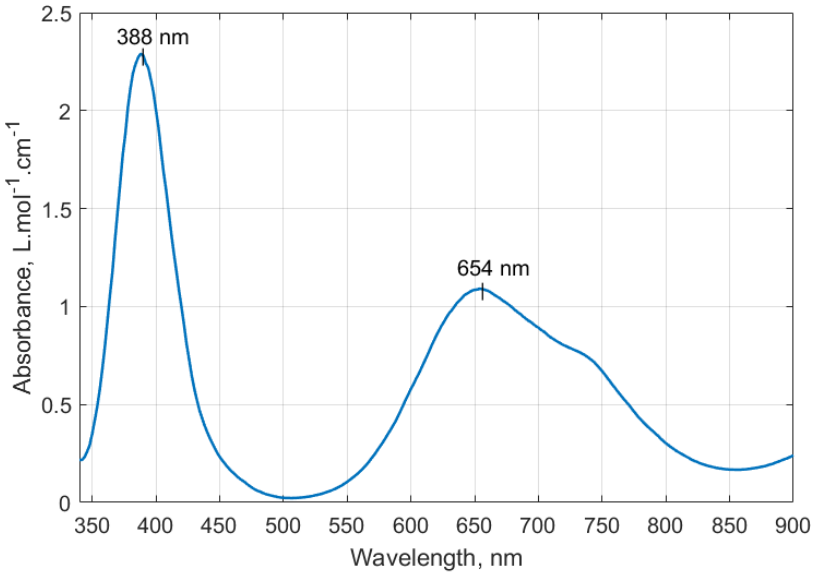

Figure 4.23. UV-Vis Spectra for Ni-Citric acid solution prepared at pH=6.7.

4.3. Analysis of Impregnation Step

In addition to chemical nature of impregnating solution, several physical parameters during the impregnation process can significantly affect the dispersion level. These parameters include the vacuum level, the temperature of the medium, and the method of mixing.

In the synthesis of all samples, the impregnation process was carried out under the same vacuum level, and an ultrasonic bath was used for effective mixing. However, it should be noted that during the use of an ultrasonic bath energy is transferred to water inside the bath tank and, as a consequence, to the thick “support-precursor solution” slurry formed in the vacuum Erlenmeyer connected to the pump, leading to a gradual increase in temperature in both mediums. The variation of water temperature over time was carefully examined, revealing a linear increase with sinusoidal fluctuations, as shown in Figure 4.24. It is important to highlight that a consistent initial temperature was maintained during the synthesis of all samples, and similar temperature increment patterns were observed across the samples.

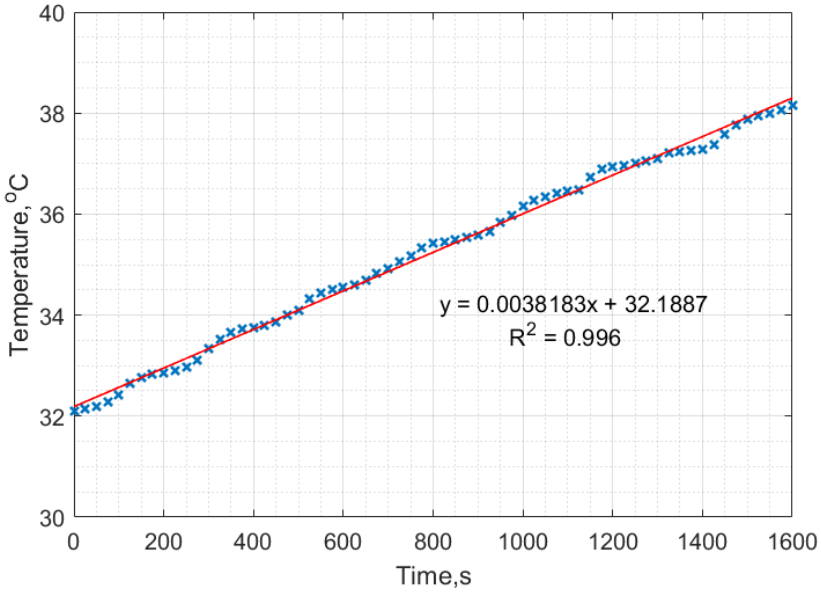

Figure 4.24. Temperature rise in ultrasonic bath during impregnation process.

To investigate the adsorption behavior of nickel cation from water onto selected support surfaces, samples synthesized with $Ni(NO_3)_2.6H_2O$ precursor were analyzed by Raman spectroscopy after overnight drying at 110 °C, and the corresponding Raman spectra are presented in Figure 4.25.

All three samples display prominent nitrate modes, with the most intense peak observed at approximately 1050 cm^{-1} and weak bands observed around 720 cm^{-1} corresponding to stretching mode of free nitrate. Absence of the Ni-N stretching mode around 400 cm^{-1} can be attributed to the formation of new nickel-support interactions after the breaking of Ni-N bonds. For the γ- and δ-Al_2O_3 samples, bands at ~1310 cm^{-1} and ~1630 cm^{-1} indicate the presence of $Al(OH)_3$ and O-H bend of free H_2O, respectively. However, in the case of La-doped Al_2O_3 that underwent calcination at 1000°C for 4 hours after lanthanum impregnation, the $Al(OH)_3$ and free water bands are absent. This absence is due to the dehydration of $Al(OH)_3$, as indicated by the reaction given in Equation 4.17 (Arnold, 2022).

$$2Al(OH)_3(s) \rightarrow Al_2O_3(s) + 3H_2O(g) \qquad \Delta H_{298\,K} = +154.5\ kJ\ mol^{-1} \qquad (4.17)$$

The presence of a Raman band at approximately 550 cm^{-1} suggests the existence of Ni-O bonds on the δ-Al_2O_3 support surface, indicating the adsorption of nickel onto the support surface. However, due to the characteristic behavior of low oxidation state metals, nickel tends to form a surface spinel on the alumina support. This can lead to the absorption and trapping of nickel in the subsurface layers. As a result, the band at 550 cm^{-1} which corresponds to Ni^{2+} adsorption on surface OH^- groups, exhibits a low intensity and weak visibility (Wash et al., 1986).

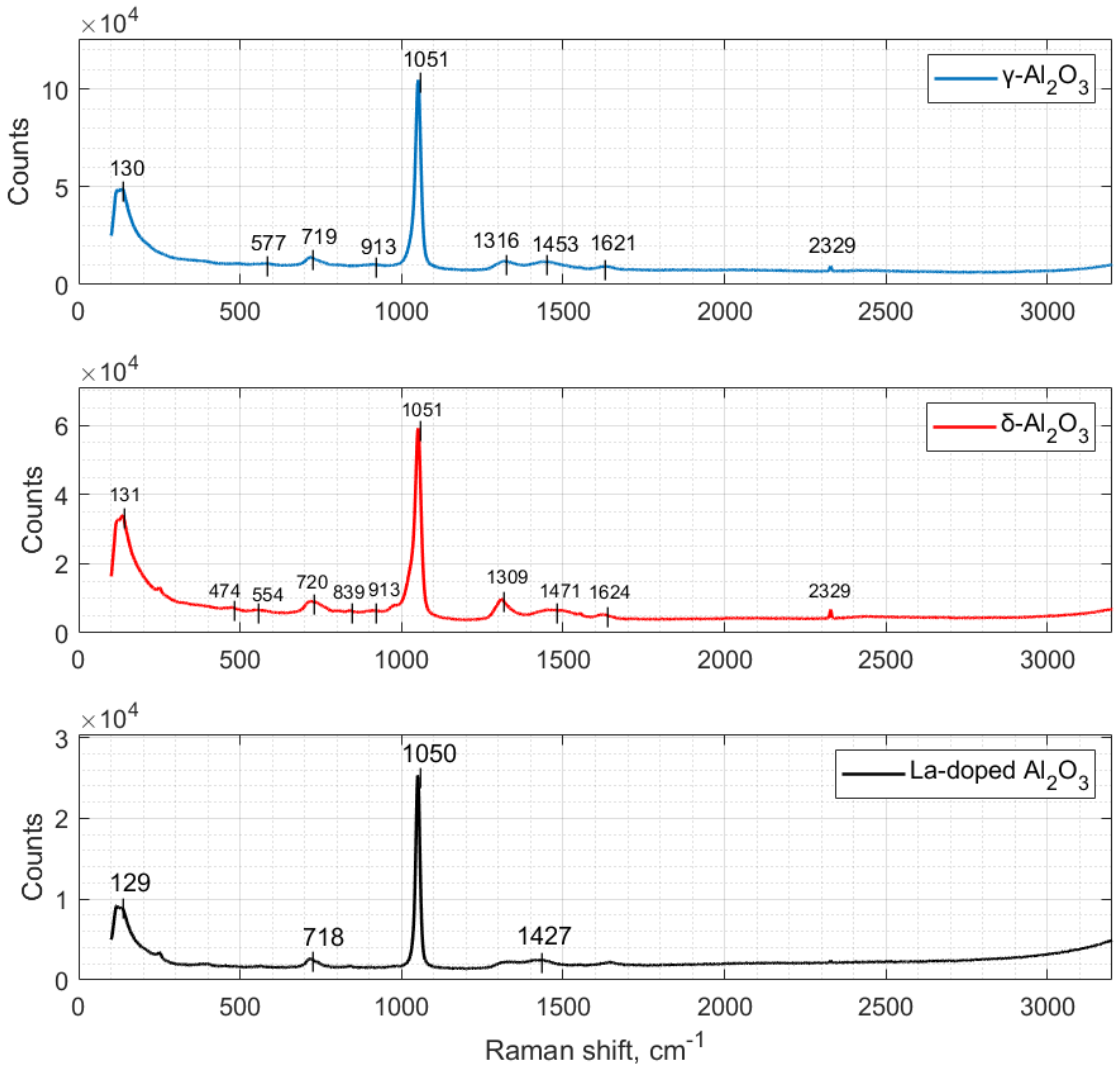

Figure 4.25. Raman spectra of $Ni(NO_3)_2$ impregnated Al_2O_3 supports after overnight drying at 110°C .

4.4. Dispersion Measurements

In this parametric study aimed at enhancing the level of metal dispersion on the reference, 10 wt.% Ni-loaded catalysts, key parameters identified were the impacts of support modification, choice of impregnation solution, and the calcination temperature. Table 4.5 displays the levels of metal dispersion obtained in the conducted study. In order to provide a clearer visualization of the impact of different parameters on dispersion, a three-dimensional column graph was prepared and presented in Figure 4.26.

Table 4.5. Ni dispersion results comparison table for all sample variants.

Impregnating Solution	**Calc. Temp (°C)**	**Gamma Alumina (γ-Al_2O_3)**		**920°C Precalcined Support (δ-Al_2O_3)**		**920°C Precalc. + 1% La Doped (calc.at 1000°C)**	
		pH	**% Dispersion**	**pH**	**% Dispersion**	**pH**	**% Dispersion**
$Ni(NO_3)_2$ Solution	**500**	3.51	5.2492	3.47	6.3426	3.57	6.5477
	700	3.52	3.1094	3.48	4.9317	3.50	4.6177
	900	3.48	4.0714	3.46	3.7846	3.52	2.9109
$Ni(NO_3)_2$ Solution with pH regulation (Below PZC)	**500**	0.86	5.4682	0.83	6.5554	0.86	6.5678
	700	0.86	5.1517	0.83	3.9632	0.86	3.5900
	900	0.85	3.9605	0.83	2.9880	0.87	3.4519
$Ni(NO_3)_2$ Solution with pH regulation (Above PZC)	**500**	9.77	4.6393	9.87	5.6147	9.82	6.0890
	700	9.57	4.7539	9.82	4.3152	9.85	4.0048
	900	9.83	3.8552	9.68	4.1144	9.87	2.5976
$Ni(NO_3)_2$ + EDTA (1:1 mol) Solution	**500**	8.02	5.1183	7.98	5.7077	8.20	6.1106
	700	8.50	3.0632	8.03	4.3473	8.22	4.054
	900	7.97	3.7533	8.42	4.1088	8.16	3.6448

Table 4.5. Ni dispersion results comparison table for all sample variants. (cont.)

Impregnating Solution	Calc. Temp (°C)	Gamma Alumina (γ-Al_2O_3)		920°C Precalcined Support (δ-Al_2O_3)		920°C Precalc. + 1% La Doped (calc.at 1000°C)	
		pH	% Dispersion	pH	% Dispersion	pH	% Dispersion
$Ni(NO_3)_2$ + NTA (1:1 mol) Solution	**500**	6.22	6.4948	6.05	7.5593	6.12	8.0191
	700	6.2	5.0428	6.12	5.3180	6.13	6.3629
	900	6.02	3.0042	8.26	3.8667	6.05	3.2373
$Ni(NO_3)_2$ + Citric Acid (1:1 mol) Solution	**500**	6.77	6.5373	6.73	7.9522	6.76	9.2624
	700	6.75	5.0861	6.65	5.0858	6.73	5.7103
	900	6.72	3.6450	6.62	3.3583	6.77	2.5622

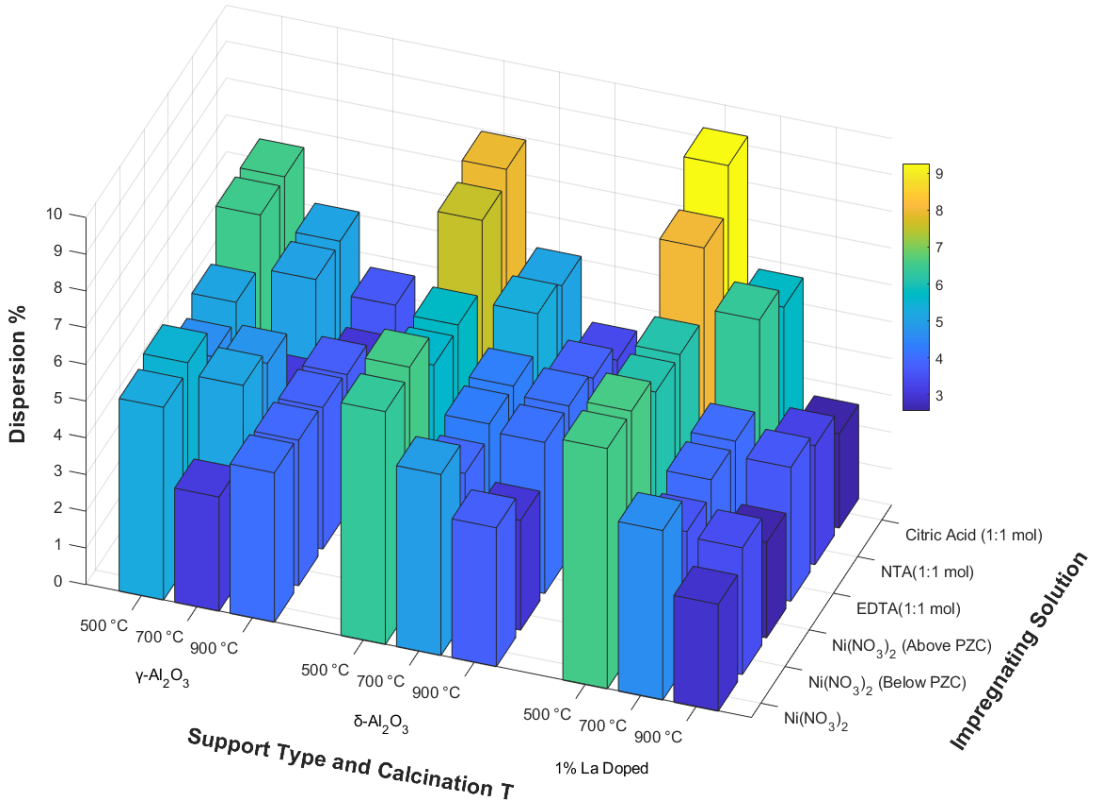

Figure 4.26. Comparative analysis of dispersion characteristics across all sample variants.

By assuming a hemispherical shape for the nickel (Ni) particles, average Ni metal particle size, L, can be computed through

$$L(nm) = \frac{6}{D}\left(\frac{\left(58.71\ \frac{g}{mol}\right)}{\left(8.902\frac{g}{cm^3}\right)(6.022\times10^{23}\ mol^{-1})}\times\frac{10^{21}\ nm^3}{cm^3}}{0.0649\ nm^2}\right) \tag{4.18}$$

which reflects the proportionality of dispersion, D, with metal particle size. Furthermore, in the field of supported metal catalysts, metallic surface area is a fundamental concept that is directly influenced by dispersion and directly related with Ni metallic surface area in samples, which can be written as

$$S_M\left(\frac{m^2}{g\ of\ Ni}\right) = (6.49\times10^{-20}\ m^2)\left(\frac{6.022\times10^{23}\ mol^{-1}}{\left(58.71\ \frac{g}{mol}\right)}\right)\times D. \tag{4.19}$$

Calculated results for Ni metal particle size and surface area are presented in Table 4.6 and the corresponding graphical representation for Ni metal particle size can be found in Figure 4.27.

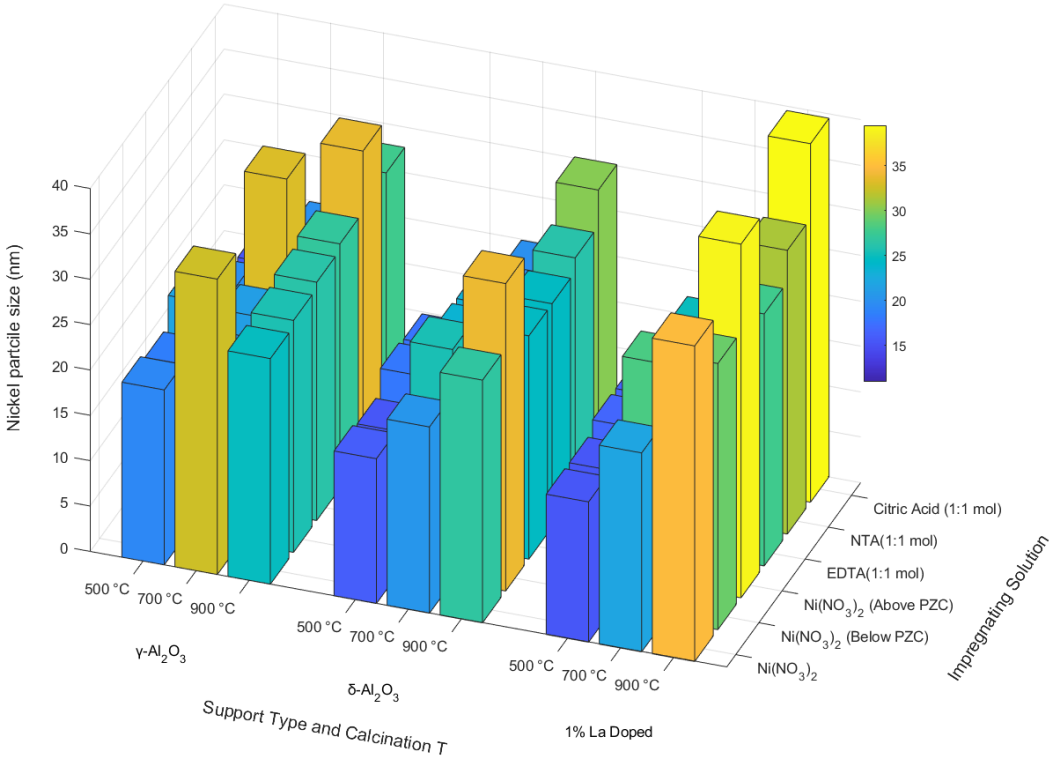

Figure 4.27. Nickel particle size on catalyst samples.

Table 4.6. Metallic area and crystallite size of Nickel on all samples.

Impregnating Solution	Calc. Temp (°C)	Gamma Alumina (γ-Al_2O_3)		920°C Precalcined Support (δ-Al_2O_3)		920°C Precalc. + 1% La Doped (calc.at 1000°C)	
		Metallic area (m^2/g metal)	Crystallite Size (nm)	Metallic area (m^2/g metal)	Crystallite Size (nm)	Metallic area (m^2/g metal)	Crystallite Size (nm)
$Ni(NO_3)_2$ Solution	**500**	34.94	19.29	42.22	15.96	43.59	15.46
	700	20.70	32.56	32.83	20.53	30.74	21.93
	900	27.10	24.87	25.19	26.75	19.38	34.78
$Ni(NO_3)_2$ Solution with pH regulation (Below PZC)	**500**	36.40	18.52	43.64	15.45	43.72	15.42
	700	34.29	19.65	26.38	25.55	23.90	28.20
	900	26.36	25.56	19.89	33.89	22.98	29.33
$Ni(NO_3)_2$ Solution with pH regulation (Above PZC)	**500**	30.88	21.82	37.38	18.03	40.53	16.63
	700	31.65	21.30	28.73	23.46	26.66	25.28
	900	25.66	26.26	27.39	24.61	17.29	38.98
$Ni(NO_3)_2$ + EDTA (1:1 mol) Solution	**500**	34.07	19.78	38.00	17.74	40.68	16.57
	700	20.39	33.05	28.94	23.29	26.99	24.98
	900	24.99	26.98	27.35	24.64	24.26	27.78
$Ni(NO_3)_2$ + NTA (1:1 mol) Solution	**500**	43.24	15.59	50.32	13.39	53.38	12.63
	700	33.57	20.08	35.40	19.04	42.36	15.91
	900	20.00	33.70	25.74	26.18	21.55	31.28
$Ni(NO_3)_2$ + Citric Acid (1:1 mol) Solution	**500**	43.52	15.49	52.94	12.73	61.66	10.93
	700	33.86	19.91	33.86	19.91	38.01	17.73
	900	24.26	27.78	22.36	30.15	17.06	39.52

In this context, a high level of dispersion indicates a well-dispersed and separately distributed metal particles. This leads to an increased metallic surface area, which plays a critical role in catalysis as it determines the amount of available active sites exposed to reactants during reaction which facilitate adsorption and surface reactions, and at the same time, improve mass transfer through supporting homogeneity of active site distribution and enhance the stability of the catalyst. Therefore, optimizing the metallic surface area becomes essential for enhancing catalytic activity, selectivity, and overall performance in a wide range of industrial and environmental applications.

4.4.1. Effect of Calcination Temperature

Calcination temperature has a significant impact on the metal dispersion levels of the catalyst. Generally, higher levels of dispersion are achieved when samples are calcined at lower temperatures. Conversely, a decrease in dispersion is observed as the calcination temperature increases. This decrease in the dispersion level of nickel can be attributed to the increased mobility of nickel oxides formed on the surface of catalyst, leading to a more pronounced particle migration and Ostwald ripening effect (Hansen et al., 2013).

Metals with lower valency and smaller ionic radii, such as nickel, have a propensity to incorporate into the spinel structure of the alumina support at elevated temperatures. Nickel on an Al_2O_3 support can exist in either metallic Ni form or in its oxide form, NiO, and can also be incorporated into the spinel structure. The formation of nickel aluminate spinel ($NiAl_2O_4$) is indicated by the transition from the green color associated with NiO to a distinct pale blue color. This color change serves as a visual confirmation of $NiAl_2O_4$, specifically observed in samples subjected to calcination temperatures of 700°C and 900°C. Furthermore, Figure 4.28 provides additional substantiation through XRD analysis, confirming the presence of $NiAl_2O_4$.

Studies conducted on Ni/Al_2O_3 catalysts have provided compelling evidence that Ni clusters derived from the reduction of the $NiAl_2O_4$ spinel structure exhibit enhanced dispersion and increased stability (Kwon et al., 2022). These improvements were attributed to the strengthened interactions between the Ni clusters and the alumina support. Furthermore, the reduction conditions employed in this study, involving one-hour treatment

at 800°C under pure H_2 flow, are well-suited for reducing $NiAl_2O_4$ to metallic Ni (Iglesias-Vázquez et al., 2022). However, it is important to note that complete reduction of all $NiAl_2O_4$ species was not achieved under these conditions, as confirmed by the XRD results.

The formation of $NiAl_2O_4$ spinels is the result of a chemical reaction occurring between two solid phases. The rate of this reaction is governed by two main factors: the $NiAl_2O_4$ formation reaction itself and the diffusion rate of Ni metal and NiO molecule into the alumina support. As the reaction progresses, the nucleation of $NiAl_2O_4$ spinels introduces a kinetic barrier effect. Consequently, the rate of the reaction is primarily controlled by diffusion processes, particularly at lower temperatures. This diffusion control mechanism plays a pivotal role in determining the overall reaction kinetics in this system (Gonçalves et al., 2018).

XRD analyses presented in Figure 4.28 reveal noticeable shifts in certain diffraction peaks attributed to the $NiAl_2O_4$ spinel phase. These peak shifts can be ascribed to the formation of inverse $Al(NiAl)O_4$ and intermediate $NiO.Al_2O_3$ spinel phases (Azurdia et al., 2006). Moreover, the samples subjected to a calcination temperature of 900°C display increased distortion in the γ-Al_2O_3 peaks, accompanied by the detection of δ- Al_2O_3 characterized by broad and low-intensity peaks.

The particle sizes of nickel (Ni) and nickel aluminate spinel ($NiAl_2O_4$) were determined through XRD analysis, focusing on the (111) and (311) crystal planes, respectively. Size calculations were performed using the Scherrer equation (Equation 4.20), employing the X-ray wavelength of 1.5406 Å corresponding to copper K-α radiation. The K shape constant was kept fixed at 0.89 for all measurements, ensuring consistency. The resulting nanoparticle sizes for Ni and $NiAl_2O_4$ were obtained and are presented comprehensively in Table 4.7 for reference and analysis.

$$L = \frac{K\lambda}{\beta . cos\theta} \tag{4.20}$$

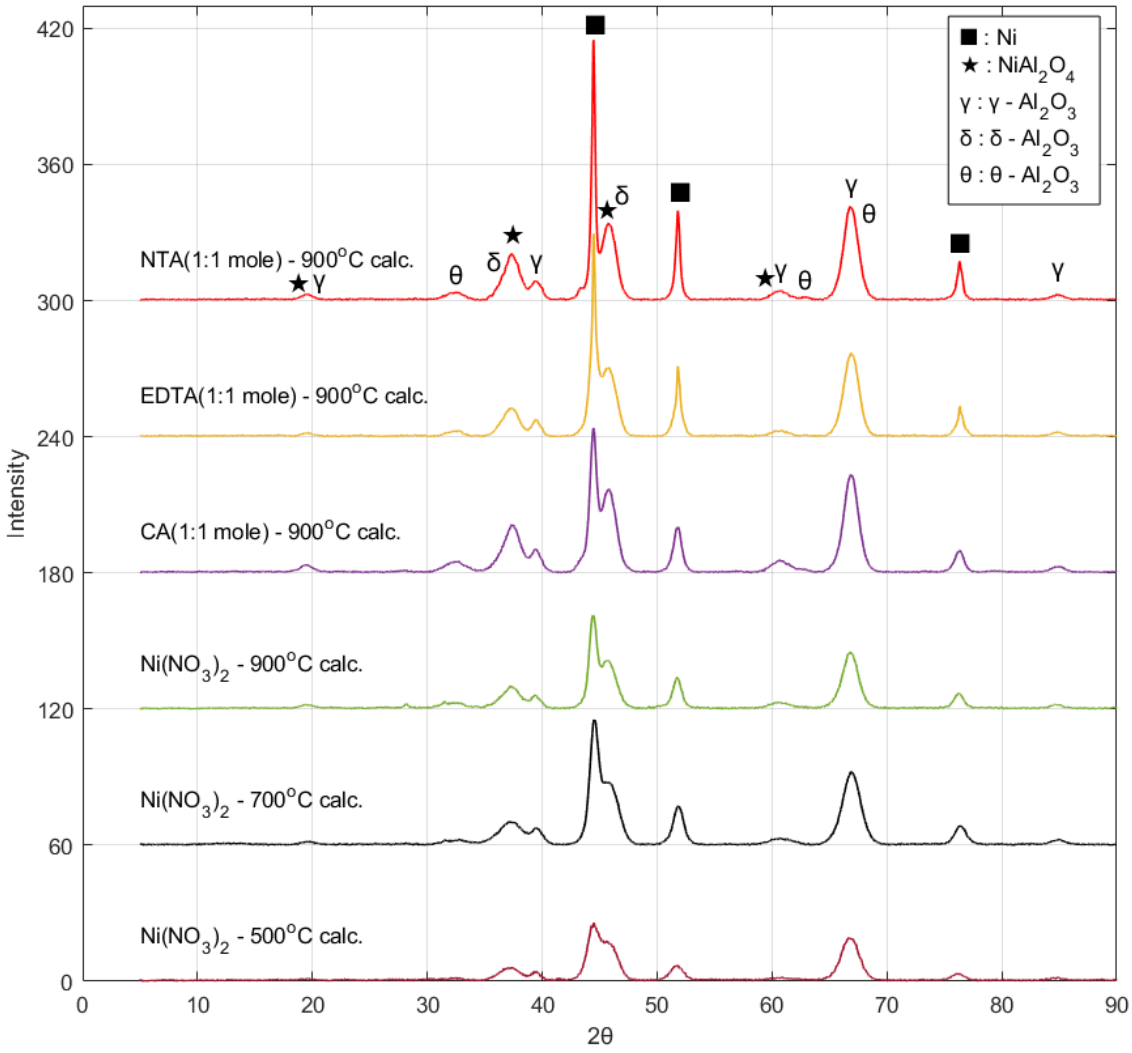

Figure 4.28. XRD results of selected reduced γ- Al_2O_3 samples.

Table 4.7. Nanoparticle size of Ni and $NiAl_2O_4$ according to Scherrer formula.

Sample	**Ni Particle size (nm)**	**$NiAl_2O_4$ Particle size (nm)**
γ-Al_2O_3 – $Ni(NO_3)_2$ - 700°C calc.	12.59	16.87
γ-Al_2O_3 – $Ni(NO_3)_2$ - 900°C calc.	13.40	8.27
γ-Al_2O_3 – CA (1:1 mole) - 900°C calc.	17.28	9.66
γ-Al_2O_3 – EDTA (1:1 mole) - 900°C calc.	27.64	9.89
γ-Al_2O_3 – NTA (1:1 mole) - 900°C calc.	20.75	7.66

Table 4.7 provides compelling evidence that increasing the calcination temperature leads to a corresponding increase in the particle size of nickel metal, while conversely resulting in a decrease in the particle size of $NiAl_2O_4$. As the calcination temperature rises, it is expected that the population of $NiAl_2O_4$ spinel species will increase in samples calcined at 900°C compared to those at 700°C. The results calculated through the use of Scherrer equation on pronounced peaks of Ni and $NiAl_2O_4$ strongly suggest that:

(i) The distribution of Ni clusters decreases, indicated by the increase in particle size, in response to increase in calcination temperature while, by showing a contrast trend, $NiAl_2O_4$ particle size decreases.
(ii) The thermodynamics/energetics of the calcination process favor the formation of Ni clusters, i.e., addition of Ni surface species to the Ni-nucleation centers forming larger size Ni clusters, while addition of Ni surface species in the enlargement of $NiAl_2O_4$ clusters with the increase in calcination temperature.
(iii) One should not misinterpret the decrease in $NiAl_2O_4$ particle size as an indication of increase in "dispersion" considering the strong possibility that the absolute amount of Ni species forming $NiAl_2O_4$ clusters may be lowered due to point (ii).

4.4.2. Effect of Support Modification

Modifications made on the support material can induce changes on the surface chemistry of the support, which can subsequently influence the interactions between the nickel metal and the support surface.

The thermal treatments applied to the alumina support induced phase transitions, leading to an increase in thermal stability and affecting the support's acidity, as demonstrated in Table 4.5. The samples were subjected to rapid thermal ramping by placing them directly in a pre-heated muffle furnace, which resulted in an increased number of surface defects and facilitated the formation of acidic sites. The higher density of acid sites strengthens interactions between nickel and the alumina support, enabling greater dispersion by preventing the migration of nickel particles during calcination. The effect of acidic sites was particularly noticeable in samples calcined at low temperatures (500°C), as demonstrated in dispersion data presented in Table 4.5 and Figure 4.26.

However, this effect was not directly observable on samples calcined at high temperatures (700°C and 900°C) due to the formation of the $NiAl_2O_4$ spinel structure.

Figure 4.29. Schematic representation of the effect of thermal treatment on nickel dispersion.

In contrast to γ-alumina, the crystalline structure of δ- and θ-phases could impede the entrapment of Ni ions in their subsurface layers, making them difficult to reduce. This observation may also explain the absence of the peak at 550 cm^{-1} in the Raman spectrum of γ-alumina, indicating the presence of Ni-O bonds on the support surface.

The XRD results provided in Figure 4.30 illustrate the X-ray diffraction patterns obtained from catalyst samples prepared using the same type of impregnating solution containing Ni – CA complexes. However, these samples were supported on different materials, namely γ-Al_2O_3 and 1% La-doped Al_2O_3. After undergoing a calcination process at 900°C for 4 hours, the samples were subsequently subjected to a reduction process. The XRD results obtained after this calcination and reduction process are presented in Figure 4.30.

The XRD results indicate the formation of $LaAlO_3$ in the 1% La-doped alumina support. After the La-doped support sample was calcined at 1000°C following lanthanum addition, the BET surface area and PSD of support material (given in Table 4.1 and Figure 4.2) did not show significant differences compared to the values obtained after precalcination at 920°C. This suggests that the presence of lanthanum oxide suppresses the sintering of the support by facilitating the formation of $LaAlO_3$ on the surface.

The particle sizes of nickel (Ni) and nickel aluminate spinel ($NiAl_2O_4$) were determined using X-ray diffraction (XRD) analysis. The Scherrer equation was applied,

taking into account the crystal planes (111) for nickel and (311) for nickel aluminate spinel. The obtained results for particle sizes are presented in Table 4.8.

Table 4.8. Particle sizes of Ni and $NiAl_2O_4$ according to Scherrer formula for selected reduced catalysts.

Sample	Ni Particle size (nm)	$NiAl_2O_4$ Particle size (nm)
γ-Al_2O_3 – $Ni(NO_3)_2$ - 900°C calc.	17.28	9.66
1% La-doped-Al_2O_3 – CA - 900°C calc.	15.98	10.66

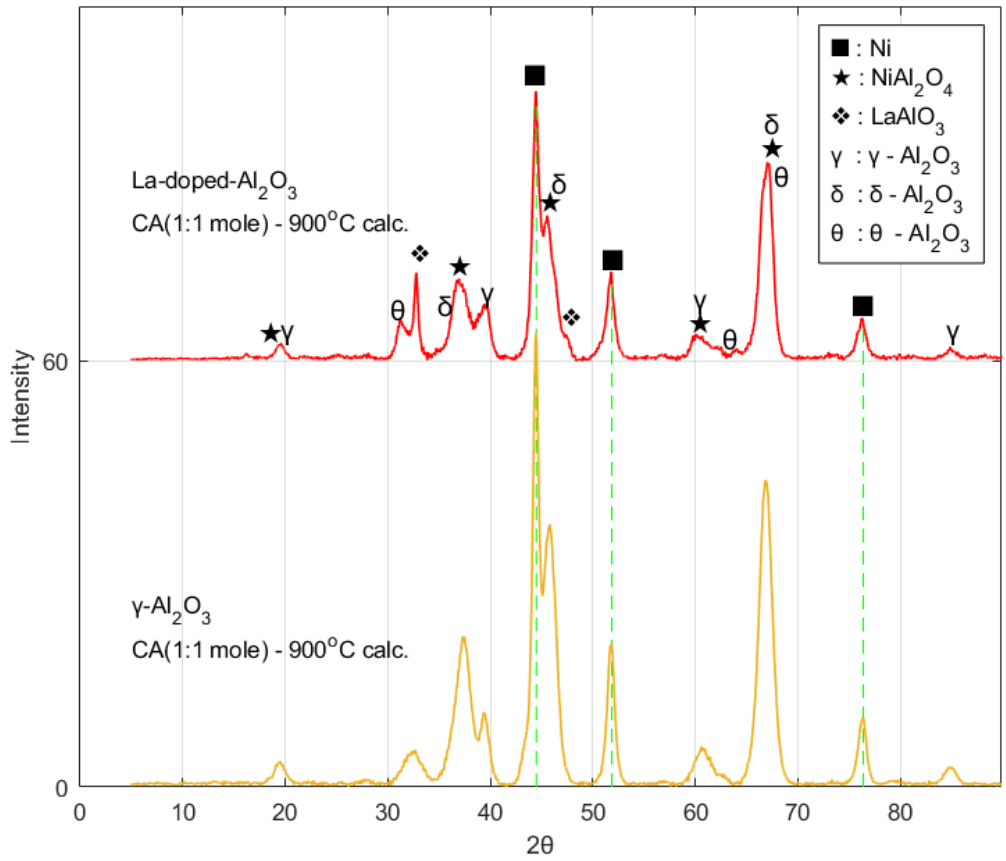

Figure 4.30. XRD results of selected reduced catalyst samples prepared on γ-Al_2O_3 and 1%La-Doped Al_2O_3.

The Brunauer-Emmett-Teller (BET) surface areas of the support materials and catalysts are provided in Table 4.9 for comparative evaluation. Further, Pore Size

Distribution (PSD) data for the catalysts and their corresponding supports are represented in Figure 4.31.

Table 4.9. BET Surface areas of selected reduced catalysts and their support materials.

Catalyst Sample	**Support Surface Area (m^2/g)**	**Catalyst Surface Area (m^2/g)**
γ-Al_2O_3 – $Ni(NO_3)_2$ - 900°C calc.	220.51	149.50
1% La-doped-Al_2O_3 – CA - 900°C calc.	114.98	98.63

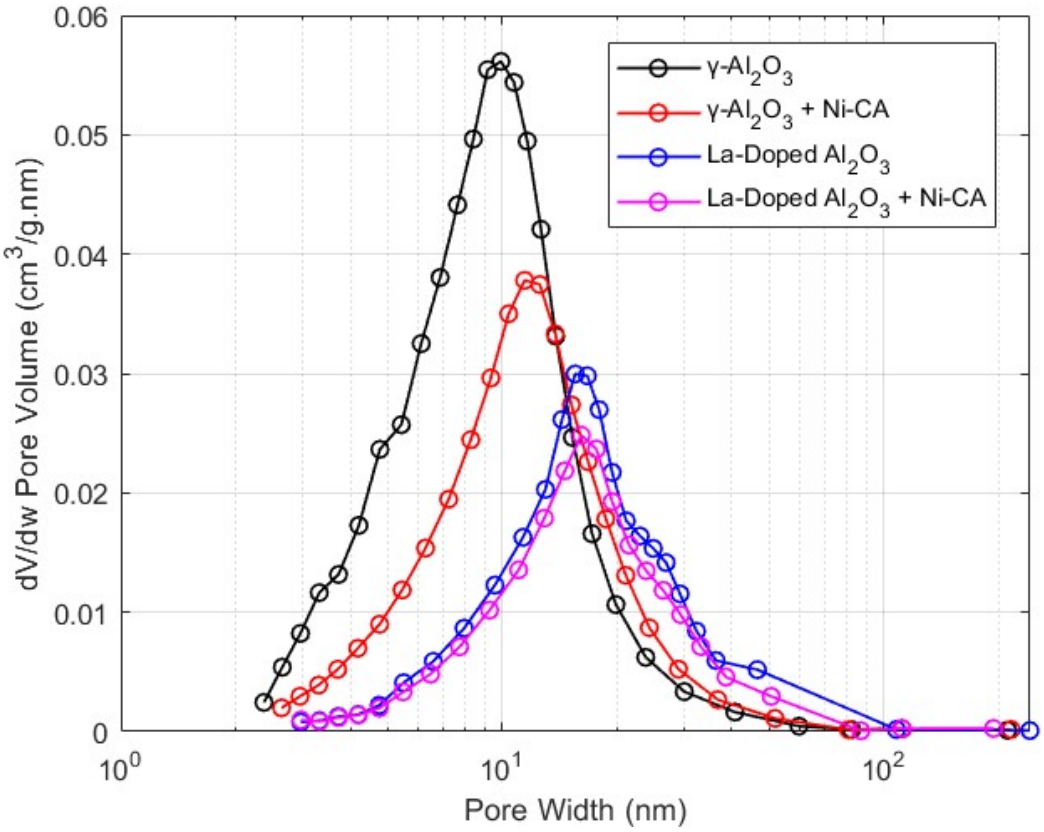

Figure 4.31. PSD of selected reduced catalyst samples after calcination at 900°C.

As shown in Figure 4.31, upon 10 wt. % Ni loading, La-doped support demonstrated more stable physical properties in terms of both surface area and pore volume. Conversely, the γ-Al_2O_3 support exhibited substantial changes under the same conditions.

4.4.3. Effect of Impregnating Solution

Variations in dispersion level are observed in catalyst samples prepared with different impregnating solutions on the same type of support. These differences can be attributed to the effects of the ligand/chelating agent on the interactions between the support surface and the nickel precursor compound, as well as changes in the interactions among the metal particles loaded onto the support surface.

Previous studies have reported that the development of carbonaceous architectures on dispersed metal catalyst systems effectively retards the process of Ostwald ripening for the metal nanoparticles, resulting in improved stability and longevity (Zhan et al., 2017).

Introduction of complexing agents, specifically NTA and CA, resulted in enhanced dispersion of metallic Ni-clusters within the synthesized catalyst samples calcined at 500°C. This significant increase in dispersion can be attributed to the stabilization of the dispersion during the drying and calcination stages, achieved via the formation of complexes with Ni^{2+} ions present in the solution. The existence of these complex compounds, characterized by their sizable bulky structure, effectively prevent the aggregation and precipitation of the molecules. This leads to their homogeneous dispersion on the surface. Moreover, these complexing agents act as intermediaries between the surface and the dispersed metals, facilitating and sustaining their dispersion, which is ultimately expected to improve the performance of the catalyst.

Upon escalating the calcination temperatures to 700°C and 900°C, an adverse impact on the dispersion of Ni-clusters was noted when synthesizing the catalyst using NTA and CA as complexing agents. It appears that the most significant change in the catalysts is the formation of the $NiAl_2O_4$ spinel structure as the calcination temperature increased. XRD analysis of $Ni(NO_3)_2$ dispersed on γ-Al_2O_3 samples at the calcination temperature of 500°C, as shown in Figure 4.28, suggested that the formation of $NiAl_2O_4$ was not favored. Consequently, to gain insight into the underlying reasons for the observed differences in Ni dispersion levels, the surface composition of Ni species was scrutinized utilizing both XRD and X-ray Photoelectron Spectroscopy (XPS).

According to the analysis of XRD results obtained, it has been observed that the particle sizes of the Ni metal and $NiAl_2O_4$ spinel on the catalyst samples, obtained using different impregnating solutions, exhibit variations as shown in Table 4.9.

Concentration ratio of the metallic Ni to the $NiAl_2O_4$ spinel on the obtained catalysts was compared through deconvoluting the individual diffraction peaks using Voigt fitting. This fitting technique combines weighted Gaussian and Lorentzian functions to separate the peaks (Varenik, 2016). Results obtained from deconvoluting the diffraction peaks are provided in Appendix D. Integrated intensity values of the resulting peaks were then evaluated for comparison.

Equation 4.21 expresses the ratio of the integrated intensities of the (111) peak of Ni and the (311) peak of $NiAl_2O_4$ in terms of their respective concentrations and angular dependent terms:

$$\frac{I_{Ni}}{I_{NiAl_2O_4}} = \frac{R_{Ni}c_{Ni}}{R_{NiAl_2O_4}c_{NiAl_2O_4}} \tag{4.21}$$

Angular dependent term ratio $\left(\frac{R_{Ni}}{R_{NiAl_2O_4}}\right)$ is assumed to be constant across all catalyst samples. This implies that the ratio of integrated intensities is directly proportional to the relative abundance of the species and can be expressed as

$$\frac{I_{Ni}}{I_{NiAl_2O_4}} \propto \frac{c_{Ni}}{c_{NiAl_2O_4}}. \tag{4.22}$$

Integrated intensity ratios are given in Table 4.10.

Table 4.10. Integrated intensity ratios of Ni (111) and $NiAl_2O_4$ (311) diffraction peaks for selected catalyst samples after reduction.

Sample	$\boldsymbol{I_{Ni\,(111)}}$	$\boldsymbol{I_{NiAl_2O_4\,(311)}}$	$\boldsymbol{\frac{I_{Ni\,(111)}}{I_{NiAl_2O_4\,(311)}}}$
γ-Al_2O_3 – $Ni(NO_3)_2$ - 700°C calc.	55.77	13.17	4.23
γ-Al_2O_3 – $Ni(NO_3)_2$ - 900°C calc.	32.77	20.05	1.63

Table 4.10. Integrated intensity ratios of Ni (111) and $NiAl_2O_4$ (311) diffraction peaks for selected catalyst samples after reduction. (cont.)

Sample	$I_{Ni\,(111)}$	$I_{NiAl_2O_4\,(311)}$	$\frac{I_{Ni\,(111)}}{I_{NiAl_2O_4\,(311)}}$
γ-Al_2O_3 – CA (1:1 mole) - 900°C calc.	55.38	11.57	4.78
γ-Al_2O_3 – EDTA (1:1 mole) - 900°C calc.	36.62	9.71	3.77
γ-Al_2O_3 – NTA (1:1 mole) - 900°C calc.	60.21	10.65	5.65

In addition to XRD, X-ray Photoelectron Spectroscopy (XPS) was employed to examine the composition of Ni species present on designated calcined and reduced samples, as shown in Figure 4.32. A comprehensive peak breakdown analysis is provided in Appendix D. To elucidate the impact of complexing agents on the incorporation of Ni into the $NiAl_2O_4$ spinel structure, samples calcined at 900°C were analyzed prior to the reduction process. This pre-reduction analysis aimed to shed light on the initial distribution of Ni-species, offering insights into the role of complexing agents in the spinel structure formation.

Existing literature points out that Ni $2p_{3/2}$ peaks can be observed at energy levels of 852 eV, 854-855 eV, and 856-857 eV, that are characteristic of metallic Ni^0, Ni^{2+} of NiO, and Ni^{2+} of $NiAl_2O_4$ spinel respectively (Iwamoto et al., 2020). Approximate areas underneath these peaks were utilized to contrast the concentration of different Ni-species on the catalyst samples. Employing the areas derived from peak deconvolution, the percentage distribution of these Ni-species on the catalyst samples was calculated. The graphical representation of this distribution can be viewed in Figure 4.33 and Figure 4.34.

The XPS analysis of samples calcined at 900°C, as detailed in Figure 4.33, shows that both NTA and CA impede the phase transition into the spinel-like structure, thereby reducing the formation of $NiAl_2O_4$ and promoting NiO generation. The XPS investigation was also expanded to encompass $Ni(NO_3)_2$ dispersed γ- Al_2O_3 samples. These samples were calcined at two different temperatures, 700°C and 900°C, with each temperature set also including their respective reduced forms. The data implied a higher propensity for $NiAl_2O_4$ formation at 900°C compared to 700°C.

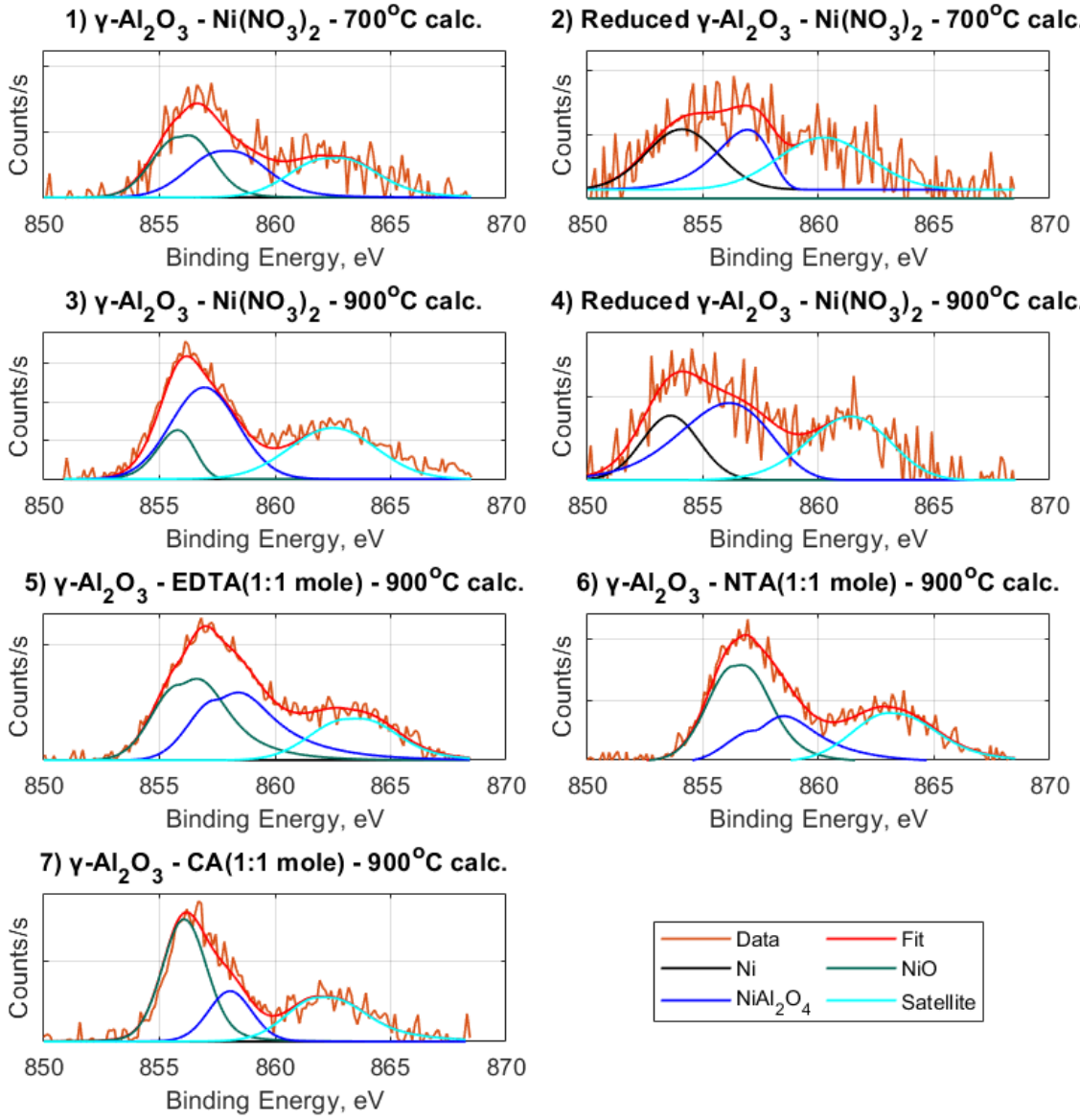

	Peak Areas			Percent Distribution		
Cat. #	**Ni**	**NiO**	**$NiAl_2O_4$**	**Ni**	**NiO**	**$NiAl_2O_4$**
1	0	3062	3021	0	50	50
2	2372	0	4595	56	0	44
3	0	5187	17190	0	23	77
4	1817	0	1418	34	0	66
5	0	9564	16729	0	36	64
6	0	11511	6669	0	63	37
7	0	7871	3118	0	72	28

Figure 4.32. XPS spectra of Ni $2p_{3/2}$ for selected 10 wt.% Ni/ γ-Al_2O_3 catalyst samples.

When contrasting the XPS data between calcined and reduced specimens, it is observed that NiO is readily and quantitatively reduced to Ni^0. However, the reduction

process of $NiAl_2O_4$ presents a greater challenge. Specifically, for the γ-Al_2O_3 - $Ni(NO_3)_2$ sample calcined at 700°C, the $NiAl_2O_4$ percentage decreased from 50% to 44% following reduction. For the γ- Al_2O_3 - $Ni(NO_3)_2$ sample calcined at 900°C, $NiAl_2O_4$ percentage was measured at 77% before reduction, and this reduced to 66% after the reduction process.

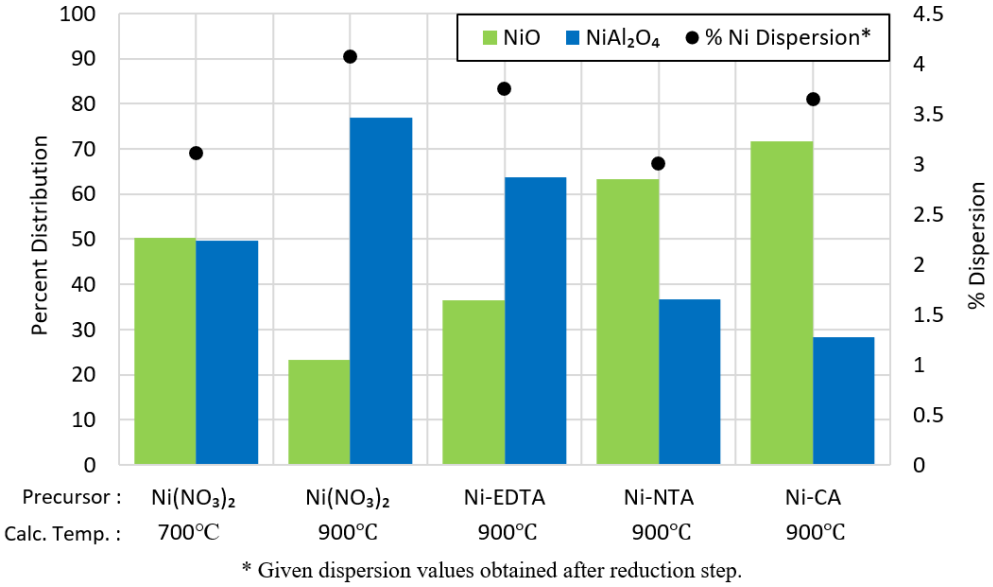

Figure 4.33. Percent distribution of Ni species on selected 10 wt.% Ni/ γ-Al_2O_3 catalyst samples before reduction step, determined by peak areas obtained from XPS analysis.

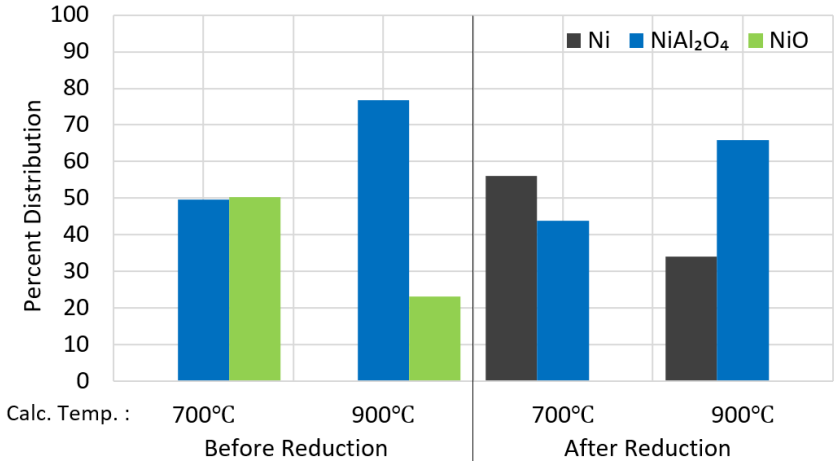

Figure 4.34. Percent distribution of Ni species' composition for 10 wt.% Ni/γ-Al_2O_3 catalyst samples prepared with $Ni(NO_3)_2$ precursor before and after the reduction step.

Consequently, data from both XPS and XRD suggest that the formation of the $NiAl_2O_4$ spinel structure can substantially influence the dispersion of Ni-clusters on Al_2O_3 support. It was observed that a higher percentage of $NiAl_2O_4$ spinel upon the calcination step at 900°C corresponded to a heightened dispersion level of Ni-clusters following the reduction phase. The robust interactions between the metal and the support surface can bolster the dispersion of Ni-clusters by enhancing their stabilization, regardless of exposure to elevated calcination temperatures and rigorous reduction conditions. This phenomenon underlines the crucial role of the $NiAl_2O_4$ spinel structure in ensuring the stability and dispersion of Ni-clusters in high-temperature catalytic processes.

The aforementioned impact of $NiAl_2O_4$ on the dispersion level of Ni-clusters was also evident on $Ni(NO_3)_2$ dispersed γ-Al2O3 sample post-calcined at 900°C, as compared to its counterpart calcined at 700°C. Conversely, the inhibitory effect of Ni-NTA and Ni-CA complexes on the formation of $NiAl_2O_4$, and consequently on the stability of the catalyst's metal dispersions, led to a significant reduction in Ni dispersion after calcination at 900°C. This effect was especially pronounced in catalysts synthesized by using NTA and CA as complexing agents.

5. CONCLUSIONS

5.1. Conclusions

Main objective of this research study was to determine the parameters necessary to enhance the dispersion level of active metal sites on supported metal catalysts prepared using DI method. Via using the Ni-Al_2O_3 catalyst as a reference model, it was aimed to establish a comprehensive methodology to enhance metal dispersion, thereby paving the way for the detailed research on the crucial aspect of dispersion-activity relation on catalyst performance optimization.

During the initial phase of the study, γ-Al_2O_3 support and its modified versions, including precalcined Al_2O_3 at 920°C and 1 wt.% La-doped Al_2O_3, were characterized to investigate their surface properties and establish a suitable physical adsorption model for optimizing the DI method. The analysis yielded several significant findings, which are summarized as follows:

- When adjusting the pH, it is crucial to take into account the pH dependence of potential species that may form in the solution, based on PZC of the support material.

- In preparation methods such as the dry impregnation method, in which high surface loading is involved, it was observed that improving electrostatic interactions plays a secondary role in dispersion improvement. Due to the strong buffering capacity of the support surface, PZC should be considered to predict the final pH of the solution and, consequently, the formation of species at the corresponding solution pH.

- To prevent the undesired formation of transition metal hydroxides, such as $Ni(OH)_{2(s)}$, which have low solubility in water, and to enhance the dispersion of metals on the support surface, utilization of complexing/chelating agents as auxiliary compounds was found beneficial.

In the second phase of the study, catalysts were prepared on the selected supports at calcination temperatures of 500°C, 700°C, and 900°C with and without using EDTA, NTA, and CA complexing agents. The catalyst preparation was based on the findings and modeling results from the earlier stage. Subsequent characterization of the prepared catalysts provided the following results:

- The results of static hydrogen chemisorption clearly indicated that the addition of NTA and CA complexing agents has a positive effect on the metal dispersion level of the catalysts especially for low-temperature (500°C) calcination.

- As the calcination temperature increased to 700°C and 900°C, dispersion level of samples prepared with NTA and CA complexing agents progressively decreased. Notably, after calcination at 900°C, the samples showed the lowest dispersion level across all catalyst series. Conversely, $Ni(NO_3)_2$ dispersed γ-Al_2O_3 samples exhibited a higher dispersion level at 900°C compared to 700°C. This difference can be attributed to the stabilizing effect of $NiAl_2O_4$ spinel structures on the dispersion of Ni-clusters. XRD and XPS analyses confirmed that the presence of NTA and CA inhibited the formation of $NiAl_2O_4$ spinel.

- Similar trends were observed in catalysts synthesized using NTA and CA complexing agents, while distinct trends were observed in catalyst samples synthesized using EDTA, a highly effective chelating agent. For the catalysts prepared with EDTA, lower calcination temperatures (500°C and 700°C) resulted in lower dispersion levels, whereas a higher dispersion level was achieved at a calcination temperature of 900°C compared to other preparation methods. Therefore, it is crucial to comprehensively examine the factors that affect dispersion, rather than making generalized conclusions based on limited observations.

Conclusively, the strategic modulation of a variety of factors, inclusive of the type of precursor, calcination temperature, and reduction conditions, plays a combined and intricate role in the optimization of metal cluster dispersion. This multi-dimensional approach enables a superior degree of control over the dispersion of metal clusters, constituting a pivotal component in the enhancement of catalyst efficiency. Therefore, comprehensive

understanding and precise management of these parameters provide a promising pathway to significantly boost the efficacy of catalysts, paving the way for future advancements in this realm of study. Presented results underscore the potential of such optimization strategies, accentuating their paramount importance in catalytic applications and offering substantial contributions to the existing body of knowledge in this scientific field.

5.2. Recommendations

Based on the findings and analysis presented in this study, several recommendations can be made to further enhance the understanding and application of the studied phenomenon. The following recommendations are proposed to address key areas of improvement and future research directions.

- The impact of denticity of complexing agents on dispersion can be investigated. To achieve this, different groups with varying denticity, consisting of diverse complexing agents with the same denticity, can be compared internally within their respective groups and also collectively.

- Dispersion enhancement experiments can be conducted using different supports and active metals, following a similar procedure.

- Modifying the structure of the complex formed with nickel is achievable by adding the complexing agents in varying molar ratios specific to nickel. This approach facilitates the determination of the optimal molar ratio for achieving the desired complex structure.

- Influence of physical conditions, including temperature and vacuum level on the Erlenmeyer flask used during the impregnation step of the DI method, can be investigated as parameters to evaluate their impact on dispersion level.

- The optimal conditions for reduction can be determined by employing the temperature programmed reduction (TPR) or for better, a combined TPR-XRD in operando manner analyses.

- To control the pH change of medium precursor solution using in DI can be improved through using a buffer solution (like Tris-EDTA buffer). This buffer helps in maintaining and regulating the pH variation of the precursor solution during the impregnation process on the support.

REFERENCES

Anderegg, G., 1982, *"*Critical Survey of Stability Constants of NTA Complexes*"*, *Pure and Applied Chemistry,* Vol. 54, No.12, pp. 2963-2758.

Anderegg, G., 2013, *Critical Survey of Stability Constants of EDTA Complexes: Critical Evaluation of Equilibrium Constants in Solution: Stability Constants of Metal Complexes,* Elsevier, Great Britain.

Apak, R., J. Hizal, and C. Ustaer, 1999, "Correlation between the Limiting pH of Metal Ion Solubility and Total Metal Concentration", *Journal of Colloid and Interface Science,* Vol. 211, No. 2, pp. 185-192.

Arnold, B., 2022, *Rubies and Implants: Aluminium Oxide and Its Diverse Facets*, Springer, Berlin, Heidelberg.

Azurdia, J. A., J. Marchal, P. Shea, H. Sun, X. Q. Pan, and R. M. Laine, 2006, "Liquid-Feed Flame Spray Pyrolysis as a Method of Producing Mixed-Metal Oxide Nanopowders of Potential Interest as Catalytic Materials. Nanopowders along the $NiO\text{-}Al_2O_3$ Tie Line Including $(NiO)_{0.22}(Al_2O_3)_{0.78}$, a New Inverse Spinel Composition", *Chemistry of Materials,* Vol. 18, No. 3, pp. 731-739.

Badoga, S., K. C. Mouli, K. K. Soni, A. K. Dalai, and J. Adjaye, 2012, "Beneficial Influence of EDTA on the Structure and Catalytic Properties of Sulfided NiMo/SBA-15 Catalysts for Hydrotreating of Light Gas Oil", *Applied Catalysis B: Environmental,* Vol. 125, pp. 67-84.

Brunelle, J. P., 1978, "Preparation of Catalysts by Metallic Complex Adsorption on Mineral Oxides", *Pure and Applied Chemistry,* Vol. 50, No: 9-10, pp. 1211-1229.

Cheng, T., J. Qiu, Y. Chen, S. Yan, M. Sun, J. Feng, M. Zhao, J. Wang, and Y. Chen, 2018, "Dispersion Improvement and Activity Promotion of Pt Catalysts Supported on a Ce-based Support by pH Adjustment", *New Journal of Chemistry,* Vol. 42, No. 19, pp. 15639-15647.

Choi, J., and D. J. Suh, 2007, "Catalytic Applications of Aerogels", *Catalysis Surveys from Asia,* Vol. 11, No. 3, pp. 123-133.

Çelebi, G., 2021, A *Study on Enhancing Thermal Stability of Alumina*, M.S. Thesis, Boğaziçi University.

Das, S., A. Jangam, Y. Du, H. Kus, and S. Kawi, 2019, "Highly Dispersed Nickel Catalysts via a Facile Pyrolysis Generated Protective Carbon Layer", *Chemical Communications,* Vol. 55, No. 43, pp. 6074-6077.

Dou, D., D. Liu, W. B. Williamson, K. C. Kharas, and H. J. Robota, 2001, "Structure and Chemical Properties of Pt Nitrate and Application in Three-way Automotive Emission Catalysts", *Applied Catalysis B,* Vol. 30, No. 1-2, pp. 11-24.

Eskandari, S., A. Dong, L. T. De Castro, F. B. Abdur Rahman, J. Lipp, D. A. Blom, and J. R. Regalbuto, 2019, "Pushing the Limits of Electrostatic Adsorption: Charge Enhanced Dry Impregnation of SBA-15", *Catalysis Today,* Vol. 338, pp. 60-71.

Ewbank, J. L., L. Kovarik, F. Z. Diallo, and C. Sievers, 2015, "Effect of Metal–Support Interactions in Ni/Al_2O_3 catalysts with Low Metal Loading for Methane Dry Reforming", *Applied Catalysis A: General,* Vol. 494, pp. 57-67.

Foger, K., 1984, "Dispersed Metal Catalysts", *Catalysis: Science and Technology*, Vol. 6, pp. 227-305.

Fogler, H. S., 2016, *Elements of Chemical Reaction Engineering*, Fifth Edition, Pearson Education, Boston.

Gonçalves, A. A., M. J. Costa, L. Zhang, F. Ciesielczyk, and M. Jaroniec, 2018, "One-Pot Synthesis of $MeAl_2O_4$ (Me = Ni, Co, or Cu) Supported on γ-Al_2O_3 with Ultralarge Mesopores: Enhancing Interfacial Defects in γ-Al_2O_3 To Facilitate the Formation of Spinel Structures at Lower Temperatures", *Chemistry of Materials,* Vol. 30, No. 2, pp. 436-446.

Han, J., K. Chanyeon, J. Park, and H. Lee, 2014, "Highly Coke-Resistant Ni Nanoparticle Catalysts with Minimal Sintering in Dry Reforming of Methane" *ChemSusChem,* Vol. 7, No. 2, pp. 451-456.

Haneda, M., T. Watanabe, N. Kamiuchi, and M. Ozawa, 2013, "Effect of Platinum Dispersion on the Catalytic Activity of Pt/Al_2O_3 for the Oxidation of Carbon Monoxide and Propene", *Applied Catalysis B: Environmental,* Vol. 142, pp. 8-14.

Hansen, T. W., A. T. DeLaRiva, S. R. Challa, and A. K. Datye, 2013, "Sintering of Catalytic Nanoparticles: Particle Migration or Ostwald Ripening?", *Accounts of Chemical Research,* Vol.46, No. 8, pp. 1720-1730.

Hao, X., W. A. Spieker, and J. R. Regalbuto, 2003, "A Further Simplification of the Revised Physical Adsorption (RPA) Model", *Journal of Colloid and Interface Science,* Vol. 267, No. 2, pp. 259-264.

Huang, Y., and J. Schwarz, 1987, "Effect of Preparation Method on Catalytic Activity of Ni/ γ-Al_2O_3 Catalysts Prepared by Wet Impregnation", *Applied Catalysis,* Vol. 30, No. 2, pp. 239-253.

Iglesias-Vázquez, S., J. Valecillos, A. Remiro, J. Bilbao, and A. G. Gayubo, 2022, "Stability of a $NiAl_2O_4$ Derived Catalyst in the Ethanol Steam Reforming in Reaction-Regeneration Cycles: Effect of Reduction Temperature", *Catalysts*, Vol. 12, No. 5, pp. 550-565.

Iwamoto, M., M. Horikoshi, R. Hashimoto, K. Shimano, T. Sawaguchi, H. Teduka, and M. Matsukata, 2020, "Higher activity of Ni/γ-Al_2O_3 over Fe/γ-Al_2O_3 and Ru/γ-Al_2O_3 for catalytic ammonia synthesis in nonthermal atmospheric-pressure plasma of N_2 and H_2", *Catalysts*, Vol. 10, No. 5, pp. 590-603.

Jos van Dillen, A., R. J. Terörde, D. J. Lensveld, J. W. Geus, and K. P. de Jong, 2003, "Synthesis of Supported Catalysts by Impregnation and Drying Using Aqueous Chelated Metal Complexes", *Journal of Catalysis,* Vol. 216, No. 1-2, pp. 257-264.

Kim, M.-Y., J.-H. Park, C.-H. Shin, S.-W. Han, and S. Gon, 2009, "Dispersion Improvement of Platinum Catalysts Supported on Silica, Silica-Alumina and Alumina by Titania Incorporation and pH Adjustment", *Catalysis Letter*, Vol. 133, pp. 288-297.

Kittaka, S., 1974, "Isoelectric Point of AI_2O_3, Cr_2O_3 and Fe_2O_3 I. Effect of Heat Treatment", *Journal of Colloid and Interface Science,* Vol. 48, No. 2, pp. 327-333.

Kwon, Y., J. E. Eichler, and C.B. Mullins, 2022, "$NiAl_2O_4$ as a Beneficial Precursor for Ni/Al_2O_3 Catalysts for the Dry Reforming of Methane", *Journal of CO_2 Utilization,* Vol. 63, pp. 102112 – 102121.

Laine, P., and R. Matilainen, 2005, "Simultaneous Determination of DTPA, EDTA, and NTA by UV–Visible Spectrometry and HPLC", *Analytical and Bioanalytical Chemistry,* Vol. 382, pp. 1601-1609.

Liu, K., and M. Ostadhassan, 2019, "The Impact of Pore Size Distribution Data Presentation Format on Pore Structure Interpretation of Shales", *Advances in Geo-Energy Research,* Vol. 3, No. 2, pp. 187-197.

Liu, L., and A. Corma, 2018, "Metal Catalysts for Heterogeneous Catalysis: From Single Atoms to Nanoclusters and Nanoparticles", *Chemical Reviews,* Vol. 118, No. 10, pp. 4981-5079.

Lu, J., J. W. Elam, and P. C. Stair, 2013, "Synthesis and Stabilization of Supported Metal Catalysts by Atomic Layer Deposition", *Accounts of Chemical Research,* Vol. 46, No. 8, pp. 1806-1815.

Ma, Z., and F. Zaera, 2006, *Encyclopedia of Inorganic Chemistry*, John Wiley & Sons, UK.

Mahmood, T., M. T. Saddique, A. Naeem, P. Westerhoff, S. Mustafa, and A. Alum, 2011, "Comparison of Different Methods for the Point of Zero Charge Determination of NiO", *Industrial & Engineering Chemistry Research,* Vol. 50, No. 17, pp. 10017-10023.

Martell, A. E., and R. D. Hancock, 2013, *Metal Complexes in Aqueous Solutions.* Springer Science & Business Media, New York.

Medici, L., and R. Prins, 1996, "Structure of Oxidic NiMo/SiO_2 Hydrotreating Catalyst Precursors", *Journal of Catalysis,* Vol. 163, No. 1, pp. 28-37.

Mehrabadi, B. A., S. Eskandari, U. Khan, R. D. White, and J. R. Regalbuto, 2017, "A Review of Preparation Methods for Supported Metal Catalysts", *Advances in Catalysis*, Vol. 61, pp. 1-35.

Morales, B. M., 2017, "Effect of Preparation Method on Catalytic Activity of Ni/γ-Al_2O_3 Catalysts", *Ingeniería. Revista de la Universidad de Costa Rica,* Vol. 27, No. 1, pp. 21-38.

Munnik, P., K. De Jong, and P. De Jongh, 2015, "Recent Developments in the Synthesis of Supported Catalysts", *Chemical Reviews*, Vol. 115, No. 14, pp. 6687-6718.

Nares, R., J. Ramirez, A. Gutiérrez-Alejandre, R. Cuevas, C. Louis, and T. Klimova, 2002, "NilHp-Zeolite Catalysts Prepared by Deposition-Precipitation", *Journal of Physical Chemistry B,* Vol. 106, No. 51, pp. 13287 - 13293.

Ortega-Domínguez, R. A., C. Peñaloza-Orta, I. Puente-Lee, C. Salcedo-Luna, and T. Klimova, 2013, "Effect of Ligands on the Dispersion of Ni Nanoparticles in Ni/SBA-15 Hydrogenation Catalysts", *Materials Research Society,* Vol. 1479, pp. 39-44.

Ortega-Domínguez, R. A., H. Vargas-Villagrán, C. Peñaloza-Orta, K. Saavedra-Rubio, X. Bokhimi, and T. Klimova, 2017, "A Facile Method to Increase Metal Dispersion and Hydrogenation Activity", *Fuel,* Vol. 198, pp. 110-122.

Park, J., and J. R. Regalbuto, 1995, "A Simple Accurate Determination of Oxide PZC and the Strong Buffering Effect of Oxide Surfaces at Incipient Wetness", *Journal of Colloid and Interface Science,* Vol. 175, pp. 239-252.

Parks, G. A., and P. L. DeBruyn, 1962, "The Zero Point of Charge of Oxides", *The Journal of Physical Chemistry,* Vol. 66, No. 6, pp. 967 - 973.

Semerjian, H. G., and D. R. Burgess, 2022, "Data Programs at NBS/NIST: 1901–2021", *Journal of Physical and Chemical Reference Data,* Vol. 51, No. 1, pp. 1-11501.

Shi, Z., C. W. Chow, R. Fabris, T. Zheng, J. Liu, and B. Jin, 2021, "Evaluation of the Impact of Suspended Particles on the UV absorbance at 254 nm (UV_{254}) Measurements using a Submersible UV-Vis Spectrophotometer", *Environmental Science and Pollution Research,* Vol. 28, No. 10, pp. 12576-12586.

Smith, R. M., and A. E. Martell, 1989, *Critical Stability Constants*, Plenum Press, New York.

Stumm, W., and J. J. Morgan, 1970, *Aquatic Chemistry.* Wiley-Interscience, New York.

Suárez-Toriello, V. A., C. E. Santolalla-Vargas, J. A. de los Reyesa, A. Vázquez-Zavala, M. Vrinat, and C. Geantet, 2015, "Influence of the Solution pH in Impregnation with Citric Acid and Activity of Ni/W/Al_2O_3 Catalysts", *Journal of Molecular Catalysis A: Chemical*, Vol. 404, pp. 36-46.

Thommes, M., K. Kaneko, A. V. Neimark, J. P. Olivier, F. Rodriguez-Reinoso, J. Rouquerol, and K. S. Sing, 2015, "Physisorption of Gases, with Special Reference to the Evaluation of Surface Area and Pore Size Distribution (IUPAC Technical Report)", *Pure and Applied Chemistry,* Vol. 87, No. 9-10, pp. 1051-1069.

To, D. T., S. H. Park, M. J. Kim, H. S. Cho, and M. V. Myung, 2022, "Effects of NH_4^+/Citrate Complexing Agent Ratio on Ni–Mo and Ni–Mo–O Electrodeposits from Ammonium Citrate Baths", *Frontiers in Chemistry,* Vol. 10, pp. 1-12.

van de Loosdrecht, J., M. van der Haar, A. M. van der Kraan, A. J. van Dillen, and J. W. Geus, 1997, "Preparation and Properties of Supported Cobalt Catalysts for Fischer-Tropsch Synthesis", *Applied Catalysis A,* Vol. 150, pp. 365-376.

Varenik, M., 2016, "Peak Fitting to Either Voigt or LogNormal Line Shapes", https://www.mathworks.com/matlabcentral/fileexchange/52321-peak-fitting-to-either-voigt-or-lognormal-line-shapes, accessed on May 12, 2023.

Wang, G., X. Sun, X. Niu, F. Meng, and F. Wang, 2017, "Effect of Chelating Agents on Catalytic Performance of Cr/γ-Al_2O_3 Dehydrogenation Catalysts", *Chemical Papers*, Vol. 72, pp. 921-928.

Wash, I. E., F. D. Hardcastle, and S. S. Chan, 1986, "Raman Spectroscopy of Supported Metal Oxide Catalysts", *Spectroscopy*, Vol. 1, No. 8, pp. 30-38.

Wong, A., Q. Liu, S. Griffin, A. Nicholls, and J. R. Regalbuto, 2017, "Synthesis of Ultrasmall Homogeneously Alloyed, Bimetallic Nanoparticles on Silica Supports", *Science,* Vol. 358, No. 6369, pp. 1427-1430.

Yao, Y., C. Zhang, Z. Jing, F. Ding, and J. Wu, 2013, "Thermodynamics Analysis of Ni^{2+}–$C_2H_8N_2$ − $C_2O_4^-$ − H_2O System and Preparation of Ni Microfiber", *Transactions of Nonferrous Metals Society of China,* Vol. 23, No. 11, pp. 3456-3461.

Zhan, W., Y. Shu, Y. Sheng, H. Zhu, Y. Guo, L. Wang, J. Zhang, G. Lu, and S. Dai, 2017, "Surfactant-Assisted Stabilization of Au Colloids on Solids for Heterogeneous Catalysis", *Angewandte Chemie International Edition*, Vol. 56, No. 16, pp. 4494-4498.

Zhang, Q., K. Long, J. Wang, T. Zhang, Z. Song, and Q. Lin, 2017, "A Novel Promoting Effect of Chelating Ligand on the Dispersion of Ni Species over Ni/SBA-15 Catalyst for Dry Reforming of Methane", *International Journal of Hydrogen Energy,* Vol. 42, No. 20, pp. 14103-14114.

Zhou, L., L. Li, N. Wei, J. Li, and J.-M. Basset, 2015, "Effect of $NiAl_2O_4$ Formation on Ni/Al_2O_3 Stability during Dry Reforming of Methane", *ChemCatChem,* Vol. 7, No. 16, pp. 2508-2516.

Zhu, X., H. R. Cho, M. Pasupong, and J. R. Regalbuto, 2013, "Charge-Enhanced Dry Impregnation: A Simple Way to Improve the Preparation of Supported Metal Catalysts", *American Chemical Society of Catalysis,* Vol 3, No. 4, pp. 625-630.

APPENDIX A: STABILITY CONSTANTS FOR THERMODYNAMIC CALCULATIONS

Table A.1. Solubility product of $Ni(OH)_2$.

Reaction	log K_{sp}	Reference
$Ni^{2+} + 2OH^- \rightleftharpoons Ni(OH)_2(s)$	14.7	(Yao et al., 2013)

Table A.2. Cumulative formation constants of possible complexes in impregnating solution of $Ni(NO_3)_2$.

Reaction	log β	Reference
$Ni^{2+} + OH^- \rightleftharpoons NiOH^+$	4.10	CSC[1]
$Ni^{2+} + 2OH^- \rightleftharpoons Ni(OH)_2°$	8.00	CSC[1]
$2Ni^{2+} + OH^- \rightleftharpoons Ni_2OH^{3+}$	3.30	CSC[1]
$4Ni^{2+} + 4OH^- \rightleftharpoons Ni_4(OH)_4^{4+}$	28.30	CSC[1]

Table A.3. Equilibrium constant of protonation of ammonium ions at 298 K.

Reaction	log K	Reference
$NH_3 + H_3O^+ \rightleftharpoons NH_4^+ + H_2O$	9.244	CSC[1]

Table A.4. Cumulative formation constants of nickel-ammonia complexes at 298 K.

Reaction	log β	Reference
$Ni^{2+} + NH_3 \rightleftharpoons \mathrm{Ni}(NH_3)^{2+}$	2.79	CSC[1]
$Ni^{2+} + 2NH_3 \rightleftharpoons \mathrm{Ni}(NH_3)_2^{2+}$	5.03	CSC[1]
$Ni^{2+} + 3NH_3 \rightleftharpoons \mathrm{Ni}(NH_3)_3^{2+}$	6.76	CSC[1]
$Ni^{2+} + 4NH_3 \rightleftharpoons \mathrm{Ni}(NH_3)_4^{2+}$	7.95	CSC[1]
$Ni^{2+} + 5NH_3 \rightleftharpoons \mathrm{Ni}(NH_3)_5^{2+}$	8.70	CSC[1]
$Ni^{2+} + 6NH_3 \rightleftharpoons \mathrm{Ni}(NH_3)_6^{2+}$	8.73	CSC[1]

[1] (Smith & Martell, 1989)

Table A.5. Cumulative formation constants of nickel-EDTA complexes at 298 K.

Reaction	log β	Reference
$Ni^{2+} + EDTA^{4-} \rightleftharpoons [\mathrm{Ni}(EDTA)]^{2-}$	18.4	CSC[1]
$Ni^{2+} + EDTA^{4-} + \mathrm{H}^{+} \rightleftharpoons [\mathrm{NiH}(EDTA)]^{-}$	21.5	CSC[1]
$Ni^{2+} + EDTA^{4-} + 2H^{+} \rightleftharpoons [\mathrm{NiH_2}(EDTA)]$	22.4	CSC[1]
$Ni^{2+} + EDTA^{4-} \rightleftharpoons [\mathrm{NiOH}(EDTA)]^{3-} + H^{+}$	6.50	CSC[1]
$Ni^{2+} + EDTA^{4-} + NH_3 \rightleftharpoons [\mathrm{Ni}(EDTA)(\mathrm{NH_3})]^{2-}$	20.96	CSSC-EDTA[2]

Table A.6. Cumulative equilibrium constants for acid-base equilibrium reaction of EDTA at 298 K.

Reaction	log β	Reference
$EDTA^{4-} + H^{+} \rightleftharpoons \mathrm{H}EDTA^{3-}$	11.014	CSC[1]
$EDTA^{4-} + 2H^{+} \rightleftharpoons \mathrm{H_2}EDTA^{2-}$	17.334	CSC[1]
$EDTA^{4-} + 3H^{+} \rightleftharpoons \mathrm{H_3}EDTA^{-}$	20.024	CSC[1]
$EDTA^{4-} + 4H^{+} \rightleftharpoons \mathrm{H_4}EDTA$	22.024	CSC[1]

Table A.7. Cumulative equilibrium constants for acid-base equilibrium reaction of NTA at 298 K.

Reaction	log β	Reference
$NTA^{3-} + H^{+} \rightleftharpoons \mathrm{HNTA}^{2-}$	10.334	CSC[1]
$NTA^{3-} + 2H^{+} \rightleftharpoons \mathrm{H_2NTA}^{-}$	13.274	CSC[1]
$NTA^{3-} + 3H^{+} \rightleftharpoons \mathrm{H_3}NTA$	15.374	CSC[1]
$NTA^{3-} + 4H^{+} \rightleftharpoons \mathrm{H_4NTA}^{+}$	16.674	CSC[1]

Table A.8. Cumulative formation constants of nickel-NTA complexes at 298 K.

Reaction	log β	Reference
$Ni^{2+} + NTA^{3-} \rightleftharpoons \mathrm{Ni(NTA)}^{-}$	10.0	CSC[1]
$Ni^{2+} + 2NTA^{3-} \rightleftharpoons \mathrm{Ni(NTA)_2}^{4-}$	14.7	CSC[1]
$Ni^{2+} + NTA^{3-} + \mathrm{NH_3} \rightleftharpoons Ni(NTA)(NH_3)^{-}$	12.54	CSSC-NTA[3]

[1] (Smith & Martell, 1989)
[2] (Anderegg, 2013)
[3] (Anderegg, 1982)

Table A.9. Cumulative equilibrium constants for acid-base equilibrium reaction of citric acid at 298 K.

Reaction	log β	Reference
$Cit^{3-} + H^+ \rightleftharpoons \mathrm{HCit}^{2-}$	5.72	(To et al., 2022)
$Cit^{3-} + 2H^+ \rightleftharpoons \mathrm{H_2}Cit^-$	10.09	(To et al., 2022)
$Cit^{3-} + 3H^+ \rightleftharpoons \mathrm{H_3}Cit$	13.03	(To et al., 2022)
$Cit^{3-} \rightleftharpoons \mathrm{H_{-1}}Cit^{4-} + H^+$	-11.8	(To et al., 2022)

Table A.10. Cumulative formation constants of nickel-citric acid complexes at 298 K.

Reaction	log β	Reference
$Ni^{2+} + Cit^{3-} \rightleftharpoons \mathrm{NiCit}^-$	5.56	CSC[1]
$Ni^{2+} + Cit^{3-} + \mathrm{H}^+ \rightleftharpoons \mathrm{NiHCit}$	9.26	CSC[1]
$Ni^{2+} + Cit^{3-} + 2H^+ \rightleftharpoons \mathrm{NiH_2Cit}^+$	11.8	CSC[1]
$Ni^{2+} + 2Cit^{3-} \rightleftharpoons \mathrm{NiCit_2}^{4-}$	8.58	CSC[1]
$Ni^{2+} + 2Cit^{3-} + \mathrm{H}^+ \rightleftharpoons \mathrm{NiHCit_2}^{3-}$	13.87	CSC[1]
$2Ni^{2+} + 2Cit^{3-} \rightleftharpoons \mathrm{Ni_2(H_{-1}Cit)_2}^{4-} + 2\mathrm{H}^+$	-3.96	CSC[1]

[1] (Smith & Martell, 1989)

APPENDIX B: DETAILS OF THE PHYSICAL ADSORPTION MODEL CALCULATIONS

B.1. Derivations for pH Shift Model

The surface charge density, denoted by σ_0, can be expressed in terms of the surface density of Al_2O_3, N_s, taking into account the protonating and deprotonating equilibrium reactions given in Equation 4.2 and Equation 4.3, can be expressed as

$$\sigma_0 = eN_s \frac{([AlOH_2^+] - [AlO^-])}{([AlOH] + [AlOH_2^+] + [AlO^-])} \tag{B.1}$$

where the concentrations of surface species can also be related to $[H_s^+]$ through Equation 4.4 and 4.5. If Boltzmann distribution is used to relate bulk proton concentration $[H^+]$ to $[H_s^+]$, this equality can be written as

$$[H_s^+] = [H^+] \exp\left(-\frac{e\psi_0}{2kT}\right) \tag{B.2}$$

where, ψ_0 represents the surface potential (Zhu et al., 2013). By substituting Equations 4.4, 4.5, and B.2 into Equation B.1, surface charge density can be written as

$$\sigma_0 = eN_s \frac{\left(\frac{[H^+]\exp\left(-\frac{e\psi_0}{2kT}\right)}{K_1} - \frac{K_2}{[H^+]\exp\left(-\frac{e\psi_0}{2kT}\right)}\right)}{\left(1 + \frac{[H^+]\exp\left(-\frac{e\psi_0}{2kT}\right)}{K_1} + \frac{K_2}{[H^+]\exp\left(-\frac{e\psi_0}{2kT}\right)}\right)}. \tag{B.3}$$

Therefore, surface charge density can be calculated using the pH of the solution at equilibrium. However, in Equation B.3, equilibrium constants K_1 and K_2, oxide surface density N_s, and surface potential ψ_0 are also unknowns. Hence, additional equations are required to determine these unknowns.

At the point of zero charge (PZC), concentrations of positively charged sites, $[Al-OH_2^+]$, and negatively charged sites, $[Al-O^-]$, must be equal to each other. Therefore, PZC can be expressed as

$$\frac{pK_1+pK_2}{2}=PZC \tag{B.4}$$

Proof. We will apply the minus logarithm to both sides of equilibrium relations described in Equation 4.4 and 4.5.

$$\begin{aligned} -\log K_1 &= -\log\left(\frac{[Al-OH][H_s^+]}{[Al-OH_2^+]}\right) \\ pK_1 &= \log[Al-OH_2^+] - \log[Al-OH] - \log[H_s^+] \\ -\log K_2 &= -\log\left(\frac{[Al-O^-][H_s^+]}{[Al-OH]}\right) \\ pK_2 &= \log[Al-OH] - \log[Al-O^-] - \log[H_s^+] \end{aligned}$$

For $[Al-O^-] = [Al-OH_2^+]$ and $-\log[H_s^+] = PZC$ at PZC, sum of $pK_1$and pK_2 can be written as

$$\begin{aligned} pK_1+pK_2 &= \log[Al-OH_2^+] - \log[Al-O^-] - 2\log[H_s^+] \\ &= 2\times PZC \end{aligned}$$

which implies

$$PZC=\frac{pK_1+pK_2}{2}$$

as required.

By considering this relation, pK_1 and pK_2 can be expressed in terms of PZC and their difference $pK_2-pK_1=\Delta$pK, as

$$pK_1 = PZC-\frac{1}{2}\Delta pK \tag{B.5}$$

$$pK_2 = PZC+\frac{1}{2}\Delta pK \tag{B.6}$$

where ΔpK is not depend on near surface proton concentration.

By using Gouy-Chapman theory, surface charge distribution and surface potential can be related as

$$\sigma_0 = (8 \times 10^{-5} \varepsilon \varepsilon_0 RIT)^{1/2} \sinh\left(\frac{e\psi_0}{2kT}\right). \quad \text{(B.7)}$$

Surface charge density can also be calculated by using final pH (at equilibrium) and initial pH of solution. Protonation and deprotonation of hydroxyl groups on the support surface point is the source of surface charges. Therefore, proton balance was written as

$$\sigma_0 = \frac{F}{ws}\left[\left([H^+]_{initial} - [OH^-]_{initial}\right) - \left([H^+]_{final} - [OH^-]_{final}\right)\right] \quad \text{(B.8)}$$

where

$$[H^+]_{initial/final} = \frac{c^0}{\gamma_{H_3O^+}} 10^{-pH_{initial/final}} \quad \text{(B.9)}$$

$$[OH^-]_{initial/final} = \frac{c^0}{\gamma_{OH^-}} 10^{-(14-pH_{initial/final})}. \quad \text{(B.10)}$$

Activity coefficient of final solution at equilibrium is calculated by using Güntelberg approximation (Stumm and Morgan, 1970) – simplification of extended Debye-Hückel equation- which is useful for ionic strengths up to 0.1 M and at 25 ºC activity coefficients can be expressed as

$$\log \gamma_x = -0.51\, Z_x^2 \left(\frac{\sqrt{I}}{1+\sqrt{I}}\right). \quad \text{(B.11)}$$

B.2. Derivations for Physical Adsorption Model

Langmuir isotherm equation is used to calculate the adsorption densities (Zhu et al., 2013), providing information on the amount of adsorbate bound to the surface under specific pH, total metal concentration, and ionic strength conditions and can be written as

$$\left(\frac{\Gamma}{\Gamma_{max}}\right) = \frac{KC}{1+KC}. \quad \text{(B.12)}$$

To calculate the maximum adsorption density, Γ_{max} (in moles/m^2), following equation can be employed, taking into account a densely packed layer of adsorbates with n_{hs} hydration sheath (Zhu et al., 2013):

$$\Gamma_{max} = \left[\frac{1}{N_0 \pi (r_{ion} + 2n_{hs} r_w)^2}\right] \tag{B.13}$$

For the precursor solution of $Ni(NO_3)_2$, retaining one hydration sheet, with the ionic radius of the Ni^{2+} ion, r_{ion}, set at approximately 0.79 Å (Ewbank et al.,2015) and the radius of a water molecule, r_w, at approximately 1.35 Å (Zhu et al., 2013).

The adsorption equilibrium constant, K, is calculated solely based on the contribution of coulombic forces between the surface and nickel ions which can be expressed as

$$K = \exp\left(-\frac{\Delta G_{ads}}{RT}\right) = \exp\left(-\frac{\Delta G_{coul}}{RT}\right) \tag{B.14}$$

and coulombic energy term is calculated as a function of the potential at the plane of adsorption

$$\Delta G_{coul} = ZF\psi_x \tag{B.15}$$

where the potential, denoted as ψ_x , is calculated by assuming a simplified electric double layer model where all species adsorb in a single plane (Zhu et al., 2013).

$$\psi_x = \left[\frac{2RT}{ZF}\right] \ln\left(\frac{(Y+1) + (Y-1)\exp(-\kappa x)}{(Y+1) - (Y-1)\exp(-\kappa x)}\right) \tag{B.16}$$

Where $x = r_{ion} + 2n_{hs} r_w$ and $Y = \exp\left(\frac{ZF\psi_0}{2RT}\right)$.

Surface potential ψ_0 is found in pH shift calculations and κ is the e Debye–Hückel reciprocal double-layer length which quantifies the extent of electrostatic screening in the solution and is dependent on the ionic strength of the system as

$$\kappa = 3.31 \times 10^9 \sqrt{I} \ \ (m^{-1}), \quad I = \frac{1}{2}\sum_i Z_i^2 C_i \tag{B.17}$$

APPENDIX C: COMPUTER CODES

C.1. MATLAB Codes for pH Shift Model of Supports

```
clc; clear all; close all;

% Variables depend on support and solution

epsilon = 78.41;      % the relative dielectric constant of the solution
dpk=5.0;              % pK2 - pK1 difference of Al2O3
V_sample = 0.025;     % volume of precursor solution, [L]
m_added_list = [0.1134,0.1888,0.2174];    % added mass of support, [g]
M_ionic = 0.1*20/25;  % salt concentration, [M]
cat_num = 1;          % # of cations per formula
cat_charge = +1;      % charge of cation
an_num = 1;           % # of anions per formula
an_charge = -1;       % charge of anion
support = ["γ-Al_2O_3","δ-Al_2O_3","La-doped-Al_2O_3"]; % support type
tsa_list = [220.51, 132.39, 114.98]; % total surface areas of supports, [m^2/g]
PZC_list = [8.49, 8.42, 7.82];       % point of zero charges of supports
N_s_list = [8, 14.34, 14.7]*10^14;   % surface site hydroxyl densities,
[#OH/cm^2]:

% Fixed values for PZC Calculations

k = 1.38066*10^-23;           % Boltzmann constant,[J/K]
c_0 = 1;                      % standard concentration, [mol/L]
R = 8.3145;                   % gas constant, [J.mol^-1.K^-1]
T = 298.15;                   % temperature of suspension, [K]
eta = 1.6*10^-19;             % electric quantity of an electron, [C]
F = 96490;                    % Faradaic constant, [C/mol]
epsilon_0 = 8.854188*10^-12;  % the vacuum permittivity,[F/m]
N_0 = 6.022*10^23;            % Avogadro number, [1/mol]

% Equations

for i=1:length(support)

    m_added = m_added_list(i);
    tsa = tsa_list(i); PZC = PZC_list(i); N_s = N_s_list(i);

    w = m_added/V_sample;         % mass concentration of Al2O3, [g/L]
    K_1 = 10^-(PZC-0.5*dpk);      % Acid dissociation constant 1
    K_2 = 10^-(PZC+0.5*dpk);      % Acid dissociation constant 2

    j=0;

    for pH=0:0.1:14

        j=j+1; % counter

        syms p r s t

        % p - final pH
```

```
        % r - Surface charge distribution, C/cm^2
        % s - Surface potential, J/C
        % t - ionic strength of final solution

        %Equationd for ionic strength of initial (I_in) and final (t) solutions

        I_in = 0.5*(10^-pH + 10^(pH-14) + cat_num*M_ionic*cat_charge^2 ...
            + an_num*M_ionic*an_charge^2 );

        eqn1 = 0.5*((10^-14)/p + p + cat_num*M_ionic*cat_charge^2 ...
            + an_num*M_ionic*an_charge^2 )== t;

        % Activity coefficients calculated by using Guntelberg approximation
        gamma_i = 10^(-0.51*(sqrt(I_in)/(1+sqrt(I_in))));  % initial solution
        gamma_f = 10^(-0.51*(sqrt(t)/(1+sqrt(t))));        % final solution

        % Proton balance equation for surface charge distribution
        eqn2 = ((10^-4)*(F/(w*tsa))*(((10^-pH)/gamma_i-(10^(pH-
14))/gamma_i)+...
            (((10^-14)/p - p))*(1/gamma_f))) == r;

        % Surface charge distribution from Gouy-Chapman theory
        eqn3 = ((sqrt(8*10^-5*epsilon*epsilon_0*k*T*N_0*t))*...
            sinh(eta*s/(2*k*T))) == r;

        % Surface charge distribution equation from equilibrium calculations
        eqn4 = ((((p*(exp(-eta*s/(2*k*T)))/K_1)-...
            (K_2*(exp(eta*s/(2*k*T)))/p))/...
            (1+(p*(exp(-eta*s/(2*k*T)))/K_1)+...
            (K_2*(exp(eta*s/(2*k*T)))/p)))*eta*N_s) == r;

        % For initial guess:

        if pH<= PZC
            x0=[PZC, 1e-2, -1e-1, M_ionic];
        else
            x0=[pH, -1e-2, -1e-1, M_ionic];
        end

        % Modified version of Newton method for numerical root finding:
        X=vpasolve([eqn1,eqn2,eqn3,eqn4],[p,r,s,t],[10^-
x0(1),x0(2),x0(3),x0(4)]);

        TF = isempty(X.p) || imag(X.p)~=0 || imag(-log10(X.p))~=0;

        if TF==0
            sol(j,4*i-3) = pH;
            sol(j,4*i-2) = -log10(X.p);
            sol(j,4*i-1) = X.r;
            sol(j,4*i) = X.s;
        else
            j=j-1;
        end
    end

    subplot(1,3,i)
    plot(sol(:,4*i-3),sol(:,4*i-2));
    title(['Final vs initial pH for ',support(i)]);
```

```
    xlabel('Initial pH'); xlim([0 14]);
    ylabel('final pH');
    grid on;

end
```

C.2. MATLAB Codes for Simplified Physical Adsorption Model

```
clc; clear all; close all;

% Variables depend on support and solution

epsilon = 78.41;      % the relative dielectric constant of the solution
dpk=5.0;              % pK2 - pK1 difference of Al2O3
V_sample = 0.0032;    % volume of precursor solution, [L]
m_added_list = 3.2354*[1,1,1];    % added mass of support, [g]
M_ionic = 1.91402;    % salt concentration, [M]
cat_num = 1;          % # of cations per formula
cat_charge = +2;      % charge of cation
an_num = 2;           % # of anions per formula
an_charge = -1;       % charge of anion
support = ["γ-Al_2O_3","δ-Al_2O_3","La-doped-Al_2O_3"]; % support type
tsa_list = [220.51, 132.39, 114.98]; % total surface areas of supports, [m^2/g]
PZC_list = [8.49, 8.42, 7.82];       % point of zero charges of supports
N_s_list = [8, 14.34, 14.7]*10^14;   % surface site hydroxyl densities,
[#OH/cm^2]:

% Fixed values for PZC Calculations

k = 1.38066*10^-23;           % Boltzmann constant,[J/K]
c_0 = 1;                      % standard concentration, [mol/L]
R = 8.3145;                   % gas constant, [J.mol^-1.K^-1]
T = 298.15;                   % temperature of suspension, [K]
eta = 1.6*10^-19;             % electric quantity of an electron, [C]
F = 96490;                    % Faradaic constant, [C/mol]
epsilon_0 = 8.854188*10^-12;  % the vacuum permittivity,[F/m]
N_0 = 6.022*10^23;            % Avogadro number, [1/mol]

% Equations

for i=1:length(support)  % Calculations are repeated for all support types

    m_added = m_added_list(i);
    tsa = tsa_list(i); PZC = PZC_list(i); N_s = N_s_list(i);

    w = m_added/V_sample;         % mass concentration of Al2O3, [g/L]
    K_1 = 10^-(PZC-0.5*dpk);      % Acid dissociation constant 1
    K_2 = 10^-(PZC+0.5*dpk);      % Acid dissociation constant 2

    j=0;

    for pH=0:0.1:14

        j=j+1; % counter

        syms p r s t
```

```
        % p - final pH
        % r - Surface charge distribution, C/cm^2
        % s - Surface potential, J/C
        % t - ionic strength of final solution

        %Equationd for ionic strength of initial (I_in) and final (t) solutions

        I_in = 0.5*(10^-pH + 10^(pH-14) + cat_num*M_ionic*(cat_charge)^2 ...
            + an_num*M_ionic*(an_charge)^2 );

        eqn1 = 0.5*((10^-14)/p + p + cat_num*M_ionic*cat_charge^2 ...
            + an_num*M_ionic*an_charge^2 )== t;

        % Activity coefficients calculated by using Guntelberg approximation
        gamma_i = 10^(-0.51*(sqrt(I_in)/(1+sqrt(I_in))));  % initial solution
        gamma_f = 10^(-0.51*(sqrt(t)/(1+sqrt(t))));        % final solution

        % Proton balance equation for surface charge distribution
        eqn2 = ((10^-4)*(F/(w*tsa))*(((10^-pH)/gamma_i-(10^(pH-
14))/gamma_i)+...
            (((10^-14)/p - p))*(1/gamma_f))) == r;

        % Surface charge distribution from Gouy-Chapman theory
        eqn3 = ((sqrt(8*10^-5*epsilon*epsilon_0*k*T*N_0*t))*...
            sinh(eta*s/(2*k*T))) == r;

        % Surface charge distribution equation from equilibrium calculations
        eqn4 = ((((p*(exp(-eta*s/(2*k*T)))/K_1)-...
            (K_2*(exp(eta*s/(2*k*T)))/p))/...
            (1+(p*(exp(-eta*s/(2*k*T)))/K_1)+...
            (K_2*(exp(eta*s/(2*k*T)))/p)))*eta*N_s) == r;

        % For initial guess:

        if pH<= PZC
            x0=[PZC, 1e-2, -1e-1, M_ionic];
        else
            x0=[pH, -1e-2, -1e-1, M_ionic];
        end

        % Modified version of Newton method for numerical root finding:
        X=vpasolve([eqn1,eqn2,eqn3,eqn4],[p,r,s,t],[10^-
x0(1),x0(2),x0(3),x0(4)]);

        TF = isempty(X.p) || imag(X.p)~=0 || imag(-log10(X.p))~=0;

        if TF==0
            sol(j,5*i-4) = pH;
            sol(j,5*i-3) = -log10(X.p);
            sol(j,5*i-2) = X.r;
            sol(j,5*i-1) = X.s;
            sol(j,5*i  ) = X.t;
        else
            sol(j,5*i-4) = NaN;
            sol(j,5*i-3) = NaN;
            sol(j,5*i-2) = NaN;
            sol(j,5*i-1) = NaN;
            sol(j,5*i  ) = NaN;
```

```
    end
end

figure
subplot(2,2,1)
plot(sol(:,5*i-4),sol(:,5*i-3),'LineWidth',1.5);
set(gca,'FontSize',12);
title(['Final vs initial pH for ',support(i)]);
xlabel('Initial pH'); xlim([0 14]);
ylabel('Final pH'); ylim([0 14]);
grid on;

subplot(2,2,2)
plot(sol(:,5*i-3),sol(:,5*i-2),'LineWidth',1.5);
set(gca,'FontSize',12);
title(['Surface charge density vs initial pH for ',support(i)]);
xlabel('Final pH'); xlim([0 14]);
ylabel('Surface Charge Density, C/cm^2');
grid on;

subplot(2,2,3)
plot(sol(:,5*i-3),sol(:,5*i-1),'LineWidth',1.5);
set(gca,'FontSize',12);
title(['Surface potential vs initial pH for ',support(i)]);
xlabel('Final pH'); xlim([0 14]);
ylabel('Surface potential, J/C');
grid on;

% Simplified Physical Adsorption Model

B=sol(:,5*i-4:5*i);   % Solution obtained from pH shift model
for j=1:size(B,1)

    I(j) = B(j,5);    % Ionic strengt of solution, M
    % Debye-Hückel reciprocal double-layer length, m^-1
    kappa(j)=(3.31*10^9)*sqrt(I(j));
    r_w = 1.35*10^-10;     % radius of water molecule, m
    r_Ni = 0.79*10^-10;    % radius of Ni^2+ ion, m
    x = (r_Ni + 2*r_w);
    Y(j) = exp(F*B(j,4)/(2*R*T));

    % potential at the plane of adsorption:
    psi_x(j) = (2*R*T/F)*log(((Y(j)+1)+(Y(j)-1)*...
        exp(-kappa(j)*x))/((Y(j)+1)-(Y(j)-1)*...
        exp(-kappa(j)*x)));
    z = +2;                          % charge of adsorbed Ni ion
    G(j) = z*F*psi_x(j);             % Coulombic gibbs free energy
    K(j) = exp(-G(j)/(R*T));         % Adsorption equilibrium const.
    conc = M_ionic;
    gamma_max = 1/(N_0*pi*(x^2));    % Max. adsorption density
    gamma_dist(j) = gamma_max*K(j)*conc/(1+K(j)*conc); % Metal uptake

end

subplot(2,2,4)
plot(B(:,2),gamma_dist*10^6,'LineWidth',1.5);
set(gca,'FontSize',12);
title('Surface covarage vs final pH');
```

```
    xlabel('Final pH'); xlim([0 14]);
    ylabel('Surface covarage, µmole/m^2');
    grid on;
end
```

C.3. MATLAB Codes for Thermodynamic Prediction of Complexes in $Ni(NO_3)_2$ – Ammonia Precursor Solution

```
clc; close all; clear all;

global OH K K_w c_NiNO3

K_w = 10^-14;  % water autoionization constant
logK = [9.244 2.79 5.03 6.76 7.95 8.70 8.73 14.7]; % log K values
K = 10.^logK; % stability constants

j=1;
for i=0:0.1:14          % pH increments
    OH = 10^-(14-i);    % [OH^-] in solution
    x0 = ones(1,2);     % Initial guess
    options = optimoptions('fsolve','Display','iter');
    options.Algorithm ='trust-region-dogleg';
    [x,fval]= fsolve(@ammoniaequations,x0,options);  % Solution of eq'ns
    pH(j)=i;
    Sol(j,:) = [pH(j),x];
    j=j+1;
end

% Molar fractions of each Ni species
NiNH3 = K(2).*Sol(:,2).*Sol(:,3)/c_NiNO3;
NiNH3_2 =K(3).*Sol(:,2).*Sol(:,3).^2 /c_NiNO3;
NiNH3_3 = K(4).*Sol(:,2).*Sol(:,3).^3/c_NiNO3;
NiNH3_4 = K(5).*Sol(:,2).*Sol(:,3).^4/c_NiNO3;
NiNH3_5 = K(6).*Sol(:,2).*Sol(:,3).^5/c_NiNO3;
NiNH3_6 = K(7).*Sol(:,2).*Sol(:,3).^6/c_NiNO3;
NiNH3_n = (NiNH3 + NiNH3_2 + NiNH3_3 + NiNH3_4 +...
    + NiNH3_5 + NiNH3_6);
NiOH_2 = K(8).*Sol(:,2).*((10.^-(14-Sol(:,1))).^2)/c_NiNO3;

plot (Sol(:,1),Sol(:,2)/c_NiNO3,'go-', Sol(:,1),NiOH_2,'rx-',...
    Sol(:,1),NiNH3_n,'b--', Sol(:,1),NiNH3,...
    Sol(:,1),NiNH3_2, Sol(:,1),NiNH3_3,...
    Sol(:,1),NiNH3_4, Sol(:,1),NiNH3_5,...
    Sol(:,1),NiNH3_6,'LineWidth',1.5);

legend ('[Ni(H_2O)_6]^2^+','Ni(OH)_2(s)','[Ni(NH_3)_n(H_2O)_6_-_n]^2^+',...
    '[Ni(NH_3)(H_2O)_5]^2^+','[Ni(NH_3)_2(H_2O)_4]^2^+',...
    '[Ni(NH_3)_3(H_2O)_3]^2^+','[Ni(NH_3)_4(H_2O)_2]^2^+',...
    '[Ni(NH_3)_5(H_2O)]^2^+','[Ni(NH_3)_6]^2^+',Location='bestoutside');

xlabel('pH of solution'); ylabel('Molar fraction of Ni');
grid on;
set(gca,'FontSize',12);
```

```
function y = ammoniaequations(x)
y = zeros(2,1);

global OH K K_w c_NiNO3

c_NiNO3 = 1.91402;       % Initial Ni(NO3)2 conc.
c_NH3 = (13.4*2.4/3.2);  % Initial ammonia conc.

% x(1)=Ni2+ ; x(2)=NH3;

% Nickel mass balance
y(1)= x(1)*(1 + K(2)*x(2) + K(3)*x(2)^2 + K(4)*x(2)^3 ...
    + K(5)*x(2)^4 + K(6)*x(2)^5 + K(7)*x(2)^6 ...
    + K(8)*OH^2) - c_NiNO3;

% Ammonia mass balance
y(2)= x(2)*(1 + K(1)*K_w/OH + x(1)*(K(2) + 2*K(3)*x(2)...
    + 3*K(4)*x(2)^2 + 4*K(5)*x(2)^3 + 5*K(6)*x(2)^4 ...
    + 6*K(7)*x(2)^5)) - c_NH3;

end
```

APPENDIX D: DECONVOLUTION RESULTS FOR XRD AND XPS PEAKS[i]

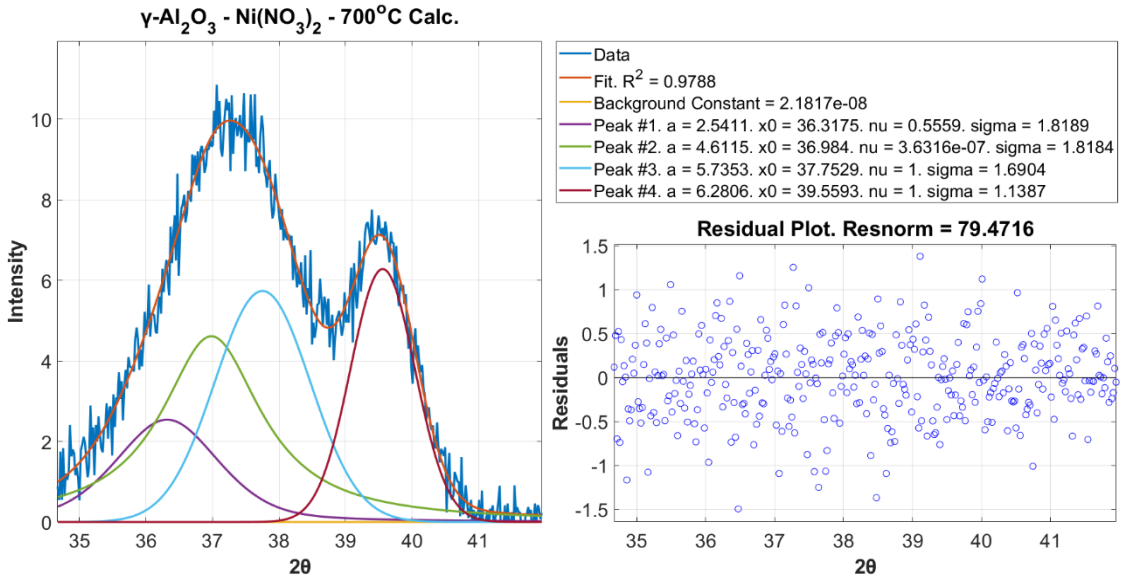

Figure D.1. Deconvolution of overlapping peaks with (311) diffraction peak of $NiAl_2O_4$ in XRD data of reduced γ- Al_2O_3 - $Ni(NO_3)_2$ - 700°C Calc. sample.

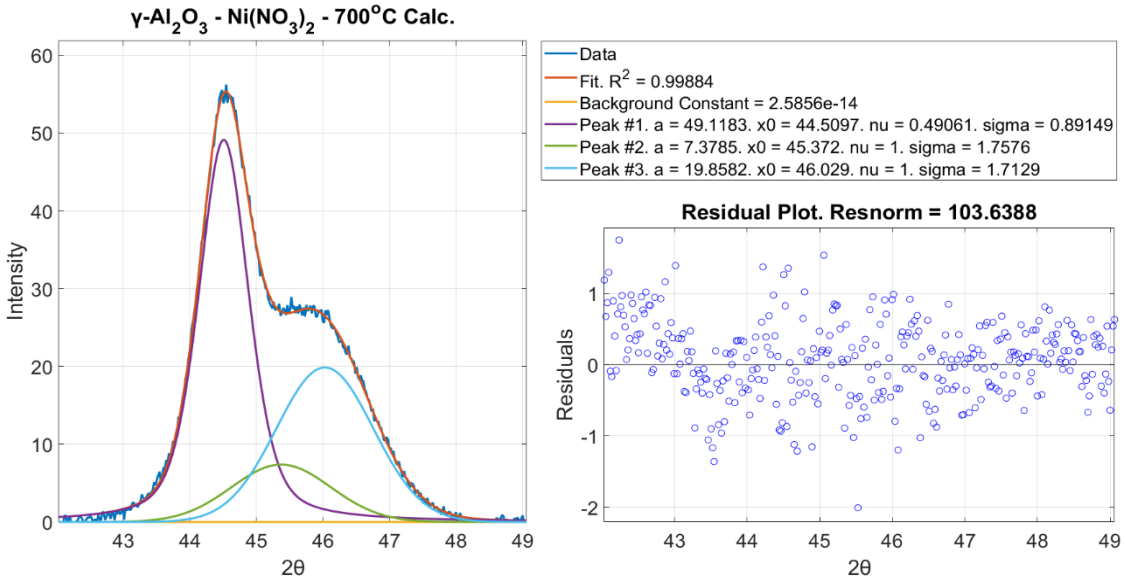

Figure D.2. Deconvolution of overlapping peaks with (111) diffraction peak of Ni in γ-XRD data of reduced Al_2O_3 - $Ni(NO_3)_2$ - 700°C Calc. sample.

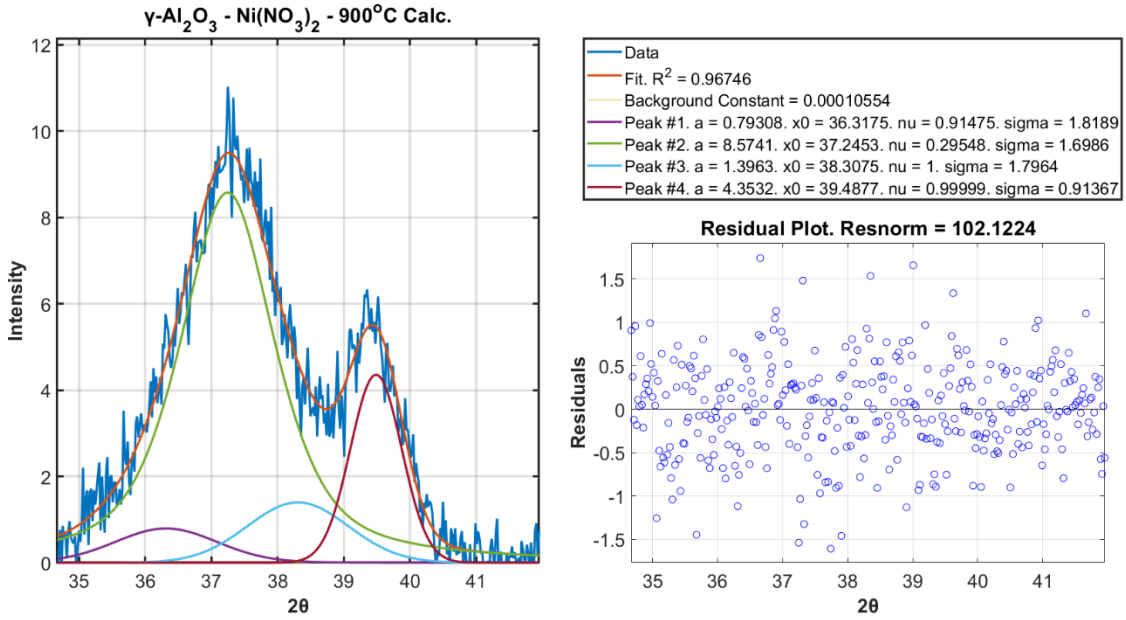

Figure D.3. Deconvolution of overlapping peaks with (311) diffraction peak of $NiAl_2O_4$ in XRD data of reduced γ- Al_2O_3 - $Ni(NO_3)_2$ - 900°C Calc. sample.

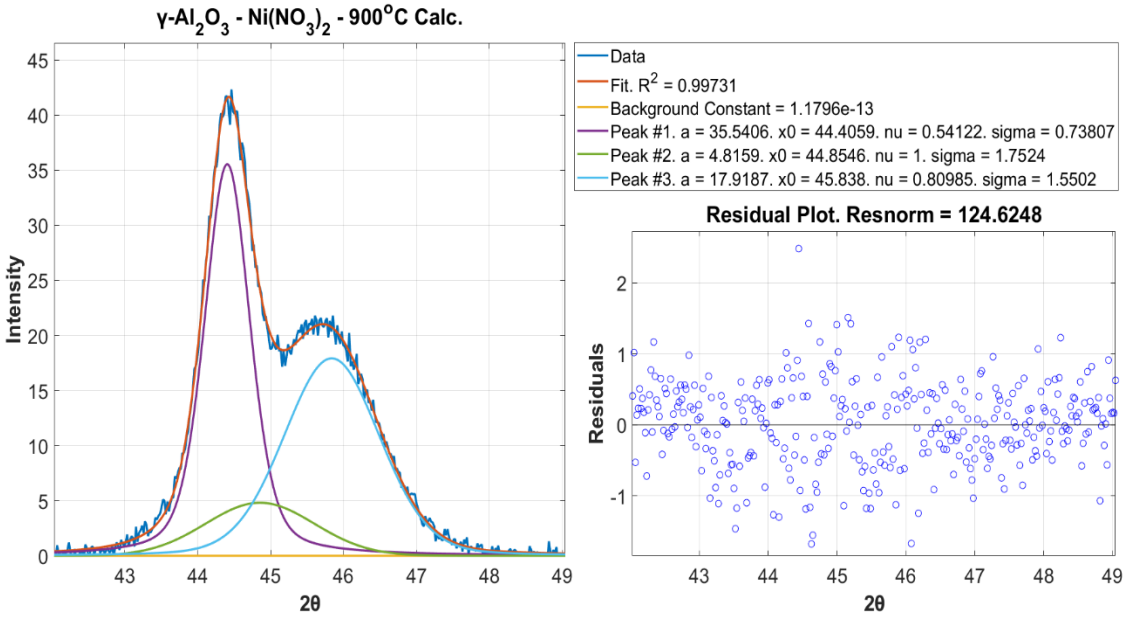

Figure D.4. Deconvolution of overlapping peaks with (111) diffraction peak of Ni in γ-XRD data of reduced Al_2O_3 - $Ni(NO_3)_2$ - 900°C Calc. sample.

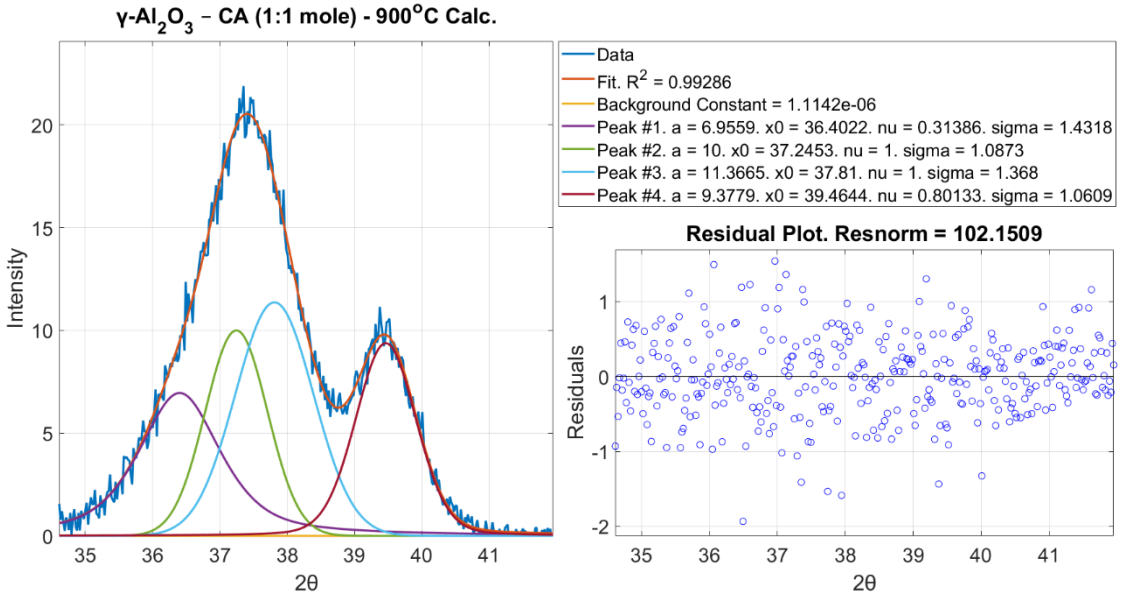

Figure D.5. Deconvolution of overlapping peaks with (311) diffraction peak of $NiAl_2O_4$ in γ- XRD data of reduced Al_2O_3 - CA (1:1 mole) - 900°C Calc. sample.

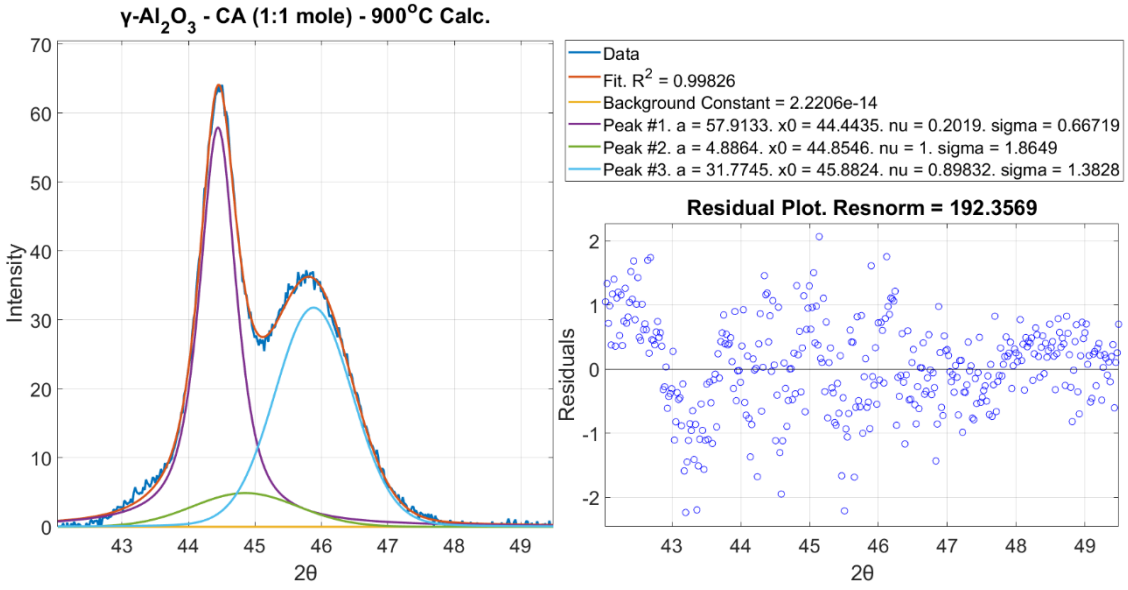

Figure D.6. Deconvolution of overlapping peaks with (111) diffraction peak of Ni in γ-XRD data of reduced Al_2O_3 - CA (1:1 mole) - 900°C Calc.sample.

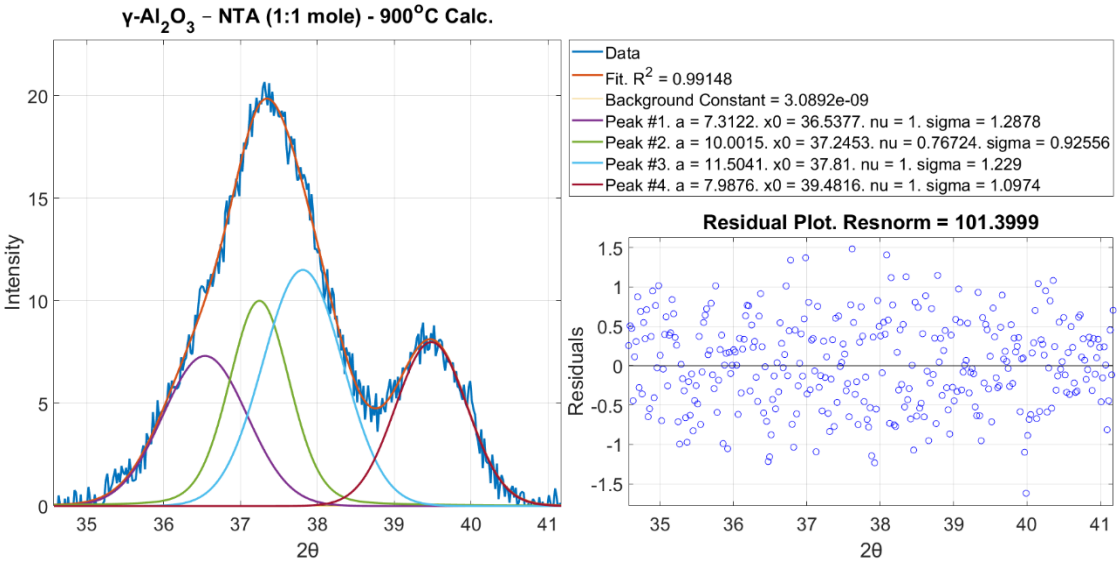

Figure D.7. Deconvolution of overlapping peaks with (311) diffraction peak of $NiAl_2O_4$ in γ- XRD data of reduced Al_2O_3 - NTA (1:1 mole) - 900°C Calc. sample.

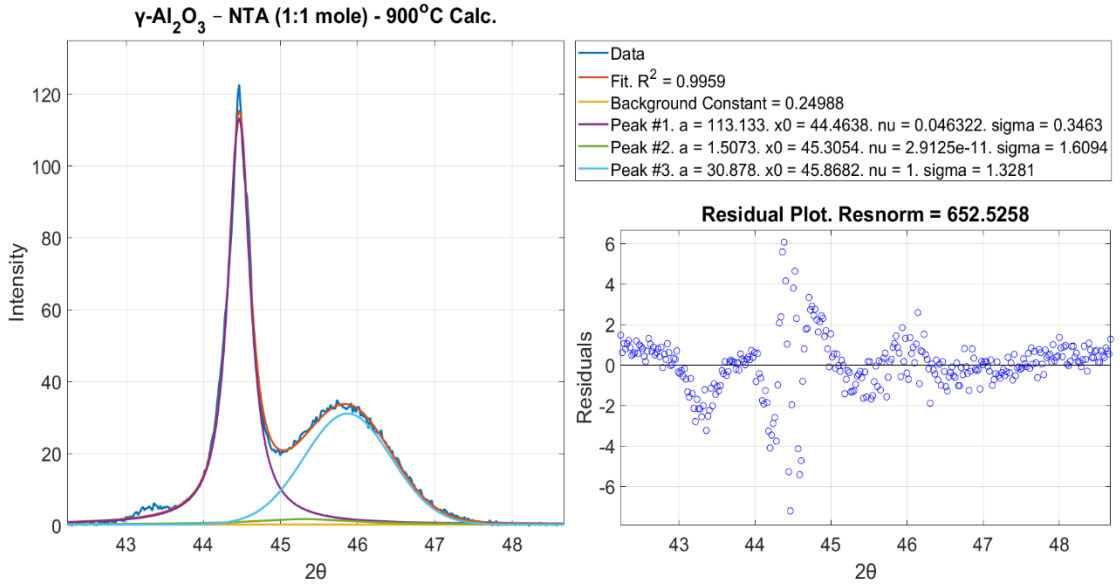

Figure D.8. Deconvolution of overlapping peaks with (111) diffraction peak of Ni in γ-XRD data of reduced Al_2O_3 - NTA (1:1 mole) - 900°C Calc. sample.

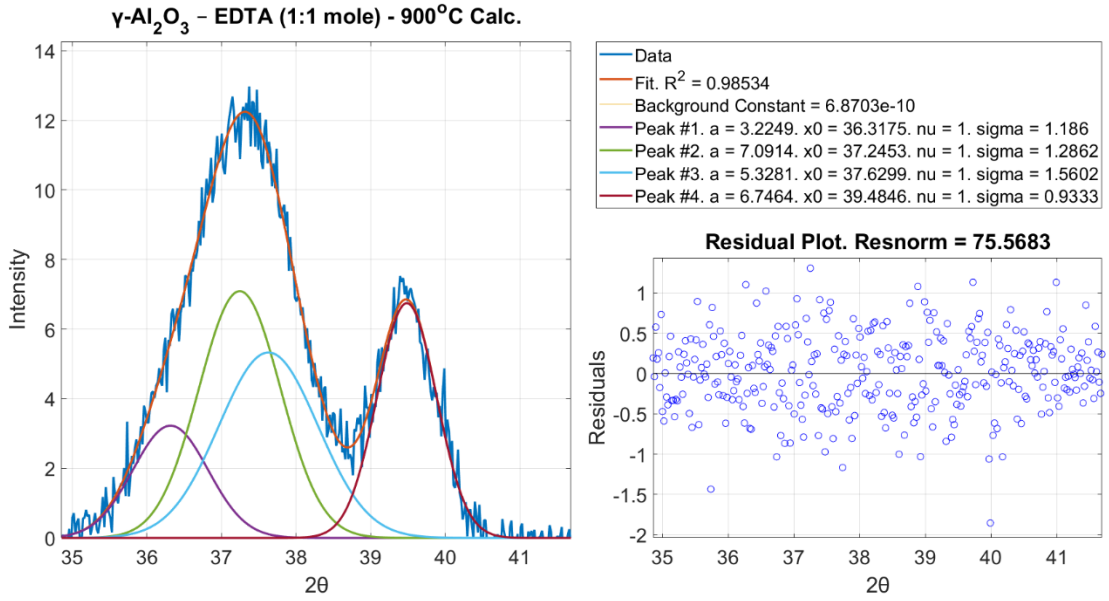

Figure D.9. Deconvolution of overlapping peaks with (311) diffraction peak of $NiAl_2O_4$ in γ- XRD data of reduced Al_2O_3 - EDTA (1:1 mole) - 900°C Calc. sample.

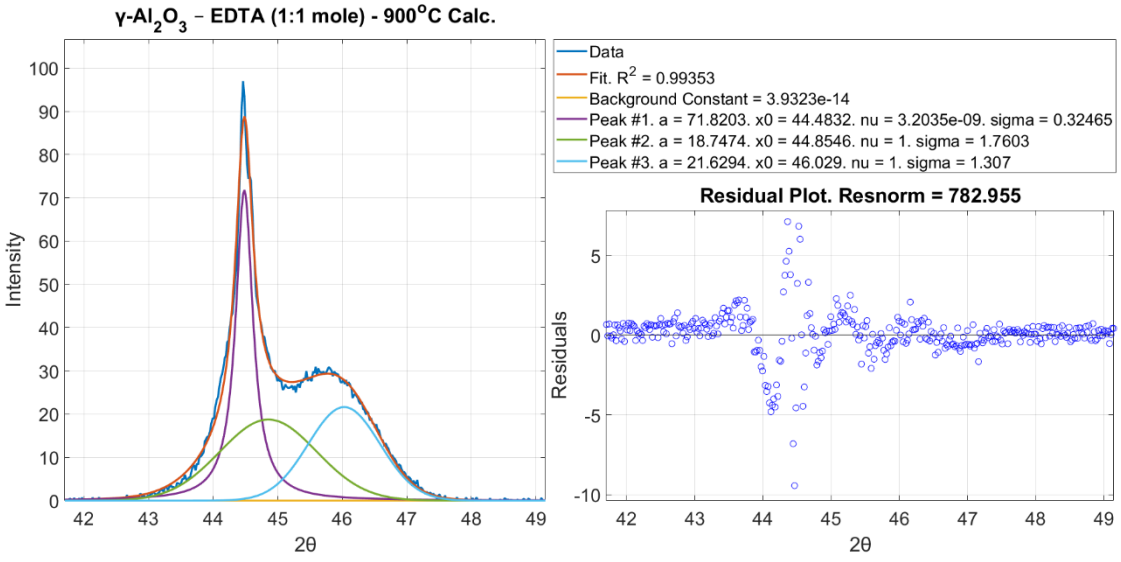

Figure D.10. Deconvolution of overlapping peaks with (111) diffraction peak of Ni in γ-XRD data of reduced Al_2O_3 - EDTA (1:1 mole) - 900°C Calc. sample.

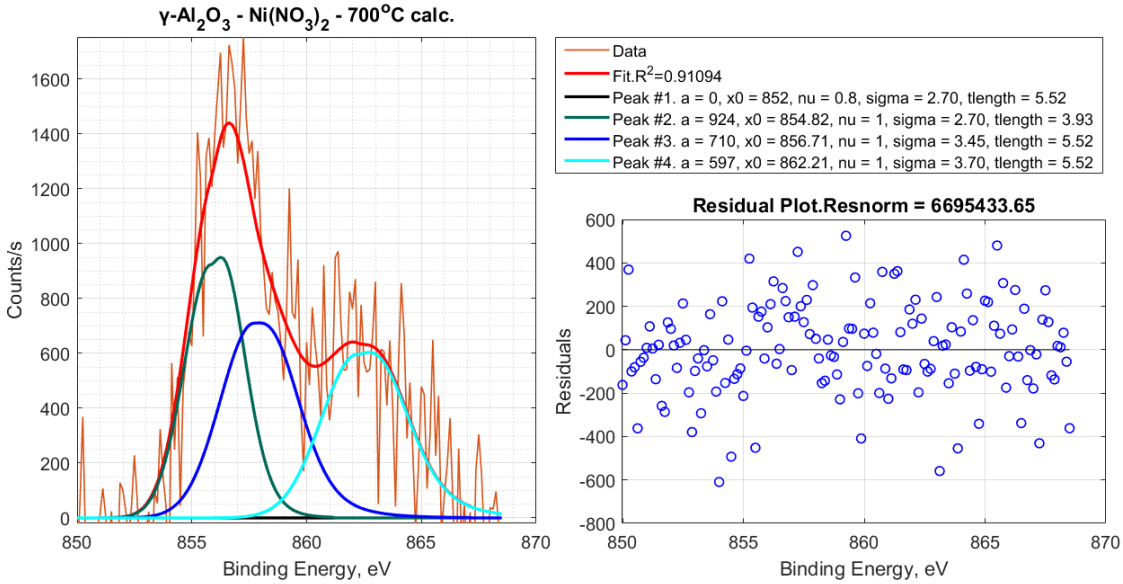

Figure D.11. Deconvolution of XPS results for Ni $2p_{3/2}$ peaks on γ-Al_2O_3 - $Ni(NO_3)_2$ sample calcined at 700°C before reduction.

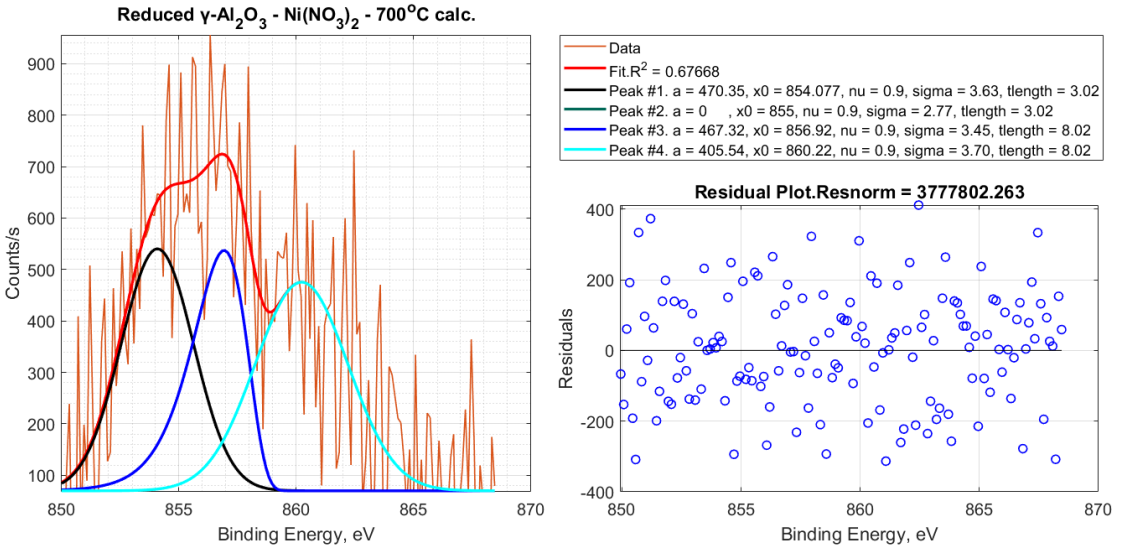

Figure D.12. Deconvolution of XPS results for Ni $2p_{3/2}$ peaks on reduced γ-Al_2O_3 - $Ni(NO_3)_2$ sample calcined at 700°C.

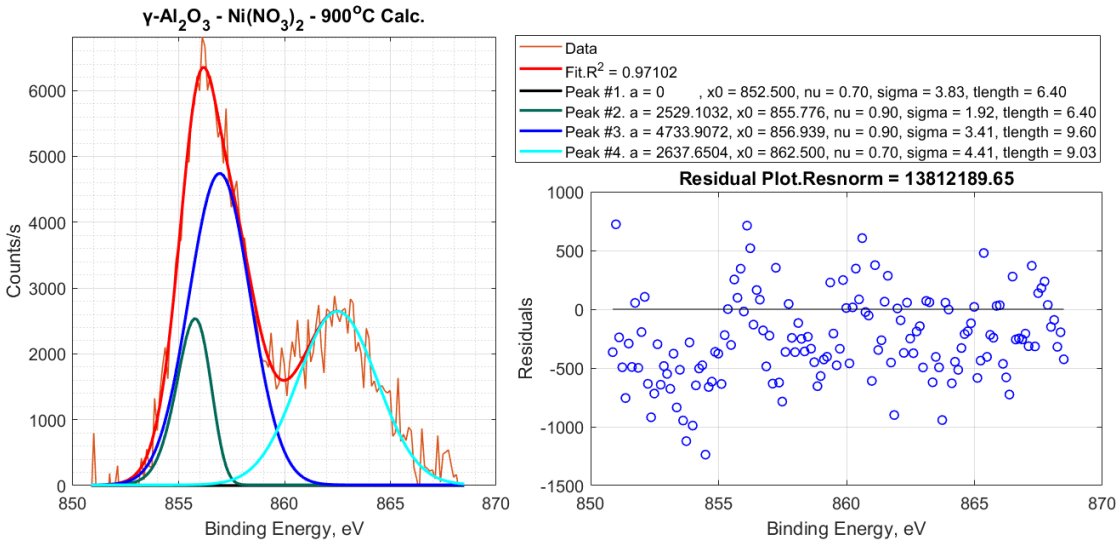

Figure D.13. Deconvolution of XPS results for Ni $2p_{3/2}$ peaks on γ-Al_2O_3 - $Ni(NO_3)_2$ sample calcined at 900°C before reduction.

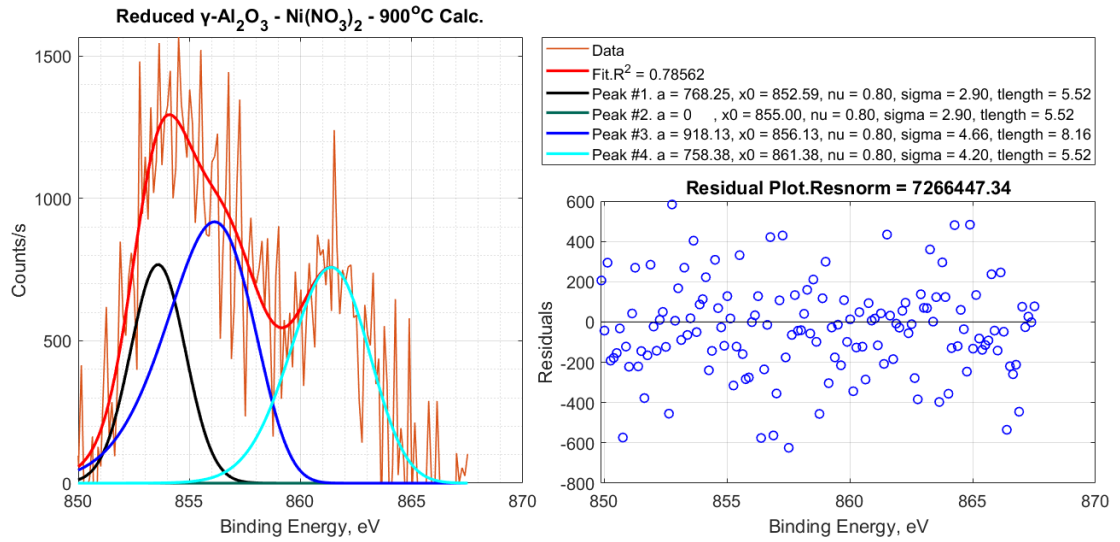

Figure D.14. Deconvolution of XPS results for Ni $2p_{3/2}$ peaks on reduced γ-Al_2O_3 - $Ni(NO_3)_2$ sample calcined at 900°C.

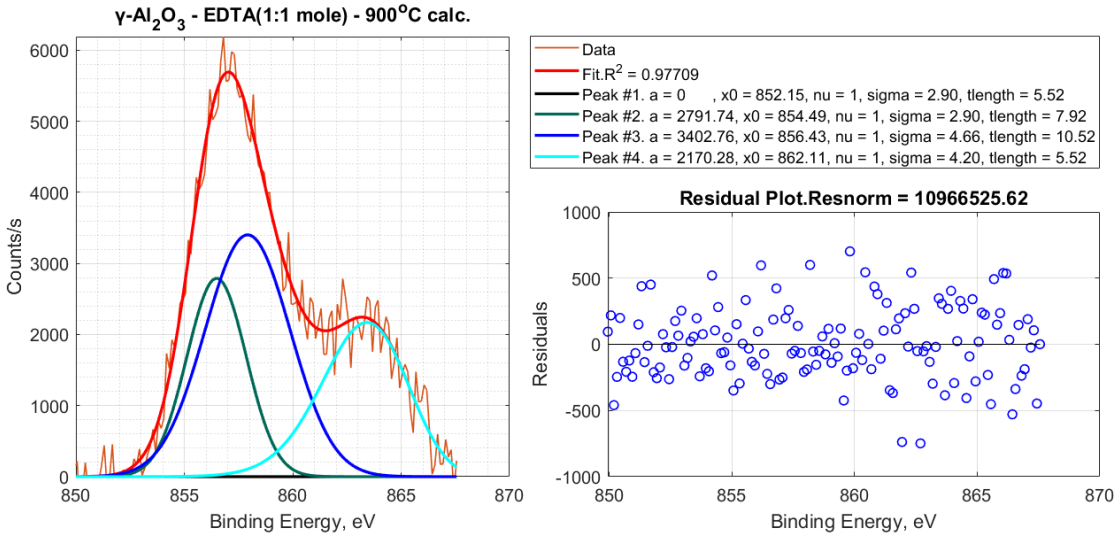

Figure D.15. Deconvolution of XPS results for Ni $2p_{3/2}$ peaks on γ-Al_2O_3 - EDTA (1:1 mole) sample calcined at 900°C before reduction.

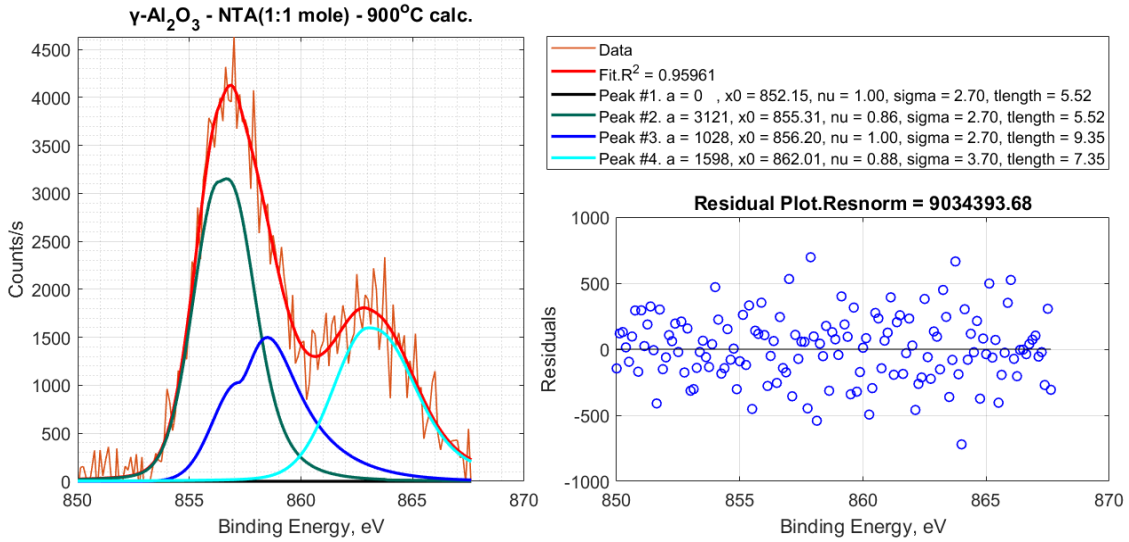

Figure D.16. Deconvolution of XPS results for Ni $2p_{3/2}$ peaks on γ-Al_2O_3 - NTA (1:1 mole) sample calcined at 900°C before reduction.

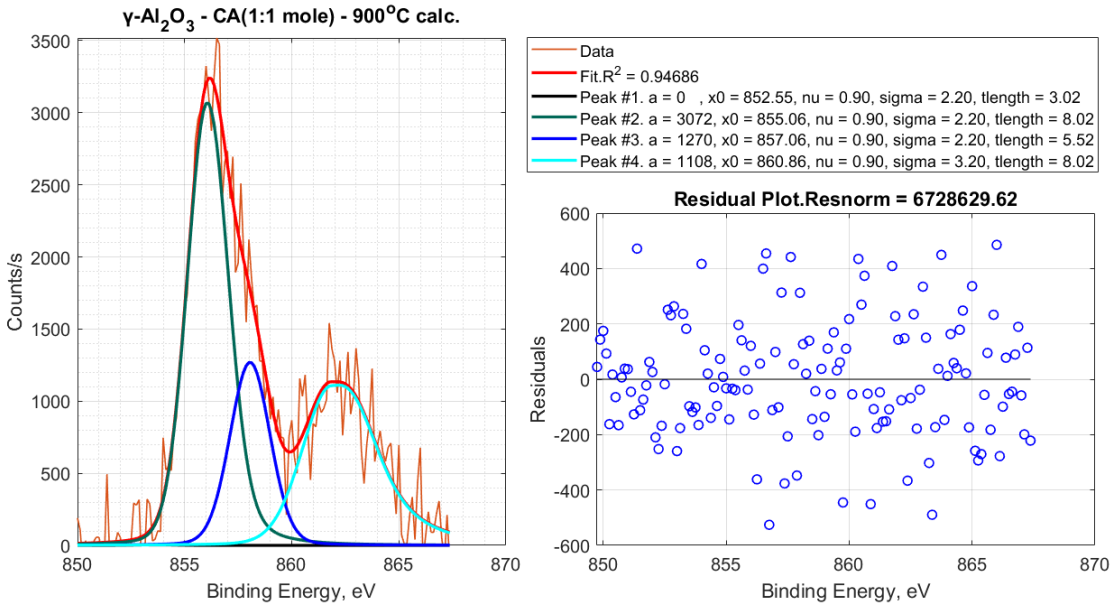

Figure D.17. Deconvolution of XPS results for Ni $2p_{3/2}$ peaks on γ-Al_2O_3 - CA (1:1 mole) sample calcined at 900°C before reduction.

[i] The parameters corresponding to the peaks obtained from deconvolution are provided in the legend as follows: **a** : Maximum intensity of the peak, **nu** : Weighting of peak shape (0=Lorentz < nu < 1=Gauss), **x0** : Peak Center, **sigma** : Full Width of Half Maximum (FWHM), **tlength** : Tail length